Analysis and optimization of a-Si:H/c-Si heterojunction solar cells

Von der Fakultät für Mathematik und Physik
der Gottfried Wilhelm Leibniz Universität Hannover
zur Erlangung des Grades

Doktor der Naturwissenschaften
(Dr. rer. nat.)

genehmigte Dissertation

von

Dipl.-Phys. Ralf Gogolin

geboren am 28.02.1981 in Burgwedel

2015

Referent: Prof. Dr. Jan Schmidt
Korreferent: Prof. Dr. Christoph Tegenkamp
Tag der Promotion: 21. Juli, 2015

Kurzzusammenfassung

Im Rahmen dieser Arbeit werden unterschiedliche Typen von Solarzellen mit Heteroübergängen aus amorphem und kristallinem Silizium (a-Si:H/c-Si) hergestellt und analysiert. Unsere bifacialen siebgedruckten Solarzellen zeigen sehr hohe offene Klemmenspannungen $V_{\mathrm{OC}} = 733\,\mathrm{mV}$, was die exzellente Oberflächenpassivierung direkt am Bauelement demonstriert. Wir zeigen erstmals, dass sich für die Passivierung von $(1\,1\,1)$-orientierten Oberflächen im Gegensatz zu $(1\,0\,0)$-Oberflächen eine erhöhte Wasserstoffverdünnung während der Plasmaabscheidung positiv auswirkt. Diese Erkenntnis ist von besonderer Bedeutung für die Passivierung von texturierten Si-Wafern, dessen $(1\,0\,0)$-Oberfläche zu Pyramiden mit $(1\,1\,1)$-Orientierung wird. Die Solarzelleneffizienz von $20.2\,\%$ ist limitiert durch eine relativ niedrige Kurzschlussstromdichte von $37.1\,\mathrm{mA/cm^2}$ und einen Füllfaktor von $76\,\%$. Wir führen eine detaillierte Analyse der Serienwiderstands-, Abschattungs- und Absorptionsverluste durch. Wir stellen eine neuartige experimentelle Methode vor, die es erstmalig erlaubt, die Serienwiderstandsverluste aufgrund von Ladungsträgertransport über die a-Si:H/ITO (indium tin oxide) Grenzfläche zu quantifizieren. Unsere besten gemessenen Werte sind $0.42\,\Omega\,\mathrm{cm}^2$ für den p-a-Si:H/ITO und $0.1\,\Omega\,\mathrm{cm}^2$ für den n-a-Si:H/ITO Übergang. Um die Absorptionsverluste in den einzelnen a-Si:H- und ITO-Schichten zu bestimmen, führen wir Ray-Tracing-Simulationen durch, wobei die optischen Konstanten der Materialien mittels Ellipsometrie bestimmt werden. Wir erhalten Absorbtionsverluste von $0.02\,\mathrm{mA/cm^2 \cdot nm}$ für die ITO-Schicht, $0.10\,\mathrm{mA/cm^2 \cdot nm}$ für die i-a-Si:H-Schicht sowie $0.11\,\mathrm{mA/cm^2 \cdot nm}$ für die p-a-Si:H-Schicht. Erstmalig quantifizieren wir den Einfluss der verschiedenen Verlustmechanismen auf die Solarzelleneffizienz. Absolute Effizienzverluste von $2 - 2.5\,\%_{\mathrm{abs}}$ stammen von Serienwiderstandsbeiträgen, einschließlich $1.3\,\%_{\mathrm{abs}}$ von der Vorderseitenelektrode und $0.7 - 1.2\,\%_{\mathrm{abs}}$ vom Ladungsträgertransport durch die a-Si:H/ITO-Grenzfläche. Die Effizienzverluste aufgrund von Absorption in den a-Si:H- und ITO-Schichten liegen bei $1.4\,\%_{\mathrm{abs}}$. Die Abschattungsverluste des Metallisierungsgitters betragen $1.3\,\%_{\mathrm{abs}}$. Wir präsentieren außerdem rückseitenkontaktierte a-Si:H/c-Si Solarzellen mit $20.2\,\%$ Wirkungsgrad, was einen Weltrekord für diesen Solarzellentypen zum Zeitpunkt der Veröffentlichung darstellte. Auf dieser Basis untersuchen wir alternative Prozessflüsse und Strukturierungstechniken zur Vereinfachung der Prozesskomplexität. Wir untersuchen erstmals Laserablationstechniken zur Strukturierung von a-Si:H-Schichten. Wir zeigen, dass diese für individuelle Prozesse geeignet sind, jedoch Kompromisse bezüglich Solarzellendesign und -leistung erfordern. Wir identifizieren nasschemische Strukturierungsmethoden mittels Tintendruckertechnologie als geeignet für die schädigungsfreie Strukturierung von a-Si:H-Schichten und führen ein neuartiges Verfahren zur Kontakttrennung mittels siebgedrucktem Silbergitter ein. Mit einem vereinfachten Prozess, bestehend aus lediglich 16 Schritten, stellen wir rückseitenkontaktierte a-Si:H/c-Si Solarzellen mit einer Effizienz von $17.5\,\%$ und einer gemessenen Pseudoeffizienz von $24.0\,\%$ her. Mit Widerstandsnetzwerksimulationen identifizieren wir den a-Si:H/ITO Kontakt als größten Verlustmechanismus.

Schlagworte: Heteroübergang, amorphes Silizium, Solarzellen

Abstract

We fabricate different types of amorphous silicon/crystalline silicon (a-Si:H/c-Si) heterojunction (SHJ) solar cells. Our bifacial screen-printed solar cells feature a very high open-circuit voltage of $V_{\mathrm{OC}} = 733\,\mathrm{mV}$, demonstrating the excellent level of interface passivation directly on device level. We show for the first time that increasing the hydrogen dilution during the plasma-enhanced chemical vapor deposition process is beneficial for the passivation of $(1\,1\,1)$-oriented surfaces, whereas the opposite holds true for $(1\,0\,0)$-oriented substrates, which is of major importance for textured wafer surfaces on the front side of solar cells, where the $(1\,0\,0)$ surface changes to pyramids with $(1\,1\,1)$-oriented facets. The solar cell efficiency of $20.2\,\%$ is limited by the relatively low short-circuit current density of $37.1\,\mathrm{mA/cm^2}$ and a fill factor of $76\,\%$. We perform an in-depth analysis of the series resistance, shading and absorption losses. We introduce a novel experimental approach to measure the resistance losses due to the charge carrier transport across the a-Si:H/c-Si and a-Si:H/ITO (indium tin oxide) interfaces, which are quantified for the first time in this work. We obtain values of $0.42\,\Omega\,\mathrm{cm^2}$ for our p-a-Si:H layers and $0.1\,\Omega\,\mathrm{cm^2}$ for our n-a-Si:H layers. We perform ray tracing simulations to quantify the absorption losses in the different a-Si:H and ITO layers, whereby the optical constants of these layers are determined via ellipsometry. We extract absorption losses of $0.02\,\mathrm{mA/cm^2 \cdot nm}$ for our ITO layer, and $0.10\,\mathrm{mA/cm^2 \cdot nm}$ and $0.11\,\mathrm{mA/cm^2 \cdot nm}$ for the i-a-Si:H and p-a-Si:H layers, respectively. For the first time, the impact of the different loss mechanisms on the SHJ solar cell efficiency are quantified. Absolute efficiency losses of $2 - 2.5\,\%_{\mathrm{abs}}$ stem from series resistance contributions, including $1.3\,\%_{\mathrm{abs}}$ from the front electrode and $0.7 - 1.2\,\%_{\mathrm{abs}}$ from the transport through the a-Si:H layers and a-Si:H/ITO interface. The efficiency losses due to absorption in the a-Si:H and ITO layers are $1.4\,\%_{\mathrm{abs}}$. The shading losses of the actual front metalization grid contributes with $1.3\,\%_{\mathrm{abs}}$ efficiency loss. We also fabricate interdigitated back contacted (IBC) back junction SHJ solar cells with $20.2\,\%$ efficiency, which was a world record for this cell type at the time of publication. On the basis of these solar cells, we investigate alternative process flows and fabrication techniques for the simplification of the process complexity. For the first time, we investigate laser ablation techniques for the structuring of a-Si:H layers in IBC SHJ solar cells, which are found to be potentially applicable for individual processes, but require compromises in terms of device design and performance. We identify wet-chemical structuring using inkjet technology to be well suited for the damage-free structuring of a-Si:H layers and invent a novel contact separation technique via a screen-printed low-temperature Ag grid. With a simplified process containing only 16 steps, we fabricate IBC SHJ solar cells with an efficiency of $17.5\,\%$ and a remarkable measured pseudo efficiency of $24.0\,\%$. With resistive network simulations we identify the a-Si:H/ITO contact resistance to be the main loss mechanism.

Keywords: heterojunction, amorphous silicon, solar cells

Contents

3 Optimization of *a*-Si:H layers for the application in silicon heterojunction solar cells   33

4 Optical properties and ray-tracing simulations   57

5 Analysis of series resistance and shading losses   65

6 Interdigitated back-contacted back-junction silicon heterojunction (IBC-SHJ) solar cells   81

Glossary

Notation	Unit	Definition
∇		Nabla operator
ϵ_2		Imaginary part of pseudodielectric function
η	%	Conversion efficiency
η_{impl}	%	Implied conversion efficiency
μ_{n}	cm^2/Vs	Electron mobility
μ_{p}	cm^2/Vs	Hole mobility
μc-Si		Micro-crystalline silicon
σ	S/cm	Conductivity
ϕ		Wave function
θ	°	Bond angle between two silicon Atoms
ϑ	°C	Temperature
τ_{eff}	s	Effective charge carrier lifetime
a	Å	Distance between two silicon Atoms
Ag		Silver
Al		Aluminum
Ar		Argon
a-Si:H		Hydrogenated amorphous silicon
B_2H_6		Diborane
BSF		Back surface field
c-Si		Crystalline silicon
Cz		Czochralski grown silicon
DOS	cm^{-3}	Density of states
E	eV	Energy
E_{Urbach}	eV	Urbach energy
E_{g}	eV	Band gap
E_{opt}	eV	Optical band gap
E_{f}	eV	Fermi energy
E_{C}	eV	Conduction band edge
E_{V}	eV	Valence band edge
ΔE_{V}	eV	Valence band offset
ΔE_{C}	eV	Conduction band offset
EQE		External quantum efficiency
f	s^{-1}	Frequency
FF	%	Fill factor
FF_0	%	Ideal fill factor
FF_{impl}	%	Implied fill factor
G	$\text{cm}^{-3}\text{s}^{-1}$	Generation rate
GPD	ppm	Gas phase doping
$\hbar$	Js	Planck constant
HF		Hydrofluoric acid
H_2		Hydrogen

Contents

i-*a*-Si:H		Intrinsic amorphous silicon
IBC		Interdigitated back contacted
ISFH		Institute for solar energy research
ITO		indium tin oxide
IWO		indium tungsten oxide
J	$\mathrm{mA}/\mathrm{cm^2}$	Current density
J_0	$\mathrm{fA}/\mathrm{cm^2}$	Saturation current density
J_{SC}	$\mathrm{mA}/\mathrm{cm^2}$	Short circuit current density
J_{rec}	$\mathrm{mA}/\mathrm{cm^2}$	Recombination current density
J_{L}	$\mathrm{mA}/\mathrm{cm^2}$	photogenerated current density
$\vec{k}$		Crystal wave vector
k	eV/K	Boltzmann constant
KOH		Potassium hydroxide
m	kg	Reduced mass
mc		Multi-crystalline silicon
MPP		Maximum power point
n	$\mathrm{cm^{-3}}$	Electron density
n_0	$\mathrm{cm^{-3}}$	Electron density in the dark
n_{i}	$\mathrm{cm^{-3}}$	Intrinsic charge carrier density
Δn	$\mathrm{cm^{-3}}$	Excess electron density
n-*a*-Si:H		Phosphorous doped amorphous silicon
n_{ITO}		refractive index of ITO
n_{air}		refractive index of air
n_{Si}		refractive index of crystalline silicon
N_0	$\mathrm{cm^{-3}}$	States at the mobility edge
$N(E)$	$\mathrm{cm^{-3}}$	Energy dependent density of states distribution
N_{db}	$\mathrm{cm^{-3}}$	Dangling bond density
N_{C}	$\mathrm{cm^{-3}}$	Effective density of states in conduction band
N_{V}	$\mathrm{cm^{-3}}$	Effective density of states in valence band
O_2		Oxygen
p	$\mathrm{cm^{-3}}$	Hole density
p_0	$\mathrm{cm^{-3}}$	Hole density in the dark
P	W	Power
p-*a*-Si:H		Boron doped amorphous silicon
PECVD		Plasma enhanced chemical vapor deposition
PERC		Passivated rear and emitter
PH_3		Phosphine
PVD		Physical vapor deposition
PCD		Photoconductance decay
pFF	%	Pseudo fill factor
PP-TOFMS		Plasma profiling time-of-flight mass spectroscopy
q	As	Elementary electric charge

r	Å	Distance
R		Reflectance
R_s	Ωcm^2	Series resistance
R_{sh}	Ω	Shunt resistance
$R_{a\text{-Si/ITO}}$	Ωcm^2	Resistance through a-Si:H/ITO interface
RISE		Rear interdigitated single evaporation
S	cm/s	Surface recombination velocity
SHJ		Silicon heterojunction
SiH$_4$		Silane
SWE		Staebler Wronski effect
SEM		Scanning electron microscope
SiN		Silicon nitride
SiO		Silicon oxide
SC	%	Silane concentration
t	s	Time
TCO		Transparent conductive oxide
T	K	Absolute temperature
U	cm^{-3}s^{-1}	Recombination rate
U_k		Periodic function
V	mV	Voltage
V_{OC}	mV	Open circuit voltage
V_{impl}	mV	Implied voltage
$V_{\text{OC.impl}}$	mV	Implied open circuit voltage
$V(\vec{r})$	eV	Potential
V_{eff}	eV	Effective potential
W	cm	Thickness
ZnO:Al		Aluminum-doped zinc oxide
ZnO:B		Boron-doped zinc oxide

Introduction

The production of silicon solar cells is well established in the industry [1, 2]. However, an ongoing process is the reduction of the electricity generation costs. That can be achieved by increasing the solar cell efficiency, decreasing the production complexity or saving material. State-of-the-art aluminum back surface field (Al-BSF) solar cells reach conversion efficiencies of 19.9 % in R&D [3] and 19 % in production lines [4] and have a relatively simple process flow. The passivated rear and emitter (PERC) solar cell concept reaches efficiencies of 21.4 % in R&D [5] and $\approx 20\,\%$ in production lines [6] but requires additional processing steps. However, these solar cells are far away from the theoretically reachable efficiency limit of 29 % for silicon solar cells [7], due to (1) a high charge carrier recombination under the metal contacts, (2) high Auger recombination in the emitter and BSF, and (3) low carrier lifetimes of the p-type Czochralski (Cz) or multi-crystalline (mc) silicon bulk materials. Typical recombination current densities (J_0) for the Al-BSF and PERC solar cell concepts are presented in Fig. 0.1 [8, 9]. Due to the high J_0 values, especially of the aluminum back surface field, the conversion efficiency is strongly limited.

The amorphous silicon/crystalline silicon (a-Si:H/c-Si) heterojunction (SHJ) solar cell concept avoids the disadvantages of the conventional homojunction solar cells. In this concept, the entire surface area of the front and rear side is passivated by a thin intrinsic hydrogenated amorphous silicon (i-a-Si:H) layer, which leads to an excellent surface passivation and extremely low recombination current densities. The emitter and back surface field (BSF) are formed by boron-doped p-a-Si:H and phosphorus-doped n-a-Si:H layers. On top of the a-Si:H layers, a transparent conductive oxide (TCO) layer is deposited, which acts as antireflection coating, provides lateral conductivity for the charge carriers to the fingers of the metalization grid, and separates the metal grid from the a-Si:H layers to prevent chemical reactions. Very high open-circuit voltages (V_{OC}) are feasible, because of the excellent surface passivation quality of the a-Si:H layers, and due to the fact

1

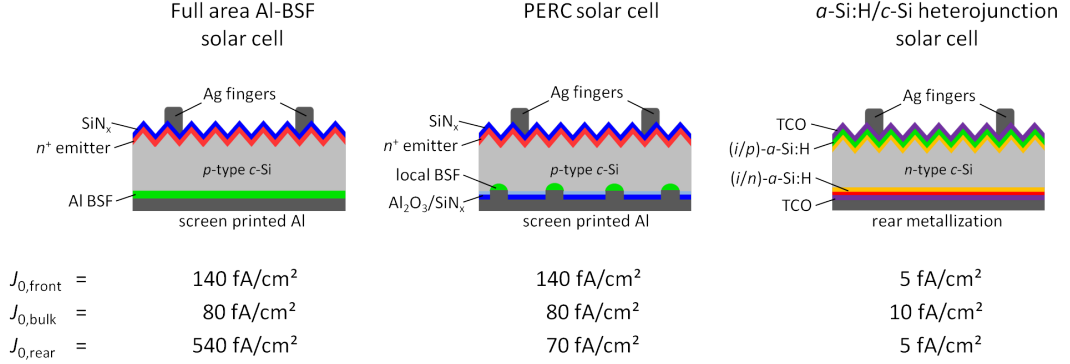|	Full area Al-BSF solar cell	PERC solar cell	a-Si:H/c-Si heterojunction solar cell
$J_{0,\text{front}}$ =	140 fA/cm²	140 fA/cm²	5 fA/cm²
$J_{0,\text{bulk}}$ =	80 fA/cm²	80 fA/cm²	10 fA/cm²
$J_{0,\text{rear}}$ =	540 fA/cm²	70 fA/cm²	5 fA/cm²

Figure 0.1: Schematic representation of a full area Al-BSF solar cell, a PERC-type solar cell, and an a-Si:H/c-Si heterojunction solar cell. Below the graphics the recombination current density (J_0) contributions are listed. The a-Si:H/c-Si heterojunction solar cell provides the lowest J_0 values due to excellent surface passivation properties of the amorphous layers and the use of n-type c-Si material.

that the a-Si:H layers decouple the metal of the front grid from the c-Si wafer. Hence, the major recombination path via a c-Si/metal interface is not present in SHJ solar cells. Because of the symmetrical arrangement of this concept, n-type as well as p-type silicon wafers can be used. However, n-type c-Si is preferred, because of its typically higher and more stable carrier lifetime which is necessary to exploit the full V_{OC} potential provided by the excellent surface passivation properties of the a-Si:H layers. The production complexity of SHJ solar cells is relatively low. A further advantage of the SHJ solar cell concept is the low process temperatures ($<200\,°\text{C}$) that allow for the use of very thin wafer material, because of reduced breakage during the manufacturing process.

A further development is the interdigitated back contacted (IBC) back junction SHJ solar cell concept, where both contacts for electrons and holes are located on the rear side of the solar cell [10, 11, 12]. This concept avoids the light absorption in the a-Si:H and TCO layers on the front side and the shading of the front metallization grid. However, this cell structure increases the process complexity immensely due to structuring of the amorphous layers on the rear side.

SHJ solar cells were first investigated by Sanyo, demonstrating an efficiency of 18% in 1992 [13]. Despite many international research activities in this area [14, 15], Panasonic (former Sanyo) is currently the only major producer of this attractive cell type. Their SHJ solar cells in production reach efficiencies of 21.6% with module efficiencies of 19% [16]. The current record for both side contacted laboratory cells is held by Panasonic with an efficiency of 24.7 % ($V_{\text{OC}} = 750\,\text{mV}$, $J_{\text{SC}} = 39.5\,\text{mA/cm}^2$, $FF = 83.2\,\%$) [17, 18], and 25.6 % ($V_{\text{OC}} = 740\,\text{mV}$, $J_{\text{SC}} = 41.8\,\text{mA/cm}^2$, $FF = 82.7\,\%$) for IBC SHJ solar cells.

However, a large gap between the world record SHJ solar cell performance and the solar cells from mass production is present. One of the main challenges is the

carrier transport across the a-Si:H/c-Si heterojunction, which reduces the fill factor of SHJ solar cells. Additionally, in both-side contacted SHJ solar cells, optical losses reduce the short-current density due to absorption in the a-Si:H and TCO layers. For the fabrication of IBC SHJ solar cells suitable structuring techniques for the a-Si:H and TCO layers on the rear side have to be identified. These topics are investigated in this thesis, which is organized as follows:

Chapter 1 presents the SHJ concept and discusses its advantages and challenges in detail. An overview of the main properties of a-Si:H is given, including structural and electronic properties, as well as growth and doping mechanisms. Finally, we briefly address the topic of TCO deposition.

Chapter 2 presents the current-voltage characteristics of the solar cell. It also introduces the main characterization techniques used in this thesis. Current-voltage measurements are used to determine the characteristics of finished solar cells. Photo-conductance decay measurements are used to determine the charge carrier lifetime on test samples.

Chapter 3 covers optimization processes of our a-Si:H layers and introduces the PECVD cluster tool used for the deposition of the a-Si:H layers. Lifetime optimization processes of our i-a-Si:H layers are performed in dependence of the deposition parameters and post treatments. Furthermore, the doping efficiency of n-a-Si:H and p-a-Si:H and its influence on the solar cell performance is studied. Additionally, the structural composition of the a-Si:H layers is investigated.

Chapter 4 covers ellipsometric measurements to determine the optical constants of our a-Si:H and TCO layers. Ray-tracing simulations are performed to identify and quantify the optical losses in the different layers. The simulation results are compared with experimental data.

Chapter 5 introduces a novel method to quantify the series resistance through the a-Si:H layer and a-Si:H/TCO interface. Additionally, results for our bifacial screen-printed SHJ solar cells are presented. On the basis of these solar cells, an in-depth analysis of the series resistance, shading and absorption losses is performed.

Chapter 6 covers the fabrication and characterization of IBC SHJ solar cells. We investigate alternative process flows and fabrication techniques, i.e. laser ablation and inkjet structuring, for the simplification of the process complexity. We present IBC SHJ solar cells fabricated with a simplified process flow and perform a detailed analysis of the series resistance losses by means of resistive network simulations.

The *a*-Si:H/*c*-Si heterojunction solar cell concept

In this Chapter, the characteristic features of the SHJ solar cell concept are presented. First, the working principles of SHJ solar cells are reviewed. Second, an overview of the *a*-Si:H and TCO properties is given.

1.1 Characteristic features of *a*-Si:H/*c*-Si heterojunction solar cells

An ideal solar cell consists of a light absorbing material and two charge carrier selective contacts for electrons and holes, respectively. An energy band diagram of such an ideal structure is shown in Fig. 1.1. On the left side of the structure there is a potential barrier for electrons, whereas the holes can easily enter. On the right side the electrons can pass while holes are blocked. Depending on the height of the barrier, the blocking of one charge carrier species is more or less efficient. In the ideal case, no interface recombination takes place.
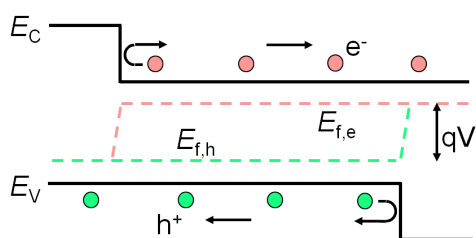

Figure 1.1: Schematic representation of the band diagram for ideal selective contacts. On one side the conduction band inhibits a barrier for electrons, and on the other side the valance band inhibits a barrier for holes.
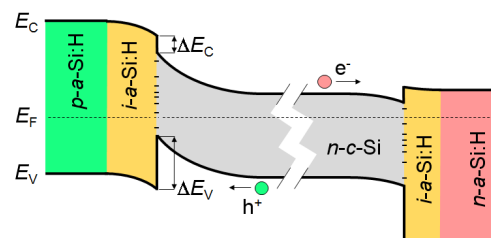

Figure 1.2: Schematic representation of the band diagram for a SHJ solar cell. Due to the different work functions of the two materials, band offsets are built on both sides for electrons and holes.

In the SHJ solar cell, the absorber material is the *c*-Si wafer and the carrier selective contacts are provided by phosphorus- or boron-doped *a*-Si:H layers. Whereas the *c*-Si band gap is $\approx 1.1\,\text{eV}$, the *a*-Si:H layers have a band gap of $\approx 1.7\,\text{eV}$. Bringing these two materials in contact, the energy bands arrange as indicated in Fig. 1.2. The band offset in the valence band is $\approx 2 - 3$ times larger than in the conduction band. Typical values for the band offsets in the valence and conduction bands are $\Delta E_{\text{V}} \approx 400 - 450\,\text{meV}$ and $\Delta E_{\text{C}} \approx 150 - 200\,\text{meV}$, respectively [19]. When bringing doped *a*-Si:H layers in contact with the *c*-Si wafer, the energy bands arrange in a way that mostly all band bending occurs in the *c*-Si substrate, because the *a*-Si layers inhibit a large density of rechargeable states, that compensate the charge density in the *c*-Si bulk [20].

In addition to the carrier selectivity of the doped amorphous layers, intrinsic *i*-*a*-Si:H layers provide an excellent surface passivation. At the *c*-Si surface, many defect states are present in the band gap due to the discontinuity of the silicon crystal. However, the *i*-*a*-Si:H layer consists of a high amount of hydrogen, which can efficiently saturate these states by bonding to the unsaturated silicon bonds.

A unique feature of the SHJ solar cell concept is the separation of the *c*-Si surface from the metalization grid by the *a*-Si:H layers. Therefore, in contrast to conventional solar cells, the entire *c*-Si surface is almost perfectly passivated and no trade-off between metalized and passivated areas is necessary. However, the carrier transport across the *a*-Si:H/*c*-Si and the *a*-Si:H/TCO interfaces is not free of losses. Various transport mechanisms and formalisms have been discussed in the past, mainly based on theoretical considerations [21]. In this work, a novel experimental approach for the determination of the carrier transport across the *a*-Si:H/*c*-Si and *a*-Si:H/TCO interfaces is introduced in Chapter 5.

Because of the high defect density of the *a*-Si:H layers, nearly all generated charge carriers recombine again before they can be separated. Therefore, in terms of charge carrier collection, the *a*-Si:H layers can be assumed as electrically dead [22]. That leads to a drastically reduced spectral response at small wavelengths. Additionally, sub-band gap absorption can lead to a decrease of the spectral response over the entire solar spectrum. For this reason, the *a*-Si:H layers on the front side of a SHJ solar cell are deposited as thin as possible, without compromising the passivation quality. Another possibility is to enlarge the band gap by alloying the *a*-Si:H layers with oxygen or carbon [23, 24].

The *a*-Si:H layers do not provide any lateral conductivity, even if they are heavily doped. Therefore, a transparent conductive oxide (TCO) layer is deposited onto the *a*-Si:H layers to transport the charge carriers to the fingers of the metalization grid. However, these TCO layers also absorb light and can influence the passivation quality of the *a*-Si:H layers [25, 26]. The metalization can be conducted e.g. by screen-printing of low-temperature Ag paste, physical vapor deposition (PVD) or plating.

The advantages of a-Si:H/c-Si heterojunction solar cells can be summarized as follows:

1. Very high open-circuit voltage (V_{OC}) potential due to the excellent level of surface passivation of c-Si by i-a-Si:H.

2. Electrical separation of the metal contacts from the c-Si surface. The entire wafer surface is passivated with i-a-Si:H, leading to extremely low surface recombination velocities.

3. Low process complexity. The process steps are (1) wafer cleaning, (2) a-Si:H depositions, (3) TCO depositions, (4) metalization and drying.

4. Low-temperature processing ($<200\,°C$) and hence reduced thermal stress and a decreased breakage rate during the solar cell manufacturing process as well as a reduced energy consumption during processing.

However, there still exist some major challenges for SHJ solar cells:

1. Complex device physics. The transport across the heterojunctions influences the fill factor *FF* of the solar cell.

2. High parasitic absorption in the a-Si:H and TCO layers leads to a decreased short-circuit current density (J_{SC}).

3. The low-temperature processing requires the use of non-standard screen-printing pastes. Suitable metalization techniques still have to be identified.

1.2 Amorphous silicon

Hydrogenated amorphous silicon (a-Si:H) is the crucial component of silicon heterojunction (SHJ) solar cells. Intrinsic i-a-Si:H layers provide excellent surface passivation of the crystalline silicon (c-Si) substrate, whereas boron-doped p-a-Si:H layers and phosphorus-doped n-a-Si:H layers form the emitter or the back surface field (BSF) of the solar cell. In this Chapter, an overview of the main properties of amorphous silicon is given. That includes the structural and electronic properties as well as the growth and doping mechanisms. The interested reader is referred to [27, 28] for further information.

1.2.1 Structural properties of amorphous silicon

Silicon atoms are fourfold coordinated and usually bonded to four adjacent atoms in a tetrahedral configuration. In a silicon crystal, this periodic configuration extends over a long range. In this way, the structure of a silicon crystal is well defined through its lattice with fixed distances and angles between the silicon atoms over long distances. In amorphous silicon (a-Si), such a long-range order does not
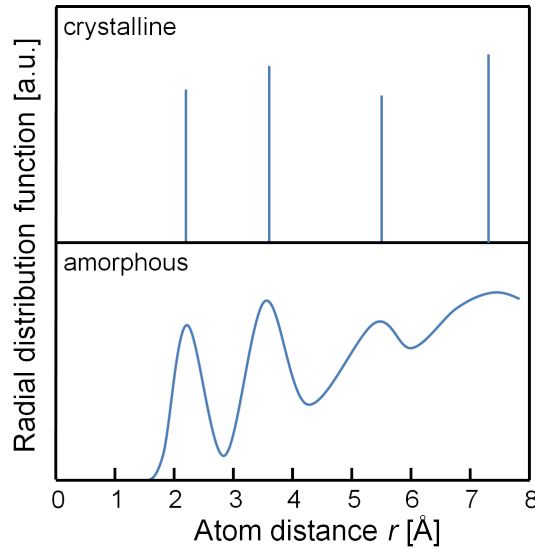
Figure 1.3: Schematic representation of the radial distribution function for a crystalline and an amorphous material according to [27].

exist. Instead the structurally disordered *a*-Si forms a continuous random network with varying bond angles and lengths [29, 30]. However, *a*-Si is not completely disordered at short distances. The covalent bonds as well as the bond length and bond angles to the nearest neighbor atoms are nearly identical to *c*-Si. The disorder of *a*-Si can be illustrated by the radial distribution function, which gives the probability of an atom to be found at a certain distance r to another atom. Fig. 1.3 shows a schematic representation of the radial distribution function for a crystalline and an amorphous material. The crystalline material shows discrete peaks at distinct distances, whereas the amorphous material is characterized by broadened peaks for the nearest neighbor atoms (short-range order) and a nearly homogeneous distribution for larger distances (long-range disorder).

The radial distribution function of *a*-Si can be measured using *x*-ray or neutron scattering experiments [31]. It was found that the distance $a = 2.35\,\text{Å}$ and intensity of the first *a*-Si peak is in accordance with the first *c*-Si peak, which confirms the fourfold coordination of the Si atoms. The width of the first *a*-Si peak originates from bond length variations of $\pm 1\,\%$. The second peak arises from the second nearest atoms with a distance of $2a \cdot sin(\theta/2) = 3.5\,\text{Å}$, where θ is the bond angle. The distance and the resulting average bond angle of 109° are again close to that of *c*-Si. This confirms the tetrahedral bonding of *a*-Si. However, the *a*-Si peak is broadened out because of a distortion of the bond lengths and the bond angles of approximately $\pm 10°$[32]. The third peak for *a*-Si is already widely broadened due to an almost random distribution of distances and angles. The most stable continuous random network is achieved for a coordination number of 2.45 [33].

Consequently, the *a*-Si network with its mostly fourfold coordinated Si atoms is over-coordinated and strained and tends to crystallize easily.

1.2.2 Electronic properties of amorphous silicon

The band structure and the sharp band edges in crystalline silicon result from the periodic lattice of the crystal. The solutions of the Schroedinger equation with a periodic potential are the Bloch wave functions which are extended in space.

$$-\frac{\hbar^2}{2m}\nabla^2\phi + V(\vec{r})\phi = E\phi \quad \text{with} \quad \phi(\vec{r}) = exp(i\vec{k}\vec{r}) \cdot U_k(\vec{r})\,. \tag{1.1}$$

In contrast to a silicon crystal, the amorphous silicon random network is structurally disordered. Due to the absence of a long-range order, no periodic potential, and hence no Bloch wave functions which are extended in space exist. The phase coherence is lost over a distance of only a few atom spacings and the electrons scatter from one Bloch state into another [34]. Consequences are:

1. Replacement of the E-$\vec{k}$ dispersion relations to describe the energy bands by an energy-dependent density of states (DOS) distribution $N(E)$.

2. Scattering of charge carriers hampers the carrier transport in *a*-Si. Compared to *c*-Si, much lower electron and hole mobilities are found. Typical values for the charge carrier mobilities in *a*-Si are in the range of 1-$5\,\mathrm{cm^2/Vs}$.

3. The $\vec{k}$-conservation rules do not apply for optical transitions in *a*-Si, i.e. the distinction between direct and indirect band gap is lost. Transitions occur between states that overlap in real space. Therefore, *a*-Si behaves like a direct semiconductor.

The electronic density of states in amorphous silicon

The bond energy in *a*-Si is approximately $2.5\,\mathrm{eV}$. Instead, the disorder energy that arises from bond angle variations is approximately $0.1\,\mathrm{eV}$. Thus, compared to the bond energy the disorder energy is relatively small. Therefore, it is a reasonable assumption that the overall shape of valence and conduction bands are nearly identical. Fig. 1.4 shows a schematic representation of the bond and disorder energy in *a*-Si.

However, due to its high structural disorder, amorphous silicon contains a large number of defects in the "forbidden" band gap. Fig. 1.5 shows a schematic representation of the density of states of *a*-Si:H. The deviation of bond angles and lengths lead to localized states merging into the "forbidden" band gap [35]. The mobility of the charge carriers in these band tail states is drastically decreased and therefore the separation between the localized band tail states and the extended conduction states is called mobility edge [36]. The extension of the tail states into
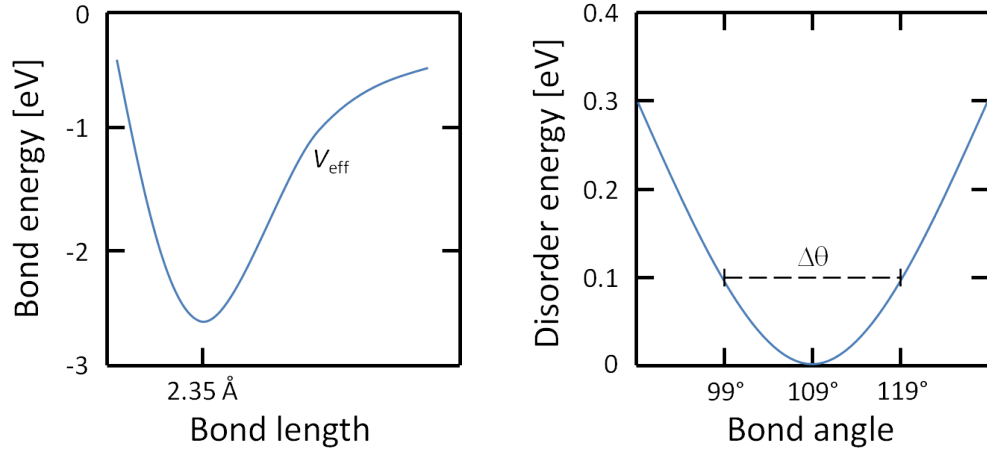
Figure 1.4: The left graph shows a schematic representation of the bond energy as a function of the bond length of silicon atoms in *a*-Si (effective potential V_{eff}). The bond energy is $\approx 2.5\,\text{eV}$. The right graph shows the disorder energy in *a*-Si as a function of the bond angle. The bond angle variations in *a*-Si are typically $\pm 10\,\%$ leading to a disorder energy of $\approx 0.1\,\text{eV}$.
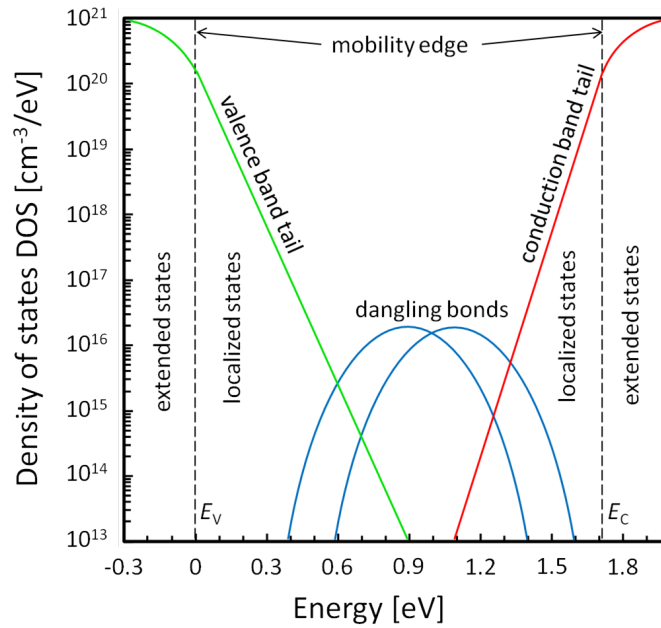

Figure 1.5: Schematic DOS distribution of typical *a*-Si:H. Three regions can be identified: the localized dangling bond defects deep in the mobility gap, the localized valence and conduction band tail states, and the extended states in the conduction and valance band, which are separated from the tail states by the mobility edge.

the mobility gap depends on the amount of disorder in the *a*-Si material. The slope of the band tails is called Urbach energy $E_{\text{Urbach}} = k\,T_{\text{Urbach}}$ and is typically in a range of $60\,\text{meV}$ for the valence band tail and $40\,\text{meV}$ for the conduction band tail [37]. With a fixed density of states at the mobility edges N_0, the density of localized tail states $N(E)$ can be expressed by the equation:

$$N(E) = N_0\,exp\left(\frac{-E}{k\,T_{\text{Urbach}}}\right). \tag{1.2}$$

The defects deep in the mobility gap stem from coordination defects, such as threefold coordinated silicon atoms, called dangling bonds.[1] The dangling bond defects can be negatively, neutral or positively charged. The subtraction or addition of an electron leads to a net-charge, i.e dangling bond defects have either an electric charge or a paramagnetic spin. In summary, three distinct regions can be separated:

1. The main conduction and valence bands which are separated from the tail states by the mobility edges.

2. The localized band tail states that merge into the mobility gap, stemming from the structural disorder in *a*-Si.

3. The deep defect states in the mobility gap, stemming from coordination defects (dangling bonds).

Carrier transport in amorphous silicon

In crystalline silicon the carrier transport takes place in the valance and conduction band. The mobility of the charge carriers is relatively high due to the conduction via extended states. In amorphous silicon, different transport mechanisms exist, requiring a clear distinction between the conductivity via localized and extended states [38]:

1. Conduction in the extended states of the valance and conduction band is the most important transport mechanism for high-quality hydrogenated *a*-Si:H. The conduction takes place near the mobility edges. However, the mobility of *a*-Si:H is drastically reduced compared to *c*-Si due to scattering of the charge carriers as a consequence of the non-periodic potential.

2. A second transport mechanism is hopping conduction in the band tail states [39]. Hopping conduction takes place by alternate trapping of charge carriers in the localized tail states and thermal excitation to the energetically higher

---

[1]The definition of a defect is different in *c*-Si compared to *a*-Si. In *c*-Si any deviation from the perfect crystalline lattice is a defect, among them vacancies, interstitials, dislocations, stacking faults or impurities. However, this is not a good explanation for defects in *a*-Si, since disorder is an inherent property. Therefore, coordination defects are introduced to describe atoms that are not incorporated with their favorable coordination number

conduction states. The so-called drift mobility is therefore even lower than the mobility in the conduction and valence bands. Additionally, the drift mobility is highly temperature dependent because of the energy needed to excite a trapped charge carrier from a localized tail state into a conducting state.

3. A third transport mechanism is hopping at Fermi level in the localized states deep in the mobility gap [40]. However, this conduction path is only relevant in non-hydrogenated *a*-Si, because of its higher dangling bond defect density.

Optical transitions in amorphous silicon

In crystalline silicon, optical transitions are constrained to energy-momentum conservation. Direct transitions can only occur with the same momentum $\vec{k}$ and indirect transitions can only occur with the presence of phonons. However, $\vec{k}$ is a consequence of the lattice periodicity, which does not exist in *a*-Si. Therefore the $\vec{k}$-conservation rules do not apply in *a*-Si and only energy conservation has to be fulfilled for optical transitions. The distinction between direct and indirect behavior is lost. Transitions occur between states that overlap in real space. Consequently, *a*-Si behaves like a direct semiconductor.

Although the mobility gap $E_\mathrm{g} = 1.7\,\mathrm{eV}$ of *a*-Si is wider compared to the band gap $E_\mathrm{g} = 1.1\,\mathrm{eV}$ of *c*-Si, the absorption in *a*-Si is much higher due to absorption in the localized tail states. The absorption coefficient for visible light of *a*-Si is about one magnitude higher than for *c*-Si [41]. In SHJ solar cells nearly all charge carriers that are generated in the doped *a*-Si layers recombine very quickly due to the high defect densities, and only $30\,\%$ of the charge carriers from the intrinsic layers can be extracted [22]. This parasitic absorption can drastically reduce the photocurrent of SHJ solar cells. The exact optical properties of *a*-Si:H depend largely on the hydrogen content [42, 43] and bonding [44] in the film as well as on the disorder of the *a*-Si:H network [45].

1.2.3 Hydrogen in amorphous silicon

For preparing device-relevant hydrogenated amorphous silicon (*a*-Si:H) with a sufficiently low defect density, the incorporation of hydrogen is indispensable. Hydrogen can reduce the strain of the over-coordinated amorphous silicon network and saturate dangling bond defects.

The bonding structure of hydrogen atoms in *a*-Si:H is fundamentally different from the bonding structure of the silicon atoms. The silicon atoms form a stiff over-coordinated network that is far away from equilibrium and contains high strain energy. The diffusion of silicon atoms is negligible. In contrast to that, the hydrogen atoms are only weakly bonded and can easily diffuse through the network as interstitials [46]. The hydrogen distribution is a mobile equilibrium structure. The hydrogen content in *a*-Si:H films depends on the deposition parameters and

affects the electronic properties. During the deposition or thermal post treatment silicon dangling bonds can be saturated by hydrogen, which eventually leads to a reduction of the defect density from $10^{20}\,\mathrm{cm}^{-3}$ to 10^{15} - $10^{16}\,\mathrm{cm}^{-3}$, which corresponds to only 1 - 10 dangling bonds per 10^7 silicon atoms [47].

Hydrogen can be incorporated in different configurations, i.e. distributed or clustered. Only the distributed hydrogen atoms contribute to the passivation of dangling bonds. In contrast to that, clustered hydrogen can even increase the defect density. With an increase of the total hydrogen in the film, the amount of clustered hydrogen increases too, whereas the distributed hydrogen content remains relatively constant at a maximum level of $\approx 10\,\%$ [48]. In high quality *a*-Si:H about $10 - 15\,\%$ hydrogen is incorporated. That is much less than the theoretically needed amount above $50\,\%$ to bring the fourfold coordinated amorphous network to its ideal coordination number of 2.45. Hence, the network of high-quality *a*-Si:H still contains some strain. However, during the deposition, highly strained Si - Si bonds, which lie below the chemical potential of the hydrogen atoms, can be cracked [49], and more stable Si - Si bonds or Si - H bonds can be reconstructed. In this way, weak Si - Si bonds are broken while stronger bonds remain. These reactions can only occur during the deposition if enough hydrogen and a sufficient energy is present at the growing surface of the *a*-Si:H film. For this reason high-quality *a*-Si:H is deposited at elevated temperatures or requires a thermal post treatment after the deposition [50].

At temperatures of $200 - 400\,^\circ\mathrm{C}$ the hydrogen totally vanishes of the *a*-Si:H films. The diffusion coefficient of hydrogen strongly depends on the doping of the *a*-Si:H film [51]. The optimum deposition temperature therefore is doping-dependent and lies typically around $100 - 200\,^\circ\mathrm{C}$.[2] For lower temperatures the hydrogen diffusion coefficient is too small to allow structural equilibrium. In contrast, if the temperature is too high, the hydrogen does not remain within the *a*-Si:H film.

1.2.4 Growth of amorphous silicon

The most common precursor to grow amorphous silicon is silane ($\mathrm{SiH_4}$). Silane decomposes at temperatures above 450°C. Theoretically such high temperatures are suitable for the growth of *a*-Si films, however, these layers incorporate a high defect density and are not capable for the fabrication of high-efficiency *a*-Si/*c*-Si heterojunction solar cells. The most common way for the deposition of high-quality (low defect) *a*-Si:H is by plasma enhanced chemical vapor deposition (PECVD).[3] The lowest defect concentrations are commonly found for deposition temperatures around $200\,^\circ\mathrm{C}$ and low power. In this study, a parallel-plate reactor with an excitation frequency of $f = 13.56\,\mathrm{MHz}$, a deposition temperature of $\vartheta_{\mathrm{dep}} = 200\,^\circ\mathrm{C}$

---

[2]Also low-temperature depositions with a subsequent annealing step or hydrogen plasma post treatment are suitable for the fabrication of high-quality *a*-Si:H layers.

[3]There is a comprehensive pool of different PECVD deposition techniques that are all suitable to produce high-quality *a*-Si:H, e.g. very-high-frequency PECVD [52], hot-wire CVD [53], inductively coupled PECVD, electron cyclotron resonance CVD.
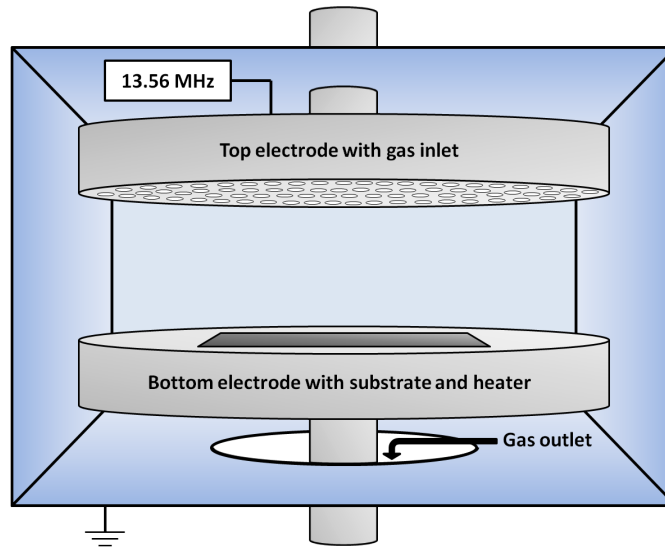
Figure 1.6: Schematic drawing of a typically used parallel-plate plasma-enhanced chemical vapor deposition (PECVD) reactor.

and a plasma power of $P = 20\,\text{W}$, corresponding to a power density of $35\,\text{mW/cm}^2$ was used. Fig. 1.6 shows a schematic drawing of a typically used parallel plate PECVD reactor.

The growth conditions during the deposition are important, because they influence the material and electronic properties of the *a*-Si:H layers, but the exact microscopic mechanisms [54, 55, 56] and connections between the growth parameters and the *a*-Si properties are still discussed [57, 58]. However, the main deposition parameters and their effects on the film growth can be roughly summarized as:

1. The **deposition pressure** typically lies between 0.1-1 mbar. The deposition pessure mainly determines the free path length of the ions and radicals in the plasma and thereby if the reactions take place on the sample surface or in the gas.

2. The **gas flow rate** determines the residence time in the reactor and thereby the duration of the reaction.

3. The **RF power** determines the dissociation rate of the gas which is directly linked to the film growth rate.

4. The **substrate temperature** influences the chemical reactions on the sample surface.

5. The **hydrogen dilution** influences if the film rather tends to grow amorphously or with a micro-crystalline structure.

Gas phase reactions

In the PECVD process, accelerated electrons collide with molecules of the reaction gas. The molecules can be excited into higher states and recombine again to the ground state by emission of photons that results in the typical plasma glow. Typical temperatures of exited molecules in higher vibrational or rotational states are $300 - 850$ K, which corresponds to energies around 0.1 eV, whereas the electrons can have temperatures in the range of $10^4 - 10^5$ K, which corresponds to energies of 1-10 eV. During the amorphous silicon deposition many different reactions take place, however, the most important mechanisms are the dissociation reactions of SiH_4 molecules in the plasma by the accelerated electrons [59, 60, 61]:

1. $SiH_4 \rightarrow SiH_2 + H_2$ (2.2 eV),

2. $SiH_4 \rightarrow SiH_3 + H$ (4 eV),

3. $SiH_4 \rightarrow Si + 2\,H_2$ (4.2 eV).

The average free path length of the ions is 0.001-0.01 cm, whereas the electrode plate distance is commonly in the range of 1-5 cm. Consequently, most of the reactions take place in the reactor volume during the diffusion to the substrate. Most of the collisions occur with other SiH_4 molecules since the content of ions or radicals is only about $0.1\,\%$. Hence, the SiH_2 molecules are quickly removed due to the processes:

4. $SiH_2 + SiH_4 \rightarrow Si_2H_6$ and

5. $SiH_2 + Si_2H_6 \rightarrow Si_3H_8$.

The SiH_3 ions are more stable against collisions with SiH_4 [62] and therefore are the dominant species for most deposition conditions [63, 64]. These SiH_3 ions can only detach to dangling bonds (Si-) at the growing surface of the substrate, but usually the entire surface is diluted by hydrogen. Hence, reactions are needed to remove the hydrogen atoms and create dangling bonds. Possible reactions are [65]:

6. $Si\text{-}H + SiH_3 \rightarrow Si\text{-} + SiH_4$ or

7. $Si\text{-}H + H \rightarrow Si\text{-} + H_2$.

The requirements to obtain high-quality *a*-Si:H, i.e a dense and lowly strained film, is a highly hydrogen-saturated substrate surface, and SiH_3 as the dominant species in the plasma. In this case, SiH_3 has a long diffusion length on the substrate surface and can find the energetically best places to attach to the growing film [66]. Instead, SiH_2 would stick very fast to the surface due to the reaction $Si\text{-}H + SiH_2 \rightarrow Si\text{-}SiH_3$, and therefore produce weakly bonded, highly strained films. Consequently, the deposition rates for high-quality *a*-Si:H are low.

However, very high hydrogen dilutions, and thus a very high hydrogen saturation of the substrate surface, can lead to undesired epitaxial growth [67, 58]. Further,
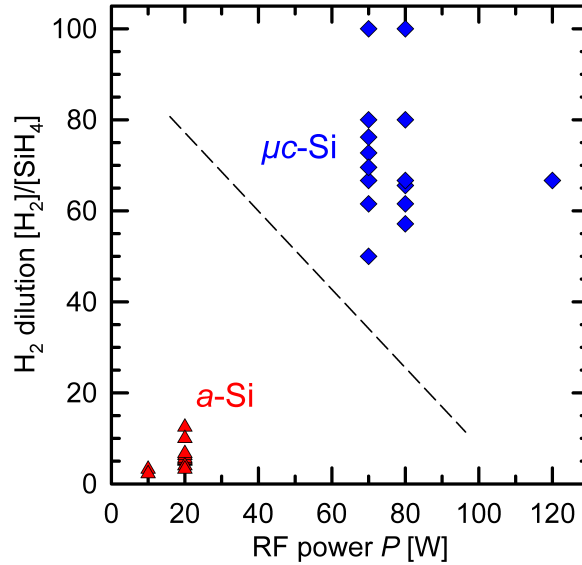
Figure 1.7: Growth conditions for amorphous and micro-crystalline silicon depend on the hydrogen dilution and the plasma power. The red triangles represent *a*-Si:H depositions, and the blue diamonds represent μc-Si depositions in our PECVD deposition tool. The dashed line is a guide to the eye and denotes the transition between *a*-Si:H and μc-Si growth. The exact transition depends also on other deposition parameters like temperature, pressure and doping.

this epitaxial growth is promoted by high plasma powers, especially on (100) surfaces [68, 69]. The extreme case of film relaxation is the growth of μ-*c*-Si [70]. Fig. 1.7 shows data points for samples which are deposited in our CS 400 P PECVD deposition tool with varying hydrogen dilutions and RF powers. The red triangles represent depositions that lead to *a*-Si:H growth, whereas the blue diamonds represent depositions that lead to μc-Si growth, determined with Raman spectroscopy measurements. The dashed line is a guide to the eye and denotes the transition between *a*-Si:H and μc-Si growth. The exact transition depends on other deposition parameters like temperature, pressure and doping. Fig. 1.8 shows the Raman crystallinity [71, 72] of the deposited film as a function of the hydrogen dilution. For higher hydrogen dilutions the crystallinity increases.

1.2.5 Doping of amorphous silicon

The doping mechanism in *a*-Si is fundamentally different from that in *c*-Si. In the perfect *c*-Si lattice, all silicon atoms are fourfold coordinated and impurities are constraint to have the same coordination number. For phosphorus and boron that leads to substitutional doping, which is the release of an electron or hole to the conduction or valence band, respectively.
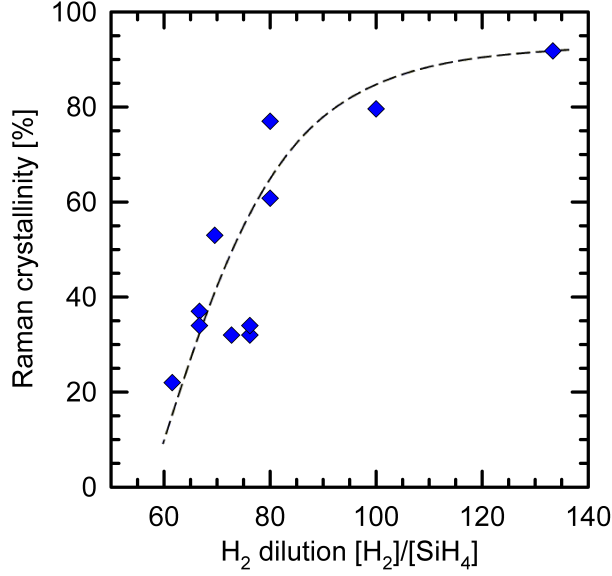
Figure 1.8: Measured Raman crystallinity as a function of the hydrogen dilution during the PECVD deposition process. The crystallinity increases with increasing hydrogen dilution for fixed other deposition parameters ($P = 120\,\mathrm{mW/cm^2}$, $d_\mathrm{electrode} = 13\,\mathrm{mm}$, $p = 3\,\mathrm{mbar}$, $\vartheta = 220\,°\mathrm{C}$). The dashed line is a guide to the eye.

In contrast to the silicon crystal, the amorphous silicon network allows the incorporation of atoms with any coordination number. Thus, it could be expected that phosphorus and boron are incorporated with their preferred coordination number and therefore have no doping character. However, there must be a doping mechanism, since the first doping of a-Si was reported by Spear and LeComber in 1975 [73]. They used PH_3 and B_2H_6 as precurser gases for the doping with phosphorus and boron, respectively. Today, the gas phase doping with PH_3 and B_2H_6 as precurser gases is still the most common application for the doping of a-Si layers.

As theoretically predicted, most of the phosphorus or boron atoms are incorporated with a threefold coordination and do not contribute to the doping. However, a small but reasonable concentration of phosphorus and boron is incorporated with a fourfold coordination due to the reaction:

$$Si_4^0 + P_3^0 \rightarrow Si_3^- + P_4^+ \,. \tag{1.3}$$

In this case, Si_4^0 stands for a fourfold silicon atom with zero net charge, and the other symbols accordingly. In this reaction, a neutral threefold phosphorous atom is ionized by giving away one of its electrons. Consequently, it then has four remaining valence electrons and can be incorporated with a fourfold coordination. In most of the cases, a negatively charged dangling bond Si_3^- is created with the free electron. Consequently, by increasing the dopant concentration, also the
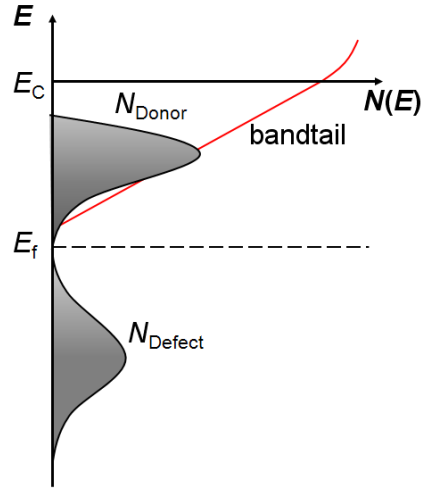
17

Figure 1.9: Schematic representation of the donor and defect densities in *n*-*a*-Si:H.

defect concentration deep in the mobility gap increases (see Fig. 1.9) [74]. This effect "pins" the Fermi level in the mobility gap and prevents it to approach the mobility edges even at very high doping concentrations. It was found that the closest distance of the Fermi level to the valence and conduction bands can be 0.3 eV and 0.15 eV, respectively [73, 75]. Therefore, the doping process of *a*-Si is a self-compensating process.

Whereas in *c*-Si the doping efficiency is almost independent of the impurity concentration with a value of one up to the solubility level, in *a*-Si the doping concentration is much lower. Only about 1 % of the phosphorus or boron atoms are incorporated as fourfold donor or acceptor states. Only approximately 10 % of these donors or acceptors are not compensated by deep defects, i.e. dangling bonds. Only 10 % of these remaining donors or acceptors do not occupy localized states at room temperature, i.e. enough thermal energy is present, so that the charge carriers are in conductive states above (electrons) or below (holes) the mobility edges.[4] Hence, the overall doping efficiency, measured in terms of free electron or hole concentration, is only in the range of 10^{-4}.

The deposition rate of phosphorus- or boron-doped *a*-Si strongly depends on the species and ratios of the precursor gases. For example, a gas phase concentration of only 1 % boron leads to a 40 % higher deposition rate. The reason for the increased deposition rate with boron in the gas phase is not yet fully understood. Boron radicals in the gas phase may promote the formation of silane radicals or the attachment of silicon atoms to the surface by promoting a faster release of hydrogen from the growing surface [77]. Instead, for phosphorus doping this effect is not

---

[4]In *c*-Si, the energetic distances of the phosphorus and boron states to the band edges are 40 meV and 45 meV, respectively [76]. In *a*-Si the energetic distance of the phosphorus and boron states to the band edges are ≈100 meV and broadly distributed.

so pronounced. For our standard deposition parameters we measure deposition rates of $0.22\,\mathrm{nm/s}$ for intrinsic a-Si:H, $0.25\,\mathrm{nm/s}$ for phosphorus-doped n-a-Si:H, and $0.47\,\mathrm{nm/s}$ for boron-doped p-a-Si:H.

1.2.6 The metastability of amorphous silicon

In 1977 Staebler and Wronski discovered that the electronic properties of a-Si:H degrade upon illumination [78, 79]. The Steabler Wronski effect (SWE) describes the increase of the dangling bond defect density upon intense illumination to values up to $N_\mathrm{db} = 10^{17}\,\mathrm{cm}^{-3}$ and therefore negatively influences the performance of SHJ solar cells. However, by annealing at $150\,^{\circ}\mathrm{C}$ this effect is reversible. Therefore, the SWE describes a metastable change of the properties of the a-Si:H. Stutzmann found that the dangling bond density N_db can be described by the generation rate G and the exposure time t [80]:

$$N_{db}(t) \propto G^{2/3} \cdot t^{1/3}\,. \tag{1.4}$$

The SWE is affected by the hydrogen content and bonding structure, by the disorder in the a-Si:H network, and by the concentration of impurities. The exact microscopic mechanisms are still under discussion. Two famous models are the "hydrogen bond switching model" [80] and the "hydrogen collision model" [81]. These models have in common that photo generated charge carriers recombine non-radiatively and their energy is transferred to break up Si-Si or Si-H bonds.

1.3 Transparent conductive oxides for the use in SHJ solar cells

The lateral conductivity of the a-Si:H layers is very poor. Therefore, a conductive layer is needed to transport the collected charge carriers to the fingers of the metalization grid on the front side of the SHJ solar cell. For bifacial solar cells this is also the case for the rear side. When applied to the front side of the solar cell, the layer also needs to be transparent and act as anti-reflection. For this purpose, transparent conductive oxide (TCO) layers are used for the fabrication of SHJ solar cells.

There are several materials that could be used for the fabrication of SHJ solar cells, e.g. aluminum- or boron-doped zinc oxide (ZnO:Al/ZnO:B), indium tin oxide (ITO), or indium tungsten oxide (IWO). The most common TCO for SHJ solar cells is ITO ($\mathrm{In_2O_3}$:Sn) and the most common deposition technique is sputtering. The scanning electron microscope (SEM) cross section in Fig. 1.10 shows the typical columnar growth of a sputtered ITO layer. In a parallel study to this thesis, different TCOs where investigated at ISFH also [82]. However, it was found that ITO provides the best performance on our SHJ solar cell. Therefore, in this thesis solely ITO was used as TCO layer.
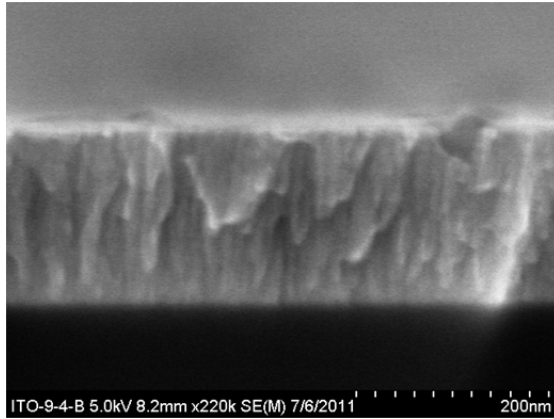
Figure 1.10: SEM cross section of an ITO layer. The image shows the typical columnar growth of ITO during sputtering.

The ITO sputter target consists of 90% indium (III) oxide (In_2O_3) and 10% tin (IV) oxide (SnO_2). Argon is used as sputter gas and oxygen is added to adjust the doping. Recent studies show that the addition of hydrogen to the plasma can further increase the conductivity of the ITO by increasing the mobility of the charge carriers. Typical transmittance and reflection data of our ITO layers for different deposition parameters are shown in Fig. 1.11. The green curve represents the typical ITO used in this study. The red curve represents an ITO film with the addition of hydrogen during sputtering. The higher transmittance of the red curve in the lower wavelength range stems from a higher charge carrier density in the conduction band, leading to a higher effective band gap for optical transitions (Burstein Moss shift).

Typical ITO layers used for the fabrication of SHJ solar cells provide lateral conductivities of $\approx 5000\,^{S}/_{cm}$ and an average transmittance of $\approx 80\,\%$ in the relevant wavelength regime [83, 84]. However, a trade off has to be found between good conductivity and high transmittance. The more charge carriers are present in the conduction band, the higher is the free carrier absorption, and consequently the transmittance decreases. The refractive index for ITO lies around $n_{ITO} = 2$ over a broad wavelength range. Therefore, the requirement for a good amplitude matching, i.e. $n_{ITO} = \sqrt{n_{air} \cdot n_{Si}}$, with $n_{air} = 1$ and $n_{Si} = 3.8$ is relatively well fulfilled. For phase matching reasons the typical layer thickness is $100\,\mathrm{nm}$. The ITO is deposited at temperatures below $200\,°C$ to avoid permanent damaging of the a-Si:H layers. However, often the a-Si:H passivation quality suffers from ion bombardment during the ITO sputtering process, but can be brought to the initial value again after a short annealing step at temperatures of $150 - 200\,°C$.

The ITO layer also functions as a barrier between the a-Si:H layer and the front and rear side metalization. That is necessary because the a-Si:H and the metal could easily react and drastically decrease the passivation quality of the a-Si:H layer. Additionally, the ITO layer must provide a good electrical contact to the
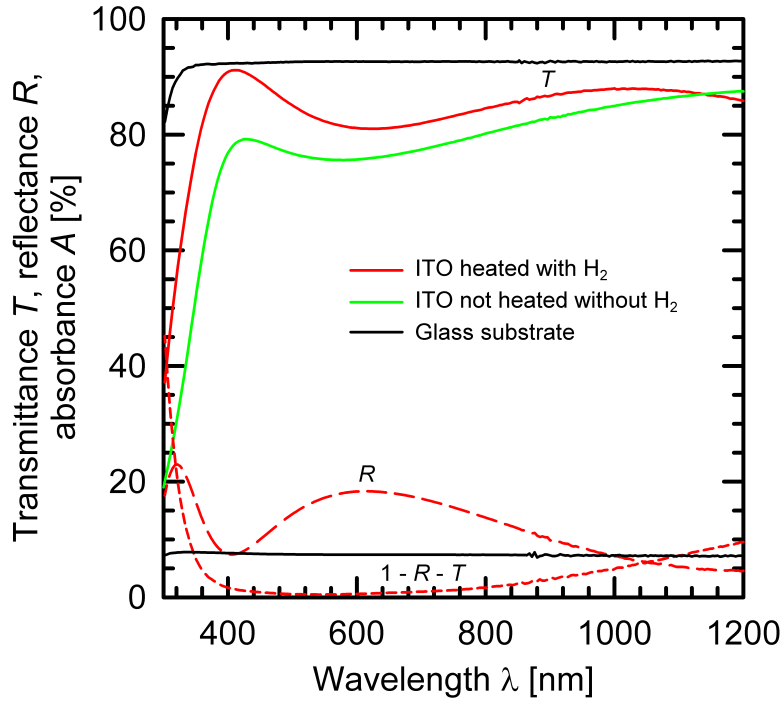
Figure 1.11: Measured transmittance and reflection data for ITO layers. The green curve represents the ITO used in this study. The red curve represents an ITO sputtered with the addition of hydrogen at 200 °C substrate temperature. The higher transmittance of the red curve in the lower wavelength range stems from a higher charge carrier density in the conduction band, leading to a higher effective band gap for optical transitions (Burstein Moss shift).

a-Si:H layers and the front and rear side metalization. ITO is a heavily doped n-type semiconductor with a band gap of about $4\,\mathrm{eV}$. The electrical contact to the n-a-Si:H layers is therefore expected to be better than the contact to the p-a-Si:H layers. The analysis of the contact resistance of the a-Si:H/ITO interface is one main focus of this work and will be discussed in more detail in Chapter 5.

Characterization techniques

In this Chapter, the measurement techniques applied in this thesis will be briefly described. First, the current-voltage characteristics of a solar cell are discussed in section 2.1. Secondly, photoconductance decay methods to determine the charge carrier lifetime are presented in Section 2.2. Finally, Section 2.3 describes the quantum efficiency measurement of a solar cell.

2.1 Current voltage characteristics

In this Section the measurement of the current-voltage (J-V) characteristics of a solar cell is discussed. All J-V curves presented in this thesis are measured using the LOANA tool of PV-tools [85]. For the measurement the solar cell is placed on a brass chuck, which contacts the rear side of the solar cell. Its temperature during the measurements is kept constant at a value of $\approx 25\,°\mathrm{C}$. The front grid is contacted with needles on the busbar. In this way, the current through the device can be measured for different applied voltages under illumination or in the dark.

2.1.1 Recombination characteristics

In solar cells, different recombination mechanisms are present in parallel. The voltage-dependent total recombination current density $J_{\mathrm{rec}}(V)$ can be described by the sum of the various contributions:

$$J_{\mathrm{rec}}(V) = \sum_i J_{0,\mathrm{i}} \left[\exp\left(\frac{q \cdot V}{n_{\mathrm{i}} \cdot kT} \right) - 1 \right] . \qquad (2.1)$$

Here, $J_{0,\mathrm{i}}$ are the saturation current densities, n_i are the ideality factors of the diode, q is the elementary electric charge, k is the Boltzmann factor and T is the absolute temperature in Kelvin. The ideality factors n_{i} are dependent on the specific recombination mechanisms. An ideality factor of $n = 1$ is obtained for
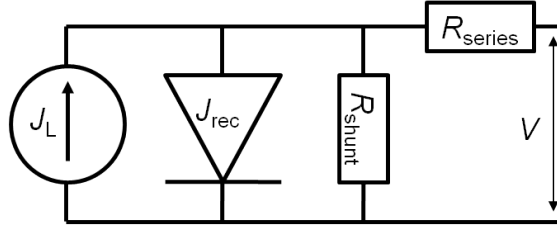
Figure 2.1: One-diode circuit diagram of a solar cell.

band-to-band and Shockley-Read-Hall (SRH) recombination in low-level injection. An ideality factor of $n = 2$ is obtained for SRH recombination in high-level injection and recombination in the space charge region, where $n = p$. An ideality factor of $n = 2/3$ is obtained for Auger recombination. In reality, the ideality factor often is voltage-dependent, depending on which recombination path dominates the *J-V* curve of an actual solar cell. Also a mix of different ideality factors is observable, if different recombination mechanisms are present at the same time.

2.1.2 Illuminated *J-V* characteristics

The general *J-V* curve under illumination of a solar cell can be described by the subtraction of the recombination current density J_{rec} from the photogenerated current density J_{L}, considering the series resistance R_{s} and the shunt resistance R_{sh}:

$$ J(V) = J_{\text{L}} - J_{\text{rec}}(V) = J_{\text{L}} - \sum_i J_{0,i} \left[\exp\left(\frac{q(V - R_{\text{s}} \cdot J)}{n_{\text{i}} \cdot kT} \right) - 1 \right] - \frac{V + R_{\text{s}} \cdot J}{R_{\text{sh}}} . \quad (2.2) $$

A schematic one-diode circuit diagram of a solar cell is given in Fig. 2.1. A typical *J-V* curve is shown in Fig. 2.2 for $J_{\text{L}} = 38\,{}^{\text{mA}}\!/\text{cm}^2$, $J_0 = 100\,{}^{\text{fA}}\!/\text{cm}^2$, $R_{\text{s}} = 2\,\Omega\text{cm}^2$, $R_{\text{sh}} = 10000\,\Omega$, and $n = 1$. Under short-circuit conditions the voltage is zero, $V = 0$, and the current is the short-circuit current density $J = J_{\text{SC}}$. Under open-circuit conditions the current is zero, $J = 0$, and the voltage is the open-circuit voltage $V = V_{\text{OC}}$. The output power is calculated by the product $J \times V$. The point where $J \times V = maximum$ is defined as the maximum power point (MPP). The Fill factor of the *J-V* curve is defined as:

$$ FF = \frac{V_{\text{MPP}} \cdot J_{\text{MPP}}}{V_{\text{OC}} \cdot J_{\text{SC}}} . \quad (2.3) $$

The *FF* is directly dependent on the ideality factor, i.e. the shunt and series resistance, as well as the recombination mechanisms taking place in the solar cell.
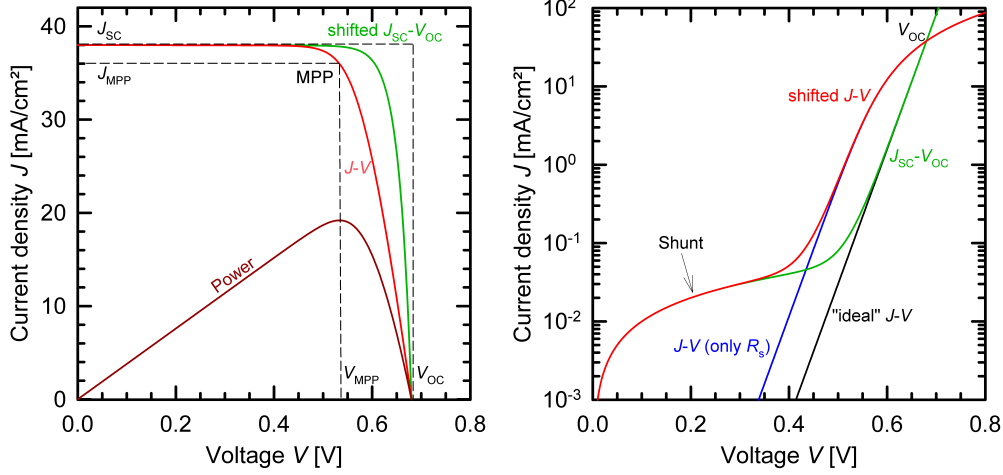
Figure 2.2: Calculated J-V curves for typical solar cell parameters; $J_{\mathrm{L}} = 38\,\mathrm{mA/cm^2}$, $J_0 = 100\,\mathrm{fA/cm^2}$, $R_{\mathrm{s}} = 2\,\Omega\mathrm{cm}$, $R_{\mathrm{sh}} = 10000\,\Omega\mathrm{cm}$, and $n = 1$. The left graph shows the light J-V curve (red line) and the J_{SC}-V_{OC} curve shifted by J_{SC} in a linear scale (green line). The difference between the two curves stems from the series resistance contribution. The right graph shows the J_{SC}-V_{OC} curve and the J-V curve shifted by J_{SC} in a logarithmic scale. Here the influence of the shunt resistance is visible.

The maximum "ideal" fill factor FF_0 without series or shunt resistances can be expressed as a function of the ideality factor and the voltage [86]:

$$FF_0 = \frac{v_{\mathrm{OC}} - ln(v_{\mathrm{OC}} + 0.72)}{v_{\mathrm{OC}} + 1} \qquad \text{with} \qquad v_{\mathrm{OC}} = \frac{q \cdot V_{\mathrm{OC}}}{n \cdot kT}. \qquad (2.4)$$

The left graph in Fig. 2.3 shows the FF_0 as a function of the ideality factor n for fixed open circuit voltages V_{OC}. The right graph in Fig. 2.3 shows the FF_0 as a function of the open-circuit voltage V_{OC} for fixed ideality factors n. The unique feature of SHJ solar cells is the very high V_{OC} potential, and therefore a high fill factor potential. However, unfortunately the transport across the hetero-interface often leads to ideality factors of approximately $n = 1.2$ [21], which leads to a reduction in the fill factor.

The solar cell conversion efficiency η is given by:

$$\eta = \frac{V_{\mathrm{MPP}} \cdot J_{\mathrm{MPP}}}{\phi}. \qquad (2.5)$$

Here ϕ is the irradiation power, which is $100\,\mathrm{mW/cm^2}$ for the AM 1.5 G spectra at 1 sun intensity. The efficiency η becomes maximal for minimal saturation current density J_0, ideality factor n and series resistance R_{s}, and for maximal shunt resistance R_{sh}.
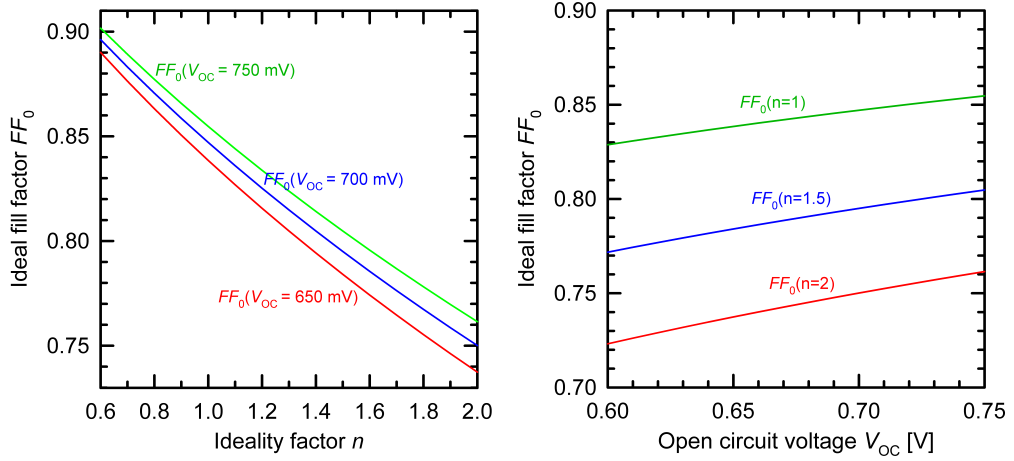
Figure 2.3: The left graph shows FF_0 as a function of the ideality factor n for fixed open circuit voltages V_{OC}. The right graph shows the FF_0 as a function of the open circuit voltage V_{OC} for fixed ideality factors n. The FF_0 increases for higher voltages or lower ideality factors.

2.1.3 $J_{SC}(V_{OC})$ characteristics

During the $J_{SC}(V_{OC})$ measurement, pairs of values of the short-circuit current density J_{SC} and the open-circuit voltage V_{OC} are taken at different illumination intensities. In this case, the photogenerated current density J_L equates the short-circuit current density J_{SC}. Under open-circuit conditions no current flows $J(V_{OC}) = 0$ and therefore the $J_{SC}(V_{OC})$ curve is not affected by any series resistance of the solar cell. Hence, the difference between the $J_{SC}(V_{OC})$ and the $J(V)$ curve measured under illumination solely stems from the series resistance R_s. The $J_{SC}(V_{OC})$ curve can be described by:

$$J_{SC} = \sum_i J_{0,i} \left[\exp \left(\frac{q \cdot V_{OC}}{n_i \cdot kT} \right) - 1 \right] + \frac{V_{OC}}{R_{sh}} \,. \tag{2.6}$$

In order to compare the $J_{SC}(V_{OC})$ curve with the $J(V)$ curve, one of the curves has to be shifted by J_{SC} to lie in the same quadrant of the graph. In Fig. 2.2, a comparison of both curves is shown. The difference stems from a series resistance of $R_s = 2\,\Omega\text{cm}^2$. The $J_{SC}(V_{OC})$ curve has an interception with the $J(V)$ curve at $V = V_{OC}$. At this point both curves are under the same illumination level and no current flows into or out of the solar cell. According to the $J(V)$ curve under illumination, a pseudo fill factor pFF can be defined as:

$$pFF = \frac{max(V_{J_{SC}(V_{OC}),\text{shifted}} \cdot J_{J_{SC}(V_{OC}),\text{shifted}})}{V_{OC} \cdot J_{SC}} \,. \tag{2.7}$$

The *pFF* gives the fill factor of a solar cell if no series resistance would be present. In the same way, a pseudo efficiency *pseudo η* can be defined as:

$$pseudo\,\eta = \eta \frac{pFF}{FF} \, . \tag{2.8}$$

Hence, the $J_{\mathrm{SC}}(V_{\mathrm{OC}})$ gives a measure for the solar cell performance if no series resistance would be present.

2.2 Photoconductance lifetime measurements

Photoconductance-based measurement techniques are widely spread methods to determine the effective lifetime of excess carriers in semiconductors [87]. The sample is placed on top of a coil and in this way is inductively coupled to an oscillator circuit that responds to changes of the samples' conductivity. By flashing the sample with a flash light, excess carriers are generated and the change of the conductivity of the sample is logged. At the same time, the intensity of the flash light is logged by monitoring a calibrated reference cell. In general, the carrier concentration is a function of the position in the wafer. The conductivity σ of the wafer can be written as:

$$\sigma = \frac{q}{W} \cdot \int_0^W (n\,\mu_n + p\,\mu_p)\,\mathrm{d}z, \tag{2.9}$$

where q is the elementary charge, W is the sample thickness, n and p are the electron and hole concentrations, and μ_n and μ_p are the electron and hole mobilities which are themselves dependent on the electron and hole concentrations. The total conductivity σ of the wafer is the sum of the conductivity induced by the photogenerated excess carriers $\Delta\sigma$ and the dark conductivity σ_{dark} of the sample, which is measured before the flash light is triggered, i.e. $\sigma = \sigma_{dark} + \Delta\sigma$. The quantity of interest is the excess carrier density Δn. By using an IR filter for the flash light, the distribution of the photogenerated carriers in the wafer can be assumed to be homogeneous. Assuming that $\Delta n = \Delta p$, Eq. 2.9 can then be simplified to:

$$\Delta n = \frac{\Delta\sigma}{q(\mu_n + \mu_p)} \, . \tag{2.10}$$

Because the mobilities μ_n and μ_p are themselves dependent on the electron and hole concentrations, an iterative procedure is necessary to obtain Δn with a charge carrier-dependent mobility model [88].

The time dependence of the excess carrier density Δn is given by the continuity equation:

$$\frac{\partial \Delta n}{\partial t} = G(t) - U(t) + \frac{1}{q}\nabla J, \tag{2.11}$$

where $G(t)$ is the generation rate, $U(t)$ the recombination rate, and J the current density. However, when considering a homogeneous photogeneration in the wafer and well passivated surfaces, the carrier density in the sample can be assumed to be spatially uniform and the last term in Eq. 2.11 can be neglected. The recombination rate can be written as $U = \Delta n / \tau_{\mathrm{eff}}$, where τ_{eff} is the effective carrier lifetime, which results in the following expression for τ_{eff}:

$$\tau_{\mathrm{eff}} = \frac{\Delta n}{G(t) - \frac{\partial \Delta n}{\partial t}}. \tag{2.12}$$

The generation rate $G(t)$ is determined from the calibrated reference solar cell:

$$G(t) = \frac{\phi(t) \, f_{\mathrm{abs}} \, J_{\mathrm{SC}}^{1sun}}{q \, W}, \tag{2.13}$$

with the intensity of the incoming light $\phi(t)$ measured by the calibrated reference cell, the short-circuit current density J_{SC}^{1sun} of the reference cell at 1 sun intensity, and the absorption coefficient f_{abs}, which takes into account different optical properties of the samples, e.g. antireflection coatings, and textured or planar surfaces.

2.2.1 Quasi-steady-state conditions

If the decay constant of the flash light is much longer compared to the carrier lifetime of the sample, the sample is to a good approximation in steady-state conditions during the measurement. In this case, the generation rate and the recombination rate are balanced and the lifetime can be written as:

$$\tau_{\mathrm{eff}} = \frac{\Delta n}{G}. \tag{2.14}$$

However, in order to correctly estimate the generation rate, the optical constant f_{abs} has to be known. This version of the measurement technique is also known as quasi-steady-state photoconductance (QSSPC) method.

2.2.2 Transient conditions

In the transient mode, the measurement starts after the flash has been switched off, i.e. $G = 0$. In this case, knowledge of the optical properties of the sample is not required. The lifetime can then be written as:

$$\tau_{\mathrm{eff}} = \frac{\Delta n}{-\frac{\partial \Delta n}{\partial t}}. \tag{2.15}$$

However, the excess carrier lifetime has to be much longer compared to the time needed to switch off the light source. This is the case for silicon wafers deposited

with well passivating *a*-Si:H layers. For this reason, the lifetime data presented in this thesis are measured under these conditions, which are also known as photoconductance decay (PCD) method.

2.2.3 Implied *J*-*V* characteristics

The result from a lifetime measurement is the excess carrier-dependent effective lifetime $\tau_{\text{eff}}(\Delta n)$. These data can be translated into an *implied J-V* curve. An implied voltage V_{impl} can be calculated from the excess charge carrier density Δn. Rearranging

$$n\,p = n_{\text{i}}^2 \ \exp\left(\frac{q\,V_{\text{impl}}}{k\,T}\right) \tag{2.16}$$

leads to:

$$V_{\text{impl}} = \frac{k\,T}{q} \ \ln\left(\frac{n\,p}{n_{\text{i}}^2}\right) = \frac{k\,T}{q} \ \ln\left(\frac{(n_0 + \Delta n)\,(p_0 + \Delta n)}{n_{\text{i}}^2}\right) . \tag{2.17}$$

This V_{impl} can be plotted against the light intensity ϕ measured in suns, which again can be translated into an implied current density J_{impl} of the measured sample. When shifting this curve by an estimated J_{SC}, the implied open-circuit voltage $V_{\text{OC,impl}}$, implied ideality factor n_{impl}, implied fill factor FF_{impl}, and implied efficiency η_{impl} can be determined equivalently to a "real" *J-V* curve.

In this way, the potential of different passivation layers and their influence on the solar cell performance can be investigated, even very early in the production process. A drawback of this method applied to conventional homojunction solar cells is the fact that the very last production step is the metalization. Because the V_{OC} of these solar cells is mainly dominated by the highly recombination active metal/*c*-Si contacts, the final V_{OC} of these solar cells cannot directly be determined by this method during the process. However, that is different for SHJ solar cells, because here the metalization is decoupled from the active solar cell. Therefore, this method is well suited for monitoring the SHJ solar cell fabrication and analyze the influence of each process step on the final solar cell performance.[1] This method gives a very good prediction of the parameters of the finished solar cell, except the resistive losses. Consequently, the *implied J-V* curve of the SHJ solar cell after each process step should be equal to the J_{SC}-V_{OC} curve of the finished solar cell.

2.2.4 *Suns*-V_{OC} measurements

The *Suns*-V_{OC} method measures the pseudo *J-V* curve of a solar cell or a solar cell precursor. The sample is placed on a brass table, which provides the back contact. The front side is contacted with a metal needle, and hence the voltage is

---

[1]After the metalization the solar cells cannot be measured by inductively coupled photoconductance techniques, because the charge carriers in the metal grid totally dominate the measured conductivity signal.

measured locally around the tip. The generation rate is determined from a separated reference cell, in opposite to the J_{SC}-V_{OC} method, where the generation is measured on the solar cell itself. Because the illumination intensity is proportional to the photogeneration rate in the probed cell, only a proportional factor is needed between the illumination intensity measured with the reference cell and the photogeneration rate of the test sample. This factor could e.g. be obtained from optical simulations, as presented in Chapter 4.

An advantage of the *Suns*-V_{OC} measurement technique compared to the J_{SC}-V_{OC} method is that even extremely high series resistances that would even affect the J_{SC} have no impact on the measured *Suns*-V_{OC} curve. Hence, it is possible to measure solar cell precursors with very high series resistances, e.g. solar cells without metalization grid, by just putting the contact needle onto a highly doped region. For our SHJ solar cells, this technique can e.g. be used after the ITO deposition before the metalization. In this way, a real voltage measurement can be performed without the influence of the metalization grid.

2.3 Quantum efficiency measurements

The external quantum efficiency (EQE) of a solar cell is the ratio of collected charge carriers $N_{electron}$ at the contacts and the number of irradiated photons N_{photon} of a certain wavelength:

$$EQE = \frac{N_{electron}(\lambda)}{N_{photon}(\lambda)} = \frac{J_{SC}(\lambda)}{J_{photon}(\lambda)} \, , \tag{2.18}$$

where J_{photon} is the "ideal" current density if no reflection or recombination losses would be present. If all irradiated photons are absorbed and transfered into charge carriers that are collected at the contact, the quantum efficiency is unity, $EQE = 1$. Photons with energies below the energy of the band gap cannot be absorbed, hence, the EQE is zero for photons with energies $E_{photon} < 1.12$ eV ($\lambda > 1200$ nm).

The EQE measurements in this thesis are performed with a LOANA system of PV-tools [85]. During the measurements, the contacted solar cell lies on a brass chuck, which temperature is kept constant at a value of $\approx 25\,°\mathrm{C}$. A $2 \times 2\,\mathrm{cm}^2$ area of solar cell is then illuminated with different wavelengths and the current at the contacts is measured under short-circuit conditions.

The EQE gives information about different loss mechanisms in a solar cell. Photons of short wavelengths are mainly absorbed near the front surface of the solar cell. Hence, the short wavelengths regime gives information about the front side of the solar cell, e.g. passivation quality of the front surface or absorption in front layers. Accordingly, the long wavelengths regime gives information about the rear side of the solar cell. The mid wavelengths regime contains information about the bulk and rear side recombination. The EQE includes also reflection R and
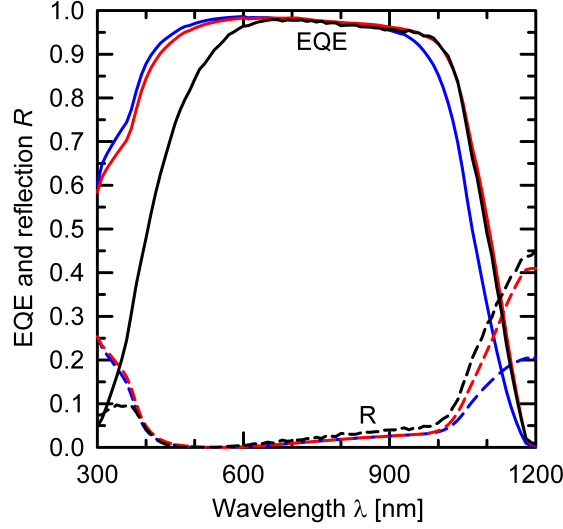
Figure 2.4: Typical EQE (solid line) and *R* (dotted line) data for an Al-BSF (blue line), a PERC (red line), and a SHJ solar cell (black line). The low *EQE* in the short wavelengths regime of the SHJ solar cell stems from absorption in the front *a*-Si:H and TCO layers. The low *EQE* in the long wavelength regime of the Al-BSF solar cell stems from a less efficient passivation of the aluminum BSF at the back side of the solar cell.

transition *T* losses. Compared to "standard" solar cells, SHJ solar cells also suffer from parasitic absorption in the *a*-Si:H and TCO layers.

Typical EQE (solid line) and *R* (dotted line) data for an Al-BSF solar cell, a PERC solar cell, and a SHJ solar cell are shown in Fig. 2.4. The SHJ solar cell shows a poor *EQE* in the short wavelengths regime compared to the other two solar cells. The relatively low *EQE* in the short wavelengths regime stems from absorption in the front *a*-Si:H and TCO layer. However, the SHJ solar cell shows a high *EQE* in the long wavelengths regime, due to excellent surface passivation of the rear side. Both, the Al-BSF and the PERC solar cells show a high *EQE* at low wavelengths. However, the Al-BSF solar cell shows a lower *EQE* at high wavelengths, due to a poorer passivation of the Al-BSF at the rear side.

The internal quantum efficiency (*IQE*) is defined as the ratio of collected electrons at the contacts under short-circuit conditions and the photons that are absorbed in the solar cell, at a certain wavelength. Hence, the IQE is given by:

$$IQE = \frac{N_{\text{electron}}(\lambda)}{N_{\text{absorbed}}(\lambda)} = \frac{J_{\text{SC}}(\lambda)}{J_{\text{absorbed}}(\lambda)} = \frac{EQE(\lambda)}{1 - R(\lambda)} \,. \tag{2.19}$$

Optimization of *a*-Si:H layers for the application in silicon heterojunction solar cells

In this Chapter, a comprehensive optimization of the *a*-Si:H layers used for the fabrication of our silicon heterojunction solar cells is presented. First, a short description of the PECVD cluster system used for the deposition of the *a*-Si:H layers will be given. Then, lifetime optimization experiments of thin undoped *i*-*a*-Si:H layers as a function of the deposition parameters, as well as annealing and H_2 plasma post treatments, are presented. Subsequently, the doping efficiency of doped *n*-*a*-Si:H and *p*-*a*-Si:H layers will be investigated as a function of the gas phase doping of the dopant gas during the deposition process. In the last Section, the influence of the hydrogen dilution during the PECVD deposition on the passivation quality of *i*-*a*-Si:H layers will be studied in dependence of the crystal orientation of the wafer surface.

3.1 The PECVD deposition tool

A photograph of the deposition tool applied in this work (Cluster System CS 400P, von Ardenne, Germany) is shown in Fig. 3.1. The cluster system includes three separate PECVD process chambers with a parallel-plate setup. A schematic representation of one such process chamber is given in Fig. 1.6. Each individual process chamber is used for one specific type of doping, i.e. one chamber only for phosphorus doping of *n*-type *a*-Si:H, one chamber only for boron doping of *p*-type *a*-Si:H, and one chamber only for undoped intrinsic *a*-Si:H. In this way, cross contamination of the process gases diborane and phosphine can be avoided. This is of critical importance, especially considering the surface passivaton quality of the thin *i*-*a*-Si:H films. All three *a*-Si:H process chambers are connected to a transfer chamber in the center of the cluster tool. Also attached to the transfer chamber is a small load-lock chamber where the samples can be inserted into the

Figure 3.1: Photograph of the PECVD Cluster System CS 400 P (von Ardenne, Germany) used in this study.

deposition tool. For the handling and during the deposition the samples are placed on an aluminum carrier.

Each process chamber has its own carrier to avoid cross contamination. Wafers of a size up to $156 \times 156\,\mathrm{mm}^2$ can be homogeneously deposited in the cluster tool. The samples can be transfered with an automatic robot control to the process chambers. Two different frequency generators with 13.58 MHz or 81.25 MHz can be used in each process chamber. However, in this work only the 13.58 MHz excitation frequency was used. Besides the *a*-Si:H process chambers also a fourth process chamber is present for the deposition of SiN, SiO, AlO, as well as ZnO:B and ZnO:Al films. However, these layers are not topic of this thesis and therefore will not be further discussed.

A well defined wafer surface is crucial for the electronic passivation with *a*-Si:H [89]. Therefore, typically an RCA cleaning [90] is performed prior to the *i-a-*Si:H passivation layer deposition. The RCA cleaning sequence ends with a dip in hydrofluoric (HF) acid, which leaves an oxygen-free, hydrogenated surface. Between this HF-dip and the insertion into the vacuum of the deposition tool lies a time span of approximately 5 minutes. Also between two depositions, e.g. when both sides of a sample must be deposited or the process chamber and thus the carrier has to be changed, the samples are exposed to the ambient air for a certain time.
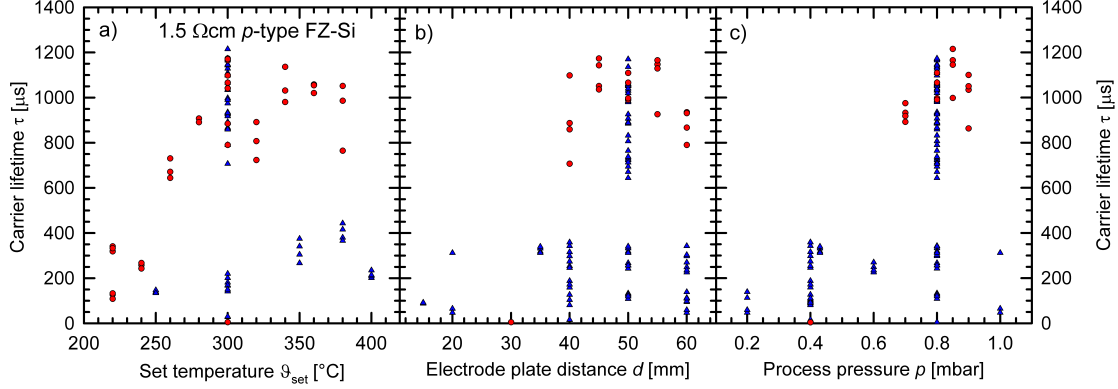
Figure 3.2: Carrier lifetime τ measured at an excess carrier density of $\Delta n = 5 \times 10^{15}\,\mathrm{cm}^{-3}$ as a function of a) the set-temperature ϑ_{set}, b) the electrode plate distance d, and c) the deposition pressure p. The red circles stem from depositions where only the investigated parameter was changed. The blue triangles stem from measurements where several process parameters were varied.

This fact will become important when analyzing the contact resistance through these layers later in this thesis (Section 5.2).

3.2 Lifetime optimization of *i*-*a*-Si:H passivation layers

3.2.1 Variation of deposition parameters

The main advantage of the SHJ solar cell concept is the outstanding open-circuit voltage potential, due to the excellent surface passivation properties of *i*-*a*-Si:H layers. However, the passivation quality is strongly influenced by the deposition conditions and hence by the process parameters. In this Section, the dependence of the deposition parameters on the passivation quality of thin *i*-*a*-Si:H layers is investigated. Therefore, the deposition pressure, the substrate temperature, the electrode distance and the gas composition have been varied on symmetrically processed lifetime samples. The silicon substrates are *p*-type float zone (FZ) wafers with a resistivity of $1.5\,\Omega\mathrm{cm}$ and a thickness of $300\,\mu\mathrm{m}$. Fig. 3.2 shows the effective lifetimes measured at an excess carrier density of $\Delta n = 5 \times 10^{15}\,\mathrm{cm}^{-3}$ as a function of a) the set-temperature ϑ_{set}, b) the electrode plate distance d, and c) the deposition pressure p. The red circles stem from depositions where only the investigated parameter was changed. The blue triangles stem from measurements where several process parameters were varied. The plasma power of $20\,\mathrm{W}$ and the hydrogen:silane ratio of 5:1 was kept constant for all processes. Each data point represents one sample. Presented are the initial lifetimes measured directly after the deposition.

The best lifetime results for the *i*-*a*-Si:H passivation layers are obtained for $\vartheta_{\mathrm{set}} = 300\,°\mathrm{C}$, $d = 50\,\mathrm{mm}$, and $p = 0.85\,\mathrm{mbar}$. Therefore, these parameters are

used as "standard" parameters for all following i-a-Si:H depositions. However, although the set-temperature is $\vartheta_{\mathrm{set}} = 300\,°\mathrm{C}$, the actual substrate temperature is considerably lower. The samples lie on an aluminum carrier located on top of the bottom electrode. Thus, the thermal contact between the $300\,°\mathrm{C}$ bottom electrode and the sample is weak. The actual sample temperature is therefore considerably lower than the set-temperature and is identified to be approximately $\vartheta_{\mathrm{sample}} \approx 200\,°\mathrm{C}$, as commonly found in literature for well-passivating a-Si:H layers.

3.2.2 Annealing of *a*-Si:H layers

In the fabrication of SHJ solar cells annealing steps may become necessary, e.g. for the curing of the damage induced by the ITO sputter process or for the drying of the screen-printed metal paste used to form the metallization grid. In this Section, the impact of an additional annealing step after the actual i-a-Si:H deposition on the surface passivation quality is investigated. Therefore $10\,\mathrm{nm}$ thin i-a-Si:H layers are deposited on p-type FZ wafers with a resistivity of $1.5\,\Omega\mathrm{cm}$ and a thickness of $300\,\mu\mathrm{m}$ at different temperatures. The samples were annealed on a hotplate in air at different annealing temperatures for 5 minutes.

Figure 3.3 shows lifetime data of four sets of samples deposited at different set-temperatures. A set-temperature of $\vartheta_{\mathrm{set}} = 300\,°\mathrm{C}$ (green bars) equates to an actual substrate temperature of $\vartheta_{\mathrm{substrate}} \approx 200\,°\mathrm{C}$. Respectively, the other substrate temperatures are $\vartheta_{\mathrm{substrate}} \approx 130\,°\mathrm{C}$ for $\vartheta_{\mathrm{set}} = 220\,°\mathrm{C}$ (blue and yellow bars) and $\vartheta_{\mathrm{substrate}} \approx 270\,°\mathrm{C}$ for $\vartheta_{\mathrm{set}} = 380\,°\mathrm{C}$ (red bars). The black bars show the initial lifetimes, measured directly after the deposition without any annealing step. The colored bars show lifetimes measured after annealing steps at $\vartheta_{\mathrm{anneal}} = 220 - 380\,°\mathrm{C}$ on a hotplate in ambient air. Each bar represents the lifetime data of four nominally identical samples. The first three bar plots (blue, green, red bars) represent samples, which were deposited with a hydrogen:silane ratio of 5:1, whereas the bar plot on the right side (yellow bars) represents a deposition with only silane as precursor gas.

The deposition at $\vartheta_{\mathrm{set}} = 300\,°\mathrm{C}$ shows the highest initial effective carrier lifetime of $1000\,\mu\mathrm{s}$ (green bars). The deposition at $\vartheta_{\mathrm{set}} = 380\,°\mathrm{C}$ shows a lower initial lifetime of $850\,\mu\mathrm{s}$ (red bars). We presume that due to the higher deposition temperature less hydrogen is incorporated in the layers and thus the passivation quality suffers. Annealing of these samples further decreases the lifetime. The lowest initial lifetimes of only $100\,\mu\mathrm{s}$ are measured for the depositions at $\vartheta_{\mathrm{set}} = 220\,°\mathrm{C}$ (blue and yellow bars). This relatively poor passivation is not due to a low amount of hydrogen in these layers, but to the structural incorporation of the hydrogen. This can be seen when the samples are annealed. For the deposition represented by the blue bars, the lifetime increases from only $100\,\mu\mathrm{s}$ after the deposition to $700\,\mu\mathrm{s}$, $1000\,\mu\mathrm{s}$ and $1100\,\mu\mathrm{s}$ for annealing temperatures of $\vartheta_{\mathrm{anneal}} = 220\,°\mathrm{C}$, $\vartheta_{\mathrm{anneal}} = 250\,°\mathrm{C}$, and $\vartheta_{\mathrm{anneal}} = 300\,°\mathrm{C}$, respectively. These lifetime values are in the same range as for the deposition at $\vartheta_{\mathrm{set}} = 300\,°\mathrm{C}$. This demonstrates that an effective re-organisation of
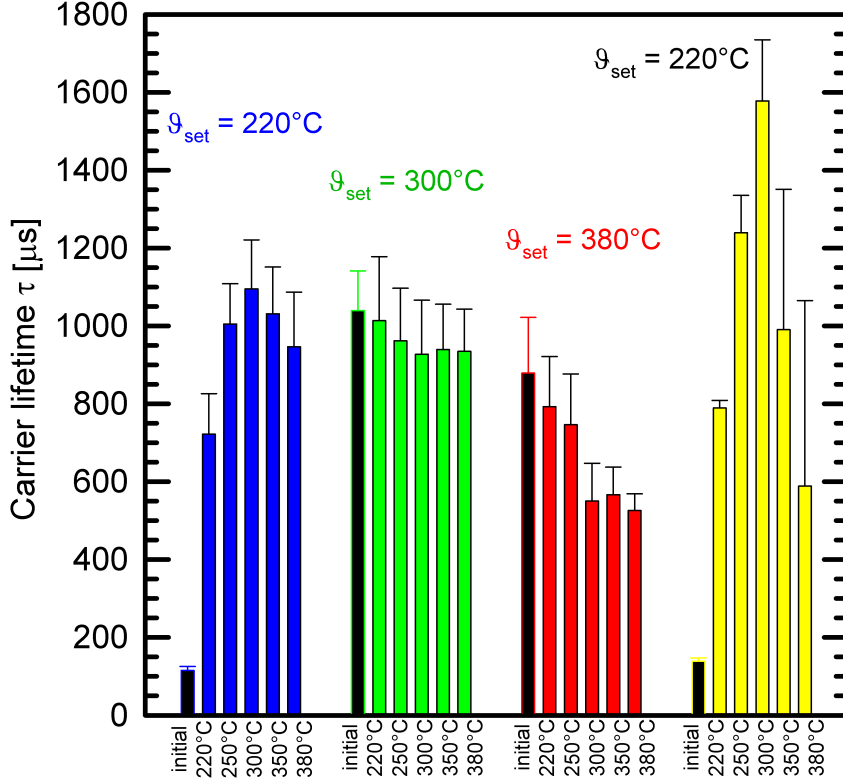
Figure 3.3: Carrier lifetime τ as a function of the set-temperature during the PECVD deposition process and subsequent annealing temperatures. The samples were annealed for 5 minutes on a hotplate for each temperature step. The left 3 groups (blue, green, and red) show data for a deposition with a hydrogen:silane ratio of 5:1. The right group (yellow) shows data for a deposition with only silane as precursor gas.

the hydrogen in the $\vartheta_{set} = 220\,°C$ layer takes place after annealing. A good initial hydrogen contribution is obviously obtained at $\vartheta_{set} = 300\,°C$.

The yellow bars on the right hand side in Fig. 3.3 shows data of a deposition where only SiH_4 was used as precursor gas, i.e. no H_2 was added. The set-temperatur during the deposition was $\vartheta_{set} = 220\,°C$ which corresponds to a substrate temperature of approximately $\vartheta_{substrate} = 130\,°C$. The initial lifetime after the deposition is only $100\,\mu s$. However, subsequent annealing drastically increases the measured effective lifetime. The maximum lifetime of $1600\,\mu s$ is obtained after an annealing step at $\vartheta_{anneal} = 300\,°C$ for 5 minutes.

In Section 1.2.3 it was stated that for a high quality passivation layer enough hydrogen must be present in the PECVD process to cover the entire substrate surface, so that the SiH_3 molecules have a long free path length to reach energetically good positions and in this way form a dense and stable film. Contrariwise, if not enough hydrogen is present at the growing surface, the a-Si:H layer can

grow very fast, incorporating more defects, which decrease the passivation quality of the film. However, the film still contains large amounts of hydrogen that can be activated by thermal annealing. At temperatures around $\vartheta_{\mathrm{anneal}} = 300\,°C$ the hydrogen in the layer is very mobile and can reconfigure inside the a-Si:H network and saturate defect states at the a-Si:H$/c$-Si interface. These results fit well with the observation that the interface passivation quality can be connected with the a-Si:H bulk properties [91].

However, although these deposition parameters lead to the highest effective lifetimes of $1600\,\mu$s after an additional annealing step at $\vartheta_{\mathrm{anneal}} = 300\,°C$, we did not choose the corresponding parameter set as our standard set. In a SHJ solar cell process, the i-a-Si:H passivation layer deposition is followed by the n-type and p-type a-Si:H depositions. In the best case, these depositions should be performed directly after the i-a-Si:H layer deposition without vacuum breakage, or at least with only short times at ambient air between the different depositions. Also, additional handling steps and a possible contamination of the sample should be avoided. An annealing step at $300\,°C$ at the end of the solar cell process or after the deposition of all a-Si:H layers is not possible, because the i/p-a-Si:H layer stack looses its passivation properties at temperatures above $200\,°C$. Consequently, we chose the deposition parameters $\vartheta_{\mathrm{dep}} = 300\,°C$ as our standard parameters. In this case, the initial lifetime is already very high and no additional annealing steps are necessary.

3.2.3 H$_2$-plasma post treatment

The passivation quality of i-a-Si:H films is strongly dependent on the H_2 content and structure in the thin layers (see Sec. 1.2.3). Subsequently to the actual deposition the passivation quality can be improved, by changing the hydrogen bonding structure in the a-Si:H layer by annealing or by a hydrogen plasma treatment [92]. In this Section, the influence of different H_2-plasma post treatments on the passivation quality of our i-a-Si:H layers will be examined.

Experimental

The test samples are $2.5 \times 2.5\,\mathrm{cm}^2$ polished n-type FZ wafers with a resistivity of $3\,\Omega$cm. One set of wafers was random-pyramid-textured in an alkaline KOH/iso-propanole solution. After RCA cleaning, the polished and textured wafers were coated with i-a-Si:H on both sides. Two different i-a-Si:H layer thicknesses, $5\,$nm and $10\,$nm, were deposited on both sets of samples, textured and planar, respectively. These layer thicknesses correspond to a deposition on a planar substrate, therefore the effective layer thickness on the textured samples is reduced by a factor of 1.7. Each set (polished/textured and 5/10 nm) consists of three nominally identical samples. Subsequent to the i-a-Si:H deposition, different H_2-plasma post treatment processes were applied to the samples. An overview of the different H_2-plasma processes is given in Table 3.1. Different plasma powers, electrode distances and

Table 3.1: Overview of the applied H_2 post-plasma treatment conditions.

	$P = 20\,\text{W}$ $d = 50\,\text{mm}$ $t = 180\,\text{s}$	$P = 50\,\text{W}$ $d = 50\,\text{mm}$ $t = 90\,\text{s}$	$P = 100\,\text{W}$ $d = 50\,\text{mm}$ $t = 180\,\text{s}$	$P = 50\,\text{W}$ $d = 30\,\text{mm}$ $t = 90\,\text{s}$	$P = 100\,\text{W}$ $d = 15\,\text{mm}$ $t = 180\,\text{s}$
5 nm *i-a*-Si:H layer	-	-	-	applied	-
10 nm *i-a*-Si:H layer	applied	applied	applied	-	applied

process times were investigated. After the H_2-plasma post treatment the carrier lifetimes of all samples were measured by PCD and an implied open-circuit voltage $V_{\text{OC.impl}}$ was calculated as described in Section 2.2.

Results and discussion

In Fig. 3.4 the calculated $V_{\text{OC.impl}}$ values for the planar and textured samples and for the different *i-a*-Si:H layer thicknesses are shown for the different H_2-plasma conditions. The graph on the left-hand side shows $V_{\text{OC.impl}}$ data for the textured samples and the graph on the right-hand side for the planar surfaces. The red data points in each graph represent samples with a 10 nm *i-a*-Si:H layer, instead the blue data points represent samples with a 5 nm *i-a*-Si:H layer. The open circles in each graph represent the $V_{\text{OC.impl}}$ of samples without any H_2-plasma post treatment process.

The $V_{\text{OC.impl}}$ values for the 10 nm *i-a*-Si:H layers without H_2-plasma reach values of 730 mV for the polished and textured surfaces (red circles). The $V_{\text{OC.impl}}$ values for the 5 nm *i-a*-Si:H layers without H_2-plasma are approximately 710 mV for the planar and only 660 mV for the textured surfaces. Note, that the 5 nm correspond to a deposition on a planar substrate, and thus the effective layer thickness on the textured samples is reduced by a factor of 1.7. Therefore, it can be concluded that the "5 nm" thin *i-a*-Si:H layer is not covering the textured surface in a sufficient way for excellent surface passivation.

For the 10 nm thin *i-a*-Si:H layers we observe a slight but steady decrease of $V_{\text{OC.impl}}$ for increasing the H_2-plasma power. However, the samples investigated in this study have high initial $V_{\text{OC.impl}}$ values compared to those samples which have been proven in the literature to benefit from this kind of treatment[92]. This better starting behavior can be explained by a high and effective hydrogen content in the amorphous network, already directly after the *i-a*-Si:H deposition process.

For the 5 nm *i-a*-Si:H layers a slightly different behavior is observable. The $V_{\text{OC.impl}}$ values of the planar samples stay almost constant, whereas the $V_{\text{OC.impl}}$ of the textured samples increases after the H_2-plasma post treatment. However, as stated before, the effective thickness of the *i-a*-Si:H layers on textured surfaces is reduced by a factor of 1.7 and even less at the pyramid edges, which leads to a reduced passivation. The thermal budget and the additional supply of H_2 may reorganize the amorphous network and in this way increase the passivation. Additionally, it could be much easier for the hydrogen to reach the *a*-Si:H/*c*-Si
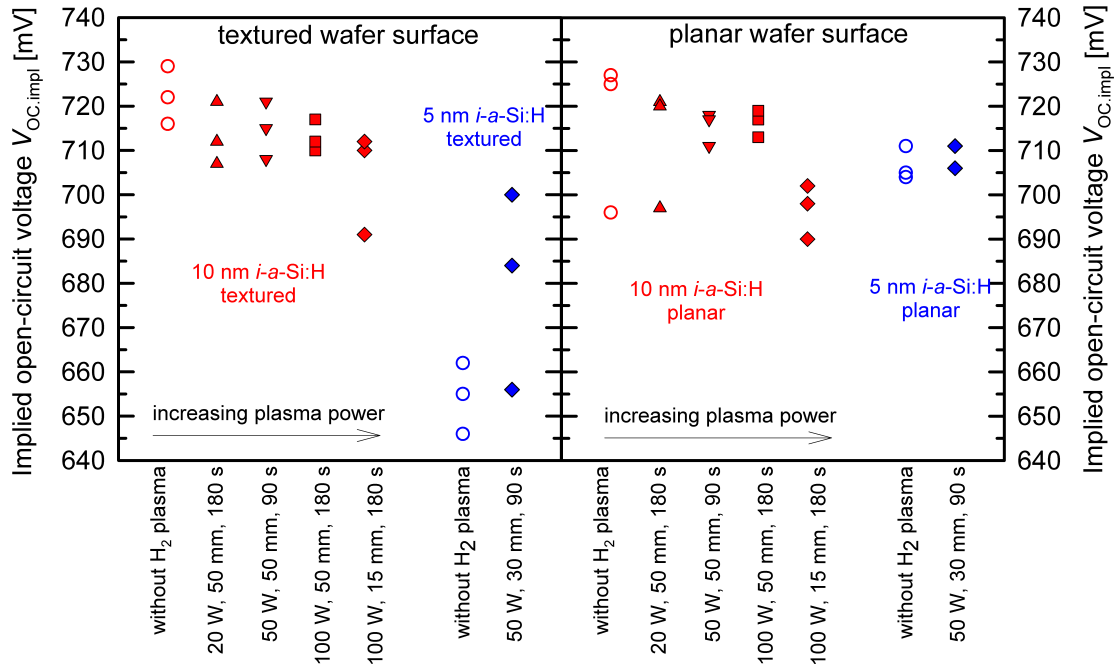
Figure 3.4: Implied open-circuit voltages for samples with and without the H_2-plasma treatment after the actual i-a-Si:H deposition. The different plasma conditions were applied to samples with two different i-a-Si:H layer thicknesses, i.e. 5 nm (blue symbols) and 10 nm (red symbols), on textured (left graph) and planar (right graph) surfaces.

interface and saturate defect states, although it has been proven that hydrogen is also capable of diffusing very deep into the bulk of the amorphous silicon. Also the scattering of the data is very broad for this set of samples and the reached $V_{\text{OC.impl}}$ values after the H_2-plasma post treatment are still not on the highest possible level.

It can be concluded that the passivation quality of our i-a-Si:H layers is already excellent after the actual deposition without any further H_2-plasma post treatment. $V_{\text{OC.impl}}$ values of 730 mV are obtained for 10 nm i-a-Si:H layers on planar and textured surfaces. The high initial passivation quality can be explained by a large hydrogen content in the amorphous network.

3.3 Influence of gas phase doping during *n*-*a*-Si:H and *p*-*a*-Si:H deposition

In this Section, the influence of the gas phase doping during the n-a-Si:H and p-a-Si:H depositions on the layer properties is investigated. First, the conductivity of n-a-Si:H and p-a-Si:H layers will be investigated as a function of the phosphorus and boron flux during the PECVD deposition of the films. Subsequently, the influence of the gas phase doping on solar cell parameters will be examined.

Table 3.2: Process parameters during a-Si:H depositions of conductivity samples. The specified temperature is the set-temperature within the bottom electrode of our PECVD deposition system. The actual sample temperature is expected to be about $100\,°C$ lower.

	Set-temperature [°C]	Deposition pressure [mbar]	Electrode distance [mm]	Power density [mW/cm^2]	SiH$_4$ flow [sccm]	H$_2$ flow [sccm]	PH$_3$ flow [sccm]	B$_2$H$_6$ flow [sccm]
i-a-Si:H	300	0.85	50	35	20	100	-	-
n-a-Si:H	300	0.85	50	35	20	120	4-24	-
p-a-Si:H	220	0.85	50	35	20	96-68	-	4-32

3.3.1 Conductivity measurements of *i*-, *p*- and *n*-*a*-Si:H layers

In this Section, conductivity measurements of intrinsic and doped a-Si:H layers are presented. The measured conductivity of the samples is then related to the Fermi energy level and thus to the effective charge carrier densities in the conduction or valence band.

Experimental

Intrinsic, phosphorus- and boron-doped a-Si:H layers are deposited onto glass substrates. The $2.5 \times 2.5\,cm^2$ boron silicate glass substrates are $1\,mm$ thick and non-conductive. The thickness of the a-Si:H layers is measured after each deposition with a mechanical profilometer (Dektak 150). The deposition time was adjusted in a way that the resulting layer thickness is approximately $300\,nm$ for all samples. The process parameters are shown in Table 3.2. The corresponding process parameters of the n-a-Si:H and p-a-Si:H layers are the same as for the standard i-a-Si layer defined in the previous Section, except the addition of the doping gases PH_3 or B_2H_6, and a lower set-temperature of $220\,°C$ for the p-a-Si:H deposition.[1] Note that only $3\,\%$ of the given amount of PH_3 or B_2H_6 is the dopant gas diluted in $97\,\% H_2$. Consequently, the amount of H_2 is nearly constant for all depositions.

After the a-Si:H deposition, an aluminum finger grid with varying finger spacing is evaporated onto the samples. The finger height and length are $6\,\mu m$ and $20\,mm$, respectively. Fig. 3.5 shows a schematic representation of the test structure. The resistance R between the fingers is then measured using a *Keithley 6517B* electrometer, which is capable of measuring currents in the $10^{-15}\,A$ region. The measurements of the doped layers are performed at a controlled temperature of $25\,°C$ under vacuum conditions. Instead, the conductivity measurements of the i-a-Si:H layers were performed at elevated temperatures and then extrapolated to the value at room temperature, because the conductivity is too low to be measured directly. For statistical reasons, the resistance R is measured for 3 different finger spacings.

---

[1]It is common that the boron-doped p-a-Si:H layer is deposited at low temperatures around $130\,°C$, because the hydrogen effusion is strongly increased in these layers at higher temperatures [93].
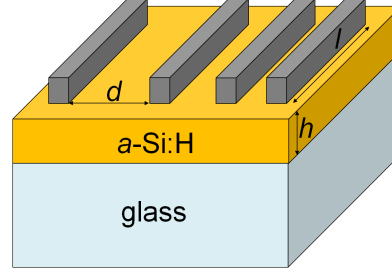
Figure 3.5: Schematic representation of the test structure to measure the *a*-Si:H conductivity. Note that the thickness in the picture is not in scale ($h_{\text{glass}} = 1$ mm, $h_{a\text{-Si:H}} = 300$ nm, $h_{\text{finger}} = 5~\mu$m).

Conductivity results

The conductivity σ of the *a*-Si:H layers can be calculated from:

$$\sigma = \frac{1}{\rho} = \frac{d}{R \cdot l \cdot h}. \tag{3.1}$$

Here, ρ is the resistivity, R the measured resistance, d the distance between the fingers, and $l \cdot h$ is the cross-section area of the *a*-Si:H layer as indicated in Fig. 3.5.

The conductivity σ as a function of the gas phase doping (GPD) is shown in Fig. 3.6. The GPD is calculated by the quotient of the dopant gas and the sum of all process gas-flows:

$$GPD = \frac{[PH_3]}{[PH_3] + [H_2] + [SiH_4]} \quad \text{for } n\text{-type } a\text{-Si:H} \tag{3.2}$$

and

$$GPD = \frac{[B_2H_6]}{[B_2H_6] + [H_2] + [SiH_4]} \quad \text{for } p\text{-type } a\text{-Si:H}. \tag{3.3}$$

Each data point represents the mean value of the measurements at different finger spacings. The *n*-*a*-Si:H layers are shown as red triangles and the *p*-*a*-Si:H layers are shown as green squares and circles. The two *p*-*a*-Si:H depositions were performed with identical process parameters during the PECVD process, but at two different runs with varying metalization. However, the two data sets are nearly identical, which underlines the reliability of our measurement results. The dashed lines are guides to the eye. The *i*-*a*-Si:H layers are shown as blue symbols.

For the *i*-*a*-Si:H layers conductivities of 1-6×10^{-11} S/cm are measured. These values correspond well with literature data for high quality *i*-*a*-Si:H [94]. By adding PH_3 (red triangles) or B_2H_6 (green squares) to the PECVD process, the conductivity increases drastically. By further increasing the GPD, the conductivity of the *a*-Si:H layers slightly continues to increase to a maximum value. For the *n*-*a*-Si:H layers conductivities of 5×10^{-3} S/cm are measured at a GPD of 1800-
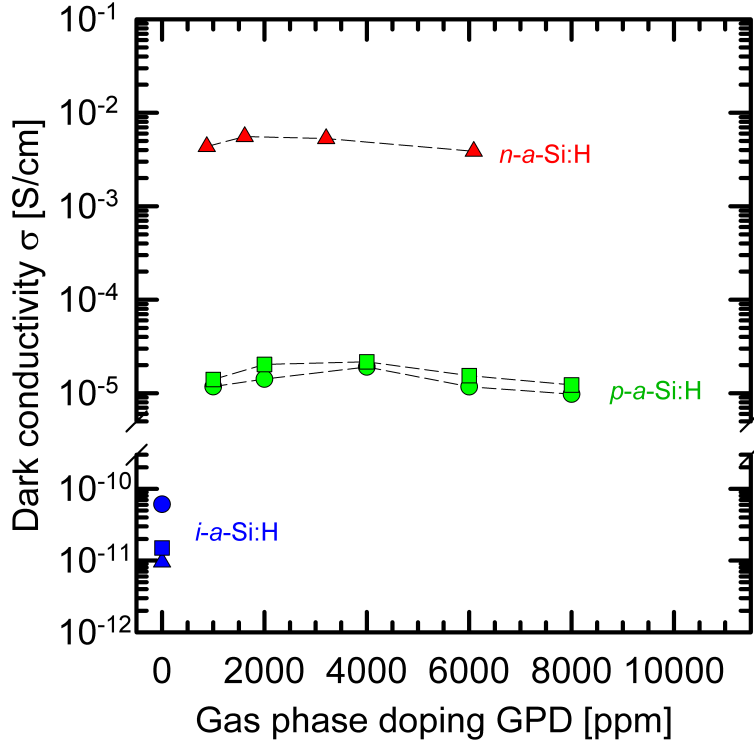
Figure 3.6: Dark conductivity σ of i-a-Si:H (blue data points), n-a-Si:H (red data points), and p-a-Si:H (green data points) layers as a function of the gas phase doping during the PECVD process. While the different colors indicate the doping type, the different symbols belong to varying process parameters. Note the break in the ordinate.

3000 ppm. For the p-a-Si:H layers conductivities of 2×10^{-5} S/cm are measured at a GPD of 2000-4000 ppm. Further increasing the GPD leads to a decrease of the conductivities, which is due to an increased defect formation in the mobility gap, which "pulls" the Fermi level away from the band edges, as discussed in Section 1.2.5.

Effective doping

The measured conductivity σ can be converted into charge carrier densities in the conduction and valence band with the following equation:

$$\sigma = \sigma_n + \sigma_p = n \, \mu_n \, q + p \, \mu_p \, q \,. \tag{3.4}$$

However, the mobilities of electrons μ_n and holes μ_p must be known. These can e.g. be determined by Hall measurements. However, because the exact mobilities of our a-Si:H layers are not known, we chose typical literature values for the electron mobility of $\mu_n = 10 - 40 \, \text{cm}^2/\text{Vs}$ and hole mobility of $\mu_n = 5 - 20 \, \text{cm}^2/\text{Vs}$ [95, 96].
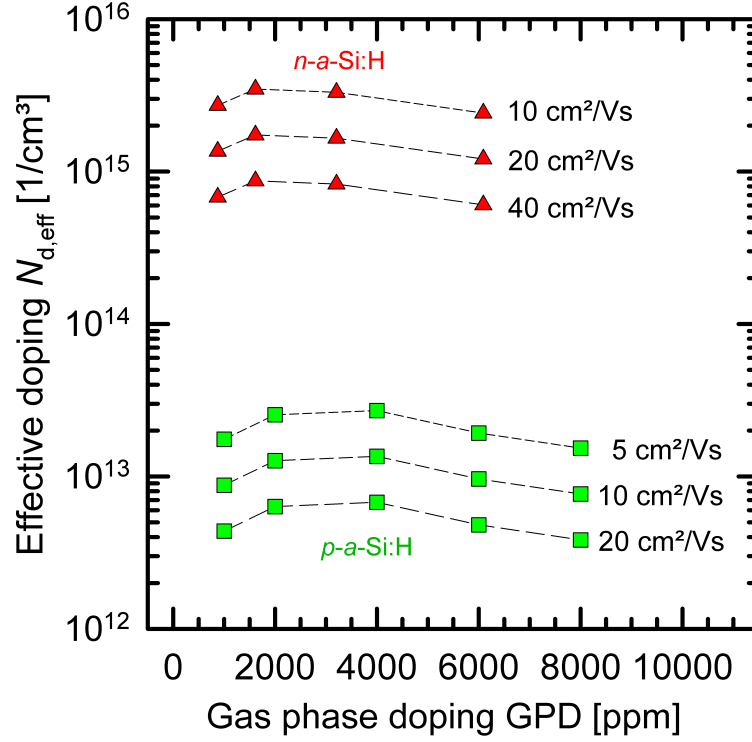
Figure 3.7: Effective doping $N_{\mathrm{d,eff}}$ of different *a*-Si:H layers as a function of the gas phase doping GPD for different electron and hole mobilities. The red data points belong to *n*-*a*-Si:H samples and the green data points to *p*-*a*-Si:H samples.

In the case of a *n*-*a*-Si:H the conductivity is dominated by the electrons in the conduction band. The calculated electron density can be interpreted as an effective doping concentration $N_{\mathrm{d,effective}}$, which can be much smaller than the amount of phosphorus atoms in the *n*-*a*-Si:H layer. Fig. 3.7 shows the calculated effective doping for the *n*-*a*-Si:H and *p*-*a*-Si:H samples for different values of electron and hole mobilities.

Fermi-level position

The Fermi-level position in the *a*-Si:H band gap can be calculated from:

$$E_{\mathrm{C}} - E_{\mathrm{F}} = -k\,T \cdot ln\left(\frac{n}{N_{\mathrm{C}}}\right) \quad \text{and} \quad E_{\mathrm{F}} - E_{\mathrm{V}} = -k\,T \cdot ln\left(\frac{p}{N_{\mathrm{V}}}\right) \tag{3.5}$$

for *n*-*a*-Si:H and *p*-*a*-Si:H, respectively. Here, E_{C} is the conduction band edge, E_{V} is the valence band edge, E_{F} is the Fermi energy, N_{C} and N_{V} are the effective densities of states in the conduction and valence band, respectively, k is the Boltzmann factor, and n and p are the electron and hole densities. Fig. 3.8 shows the Fermi-levels for the *n*-*a*-Si:H and *p*-*a*-Si:H samples calculated assuming electron and hole mobilities
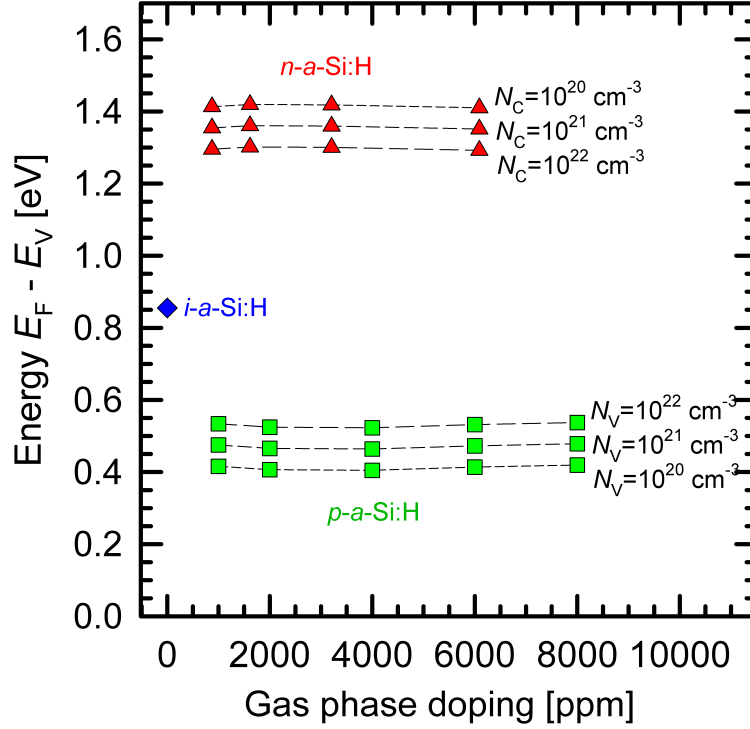
Figure 3.8: Fermi-level position $E_F - E_V$ in the a-Si:H band gap as a function of the gas phase doping GPD for different effective densities of states. The blue diamond represents data for the i-a-Si:H sample, which was calculated assuming an effective density of states of $10^{21}\,\mathrm{cm}^{-3}$.

of $\mu_\mathrm{n} = 20\,\mathrm{cm^2/Vs}$ and $\mu_\mathrm{p} = 10\,\mathrm{cm^2/Vs}$, respectively, and typical values of the effective densities of states N_C and N_V [37]. The distance of the Fermi-level from the conduction band edge for the n-a-Si:H layers is calculated to be $0.3\,\mathrm{eV}$ assuming a mobility gap of $1.7\,\mathrm{eV}$ and an effective density of states of $N_\mathrm{C} = 10^{21}\,\mathrm{cm}^{-3}$. The distance of the Fermi level from the valence band for the p-a-Si:H layers is calculated to be $0.45\,\mathrm{eV}$ assuming a mobility gap of $1.7\,\mathrm{eV}$ and an effective density of states of $N_\mathrm{V} = 10^{21}\,\mathrm{cm}^{-3}$. These values correspond well with typical values reported in the literature [37, 19]. However, the calculated Fermi-levels are about $0.15\,\mathrm{eV}$ further away from the conduction and valence band as the theoretical minima (Section 1.2.5).

In the intrinsic case $n = p = n_\mathrm{i}$, Eq. 3.4 can be rewritten as:

$$n_\mathrm{i} = \frac{\sigma}{q \cdot (\mu_\mathrm{n} + \mu_\mathrm{p})}\,. \tag{3.6}$$

Inserting the measured conductivity of $\sigma = 1\times10^{-11}\,\mathrm{S/cm}$ leads to an intrinsic carrier density of $2.4\times10^{6}\,\mathrm{cm}^{-3}$. Assuming an electron mobility of $\mu_\mathrm{n} = 20\,\mathrm{cm^2/Vs}$,

Table 3.3: Process parameters for solar cell test structures with various doped *n-a*-Si:H and *p-a*-Si:H layers. The specified temperature is the set-temperature within the bottom electrode of our deposition system. The sample temperature is expected to be about $100\,^\circ$C lower.

	Set-temperature [°C]	Deposition pressure [mbar]	Electrode distance [mm]	Power density [mW/cm^2]	SiH$_4$ flow [sccm]	H$_2$ flow [sccm]	PH$_3$ flow [sccm]	B$_2$H$_6$ flow [sccm]
i-a-Si:H	300	0.85	50	35	20	100	-	-
n-a-Si:H	300	0.85	50	35	20	96-76	4-24	-
p-a-Si:H	160	0.85	50	35	20	92-68	-	8-32

a hole mobility of $\mu_{\mathrm{p}} = 10\,\mathrm{cm}^2/\mathrm{Vs}$, and an effective density of states of $N_{\mathrm{c}} = N_{\mathrm{v}} = 10^{21}\,\mathrm{cm}^{-3}$, the obtained Fermi-level is at $E_{\mathrm{F}} - E_{\mathrm{V}} = 0.86\,\mathrm{eV}$. This value is very close to the middle of the *a*-Si:H mobility gap, as expected for an intrinsic semiconductor.

3.3.2 Influence of gas phase doping on solar cell performance

In this Section, the influence of the gas phase doping GPD on the open-circuit voltages V_{OC} and pseudo fill factors pFF of solar cell precursor structures is investigated. Two sets of samples were fabricated: one set with varying PH_3 dilution during the *n-a*-Si:H deposition and another set with varying B_2H_3 dilution during the *p-a*-Si:H deposition, while all other process parameters were kept constant. The finished samples were then measured by the *Suns-V*$_{\mathrm{OC}}$ method and the V_{OC} and pFF values were extracted.

Experimental details

We use $2.5 \times 2.5\,\mathrm{cm}^2$ polished *n*-type FZ wafers with a resistivity of $3\,\Omega$cm. After RCA cleaning, all wafers were deposited with a $5\,\mathrm{nm}$ *i-a*-Si:H passivation layer on both sides. For the *i-a*-Si:H deposition the parameters found in Section 3.2 where used. Subsequently, *n-a*-Si:H was deposited onto the rear side and then *p-a*-Si:H onto the front side. On a first set of the samples, the PH_3 flux during the *n-a*-Si:H depositions was varied, while the B_2H_3 flux during the *p-a*-Si:H depositions was kept constant. On a second set of samples, the PH_3 flux during the *n-a*-Si:H depositions was kept constant, while the B_2H_3 flux during the *p-a*-Si:H depositions was varied. The deposition parameters for all layers are given in Table 3.3.

For set 1, the PH_3 flux was varied in a way that the total process gas flux was kept constant at $120\,\mathrm{sccm}$, i.e. $20\,\mathrm{sccm}$ SiH_4, $x\,\mathrm{sccm}$ PH_3, and $(100\text{-}x)\,\mathrm{sccm}$ H_2. Because the actual PH_3 amount is only $3\,\%$ diluted in $97\,\%$ H_2, also the total H_2 amount is nearly constant in each deposition. These gas fluxes result in GPD of 1000-6000 ppm. For set 1, a constant B_2H_3 flux of $8\,\mathrm{sccm}$ was applied, which corresponds to a GPD of 2000 ppm.
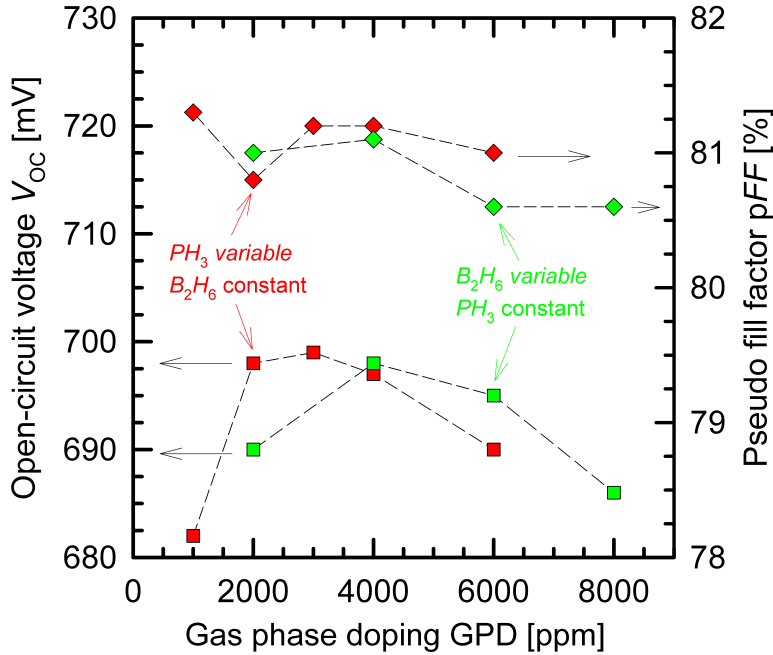
Figure 3.9: Open-circuit voltage V_{OC} (squares) and pseudo fill factor pFF (diamonds) for gas phase doping GPD variations of n-a-Si:H (red data points) and p-a-Si:H (green data points) layers. The lines are guides to the eye.

For set 2, the PH_3 flux was kept constant at 24 sccm, which represents a GPD of 6000 ppm, whereas the B_2H_3 flux was varied between 8-32 sccm, which corresponds to a GPD of 2000-8000 ppm. After the a-Si:H deposition, a TCO was sputtered onto both sides of the samples. In this case we used sputtered ZnO:Al.

Results and discussions

The finished samples were measured using the *Suns-V$_{OC}$* method. Fig. 3.9 shows the obtained open-circuit voltages V_{OC} (squares) and pseudo fill factors pFF (diamonds) as a function of the GPD. The red data points represent the n-a-Si:H and the green data points represent the p-a-Si:H variations. The dashed lines are guides to the eye. The data points representing the n-a-Si:H doping variation show a V_{OC} maximum for a GPD of 3000 ppm (red squares). The data points representing the n-a-Si:H doping variation show a V_{OC} maximum for a GPD of 4000 ppm (red squares). These data correspond well with the results from the conductivity measurements of the previous Section 3.3.1. The highest conductivity for the n-a-Si:H layer was obtained at a GPD of 1800-3000 ppm. Instead, for the p-a-Si:H layer the highest conductivity was measured for a GPD of 4000 ppm.

The higher the conductivity of the a-Si:H layers, and thus the nearer the Fermi-level is to the conduction or valence band edge, the higher is the band bending in the

c-Si substrate, which leads to a better surface passivation (field effect passivation) by efficient screening of one type of charge carrier from the recombination-active interface. The trend of the pseudo fill factor p*FF* is not so distinct. It seems to follow the V_{OC}-trend except the data point that represents the $GPD = 1000$ ppm deposition. However, the deviation of the p*FF* is very small and therefore these values lie more or less in the margin of error.

Resulting from this experiment, the *n*-*a*-Si:H layer with a GPD of 3000 ppm and the *p*-*a*-Si:H layer with a GPD of 4000 ppm are the best layers concerning optimum V_{OC}. Therefore, these layers are used for the fabrication of our SHJ solar cells. It has to be noted, that also the choice of the TCO has a detrimental impact on the recombination properties and thus influences the V_{OC} [25]. In later experiments we do not use ZnO:Al as TCO, but ITO instead. Our current solar cells with the layer doping evaluated in this experiment and presented in Section 5.3 reach in fact V_{OC} values of 730 mV.

3.4 Impact of the H$_2$ dilution on the solar cell performance

The passivation quality of thin *i*-*a*-Si:H films depends critically on the hydrogen-to-silane ratio during the PECVD deposition process [97]. High hydrogen dilutions promote the formation of crystallites even on amorphous substrates such as glass. On *c*-Si wafers, high hydrogen-to-silane ratios can lead to (defective) epitaxial growth and thus poor surface passivation quality [67, 70]. Such adverse epitaxial growth also depends on the crystal orientation of the *c*-Si wafer substrate, as first presented by Das et al. for polished (1 0 0) and (1 1 1) surfaces [68, 98]. Therefore, here we examine the effect of the hydrogen-to-silane ratio with respect to the crystal orientation of the *c*-Si wafer substrate. We choose plasma conditions that do not produce any Raman-detectable crystalline signal for 300 nm thick films on glass, even for very high hydrogen-to-silane ratios.

3.4.1 Experimental

For the *a*-Si:H depositions we use a *CS 400 P* PECVD cluster system of *von Ardenne*. For the intrinsic and doped *a*-Si:H depositions we use a 13.65 MHz parallel plate PECVD reactor respectively with a diameter of 27 cm. The deposition parameters for the intrinsic and doped *a*-Si:H layers are given in Table 3.4. Plasma power, electrode distance and set-temperature are the result of the lifetime optimization presented in Section 3.2. The power density of $35\,\mathrm{mW/cm^2}$ used in this study is similar to that applied in other studies [98]. The specified temperature refers to the set-temperature within the bottom electrode of the deposition system. Our actual samples lie on an aluminum carrier positioned on top of this bottom electrode. Thus, the thermal contact between the 300 °C bottom electrode and our samples is relatively weak. The actual sample temperature is therefore considerably lower than

Table 3.4: Process parameters during *a*-Si:H depositions. Plasma power, electrode distance and set temperature are the result of an optimization of the passivation properties of 10 nm thick intrinsic *a*-Si:H films on Si wafer substrates. The specified temperature is the set-temperature within the bottom electrode of our deposition system. The sample temperature is expected to be about 100 °C lower.

	Set-temperature [°C]	Deposition pressure [mbar]	Electrode distance [mm]	Power density [mW/cm^2]	SiH$_4$ flow [sccm]	H$_2$ flow [sccm]	PH$_3$ flow [sccm]	B$_2$H$_6$ flow [sccm]
i-*a*-Si:H	300	0.85	50	35	2-60	118-60	-	-
n-*a*-Si:H	300	0.85	50	35	20	88	12	-
p-*a*-Si:H	220	0.85	50	35	20	84	-	16

the set temperature and is expected to be at approximately 200 °C as commonly found in literature for well-passivating *a*-Si:H layers [51, 99].

We fabricate solar cells on four different wafer surfaces. We use (i) polished and (ii) damage etched 3 Ωcm *n*-type float zone (FZ) wafers with (1 0 0) crystal orientation, (iii) textured 3 Ωcm *n*-type FZ wafers where the (1 0 0) surface changes to pyramids with (1 1 1)-oriented facets and (iv) chemically polished 70 Ωcm *n*-type FZ wafers with (1 1 1) crystal orientation.

Prior to each *i*-*a*-Si:H deposition the wafers are RCA-cleaned, followed by a 1 % HF dip, subsequently rinsed in de-ionized (DI) water for 1 minute and dried with dry nitrogen. We then deposit 5 nm *i*-*a*-Si:H on each side of the wafers with the parameters given in Table 3.4. The silane concentration (SC) was varied from 4.2 % to 33.3 % and is given by SC = [SiH$_4$] / ([SiH$_4$] + [H$_2$]).

Prior to the following *n*-*a*-Si:H and *p*-*a*-Si:H depositions the wafers are dipped in 1 % HF for 1 minute plus subsequent rinsing in DI water and drying in nitrogen. After the *a*-Si:H depositions we perform photoconductance decay (PCD) measurements and calculate implied open-circuit voltages ($V_{\text{OC,implied}}$) from the lifetime data [87, 100]. ITO is then sputtered onto both sides of the samples and the $V_{\text{OC,implied}}$ is measured again. After that we evaporate an aluminum grid onto both sides and measured the *J-V* curves of the 4 cm^2 cells directly after evaporating the aluminum and after an annealing step for 5 minutes at 175 °C on a hotplate in ambient air. The *J-V* curves are measured using a LOANA system [85].

3.4.2 Results and discussion

The $V_{\text{OC,implied}}$ data obtained from the lifetime measurements and the V_{OC} data from the *J-V* curves of our SHJ solar cells are shown in Figure 3.10. Figure 3.10 shows the V_{OC} data for the four different surfaces of the samples as a function of the silane concentration. We measure high $V_{\text{OC,implied}}$ values after the *a*-Si:H deposition for all types of surfaces (red symbols). However, we observe different characteristic trends for the (1 0 0) and the (1 1 1) surfaces. For the samples with (1 0 0) surfaces (upper two graphs) we observe a strong decrease of V_{OC} with
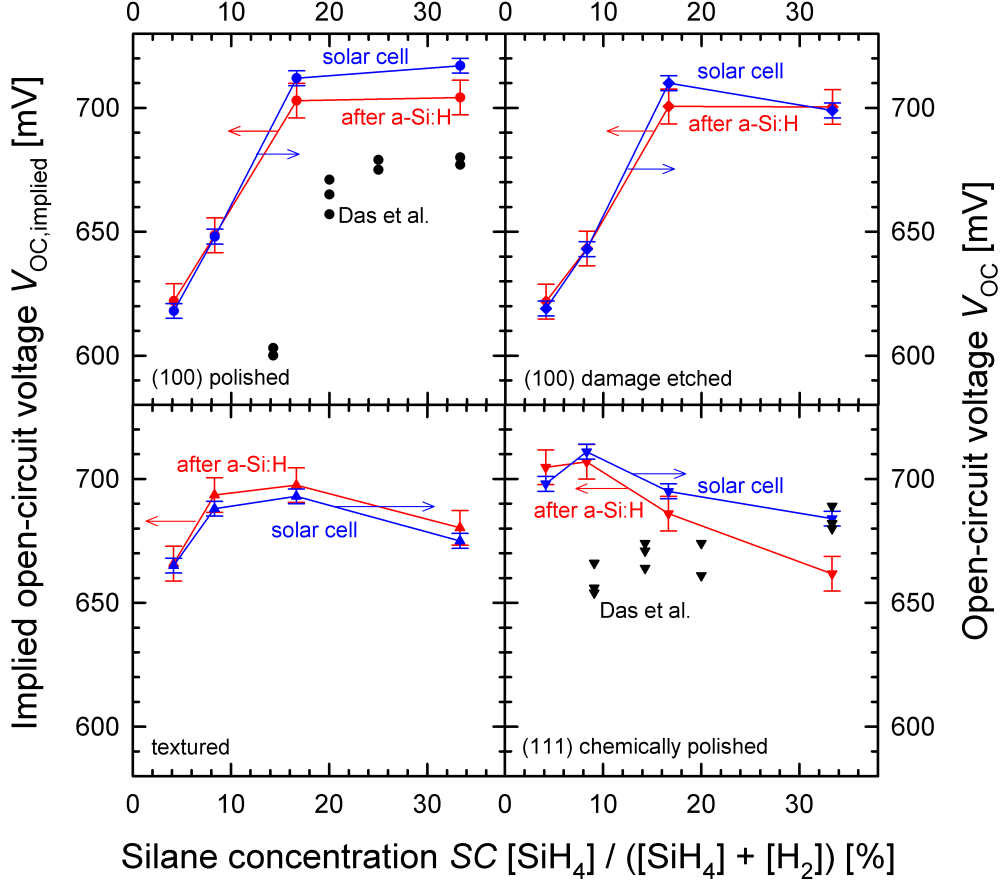
Figure 3.10: V_{OC} data for four different crystal orientations of the sample surfaces plotted as a function of the silane concentration. The $V_{OC,implied}$ data obtained from the lifetime measurements are shown as red symbols and the V_{OC} data from the *J-V* curves of our SHJ solar cells are shown as blue symbols. The red and blue lines are guides to the eye only. The black data points are V_{OC} data reported by Das et al. [68, 98].

decreasing SC for SC < 16 %, whereas the cells with (1 1 1) surfaces (lower two graphs) show still high V_{OC} values at lower SC. We find a broad maximum of V_{OC} for the samples with (1 0 0) surfaces up to high silane concentrations, whereas the samples with (1 1 1) surfaces have their V_{OC} maximum at SC = 8 % for the chemically polished (1 1 1) surfaces. The textured samples reach their highest voltages at SC = 16 % and show a decrease of V_{OC} for higher silane concentrations. After ITO sputtering and Al-evaporation we anneal the solar cells for 5 minutes at 175°C (blue data points in Figure 3.10). We observe that the V_{OC} values reach again the level of the implied $V_{OC,implied}$ from the lifetime measurements prior to ITO sputtering.

Compared to the V_{OC} values from Das et al. [68, 98] (black symbols in Figure 3.10) we achieve higher V_{OC} values for (1 0 0)- and for (1 1 1)-oriented surfaces.
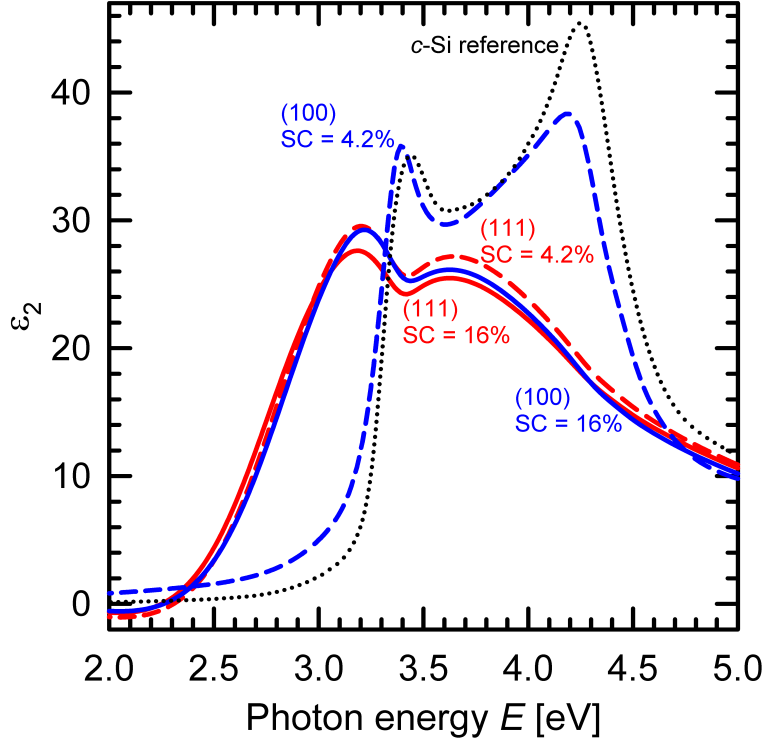
Figure 3.11: Imaginary part of the pseudodielectric function for the polished (1 0 0) and (1 1 1) wafers after the *i*-*a*-Si:H depositions for silane concentrations of 4.2 % and 16 %. The (1 0 0) sample deposited with a SC of 4.2 % shows the signature of crystalline silicon, whereas the other samples do not.

We also observe a different trend of the V_{OC} values for the (1 1 1) surfaces. While the V_{OC} values from Das et al. decrease with higher hydrogen dilution we find an optimum of the V_{OC} values at higher hydrogen dilution, i.e. SC = 8 %. This different behavior might be associated with the different cleaning procedures and the lower pressure applied in the experiment of Das et al. [68, 98].

Similarly to Das et al. we observe that for (1 0 0)-oriented Si wafers very high hydrogen dilutions eventually lead to a decreased surface passivation quality. Our reference Si-films on glass exhibit no Raman-detectable crystalline signal, however, it is well known that (1 0 0) orientations facilitate silicon epitaxy [51, 101]. Ross et al. [102] described how a crystalline substrate promotes the formation of crystalline growth in PECVD.

We therefore performed ellipsometry measurements using a *Woollam M*-2000 spectral ellipsometer. We examine the polished (1 0 0) and (1 1 1) wafers after the *i*-*a*-Si:H depositions with silane concentrations of 4.2 % and 16 %, respectively. The imaginary part of the pseudodielectric function $\epsilon_1 + i\epsilon_2$ is shown in Figure 3.11. The (1 0 0) sample with the film deposited at a low silane concentration (SC = 4.2 %)
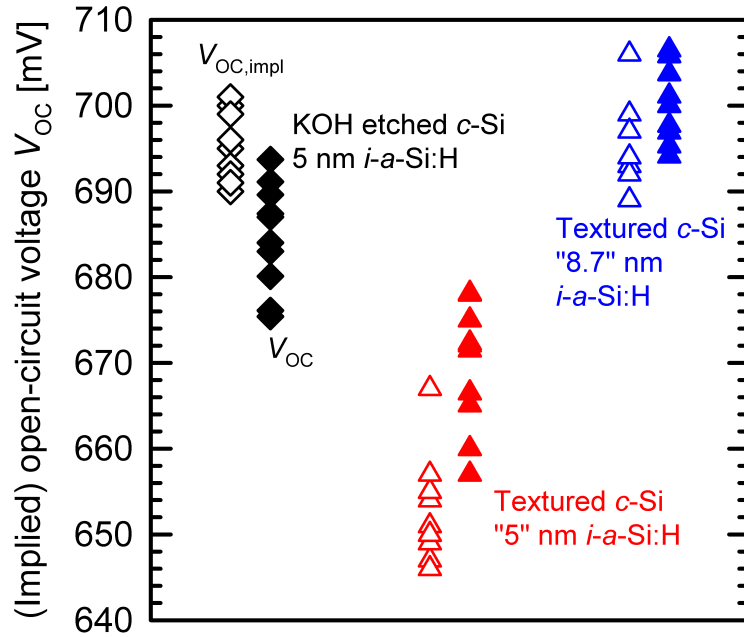
Figure 3.12: V_{OC} data for different i-a-Si:H layer thicknesses for planar KOH etched and for textured surfaces. The open symbols show $V_{OC,implied}$ data after i-a-Si deposition. The filled symbols show V_{OC} data of the finished solar cells. The black and red data points show V_{OC} data for a deposition time that produces a 5 nm i-a-Si:H layer on planar surfaces. The blue data points show V_{OC} data for a deposition time that produces a 8.7 nm i-a-Si:H layer on planar surfaces. On textured surfaces a 1.7 times thicker i-a-Si:H layer is necessary to reach the same V_{OC} values than on planar surfaces due to the increased surface area.

clearly shows a crystalline signature. This is a distinct difference to the a-Si:H film deposited at a high silane concentration (SC = 16 %) on the (1 0 0) substrate, and also different to both types of film depositions (i.e. SC =16 % and SC = 4.2 %) on the (1 1 1) wafers. Thus, measured effective carrier lifetime data correlates well with the structural properties of the deposited films. We therefore attribute the decay in the passivation quality on (1 0 0)-oriented wafers with increasing hydrogen dilution to the formation of defective epitaxial growth.

In our experiment we observe that the absolute V_{OC} values for the textured surfaces are lower than for the planar surfaces. It is well known that the surface passivation quality depends on the thickness of the i-a-Si:H layer. In particular, it has been shown by Olibet [103] that textured surfaces lead to a reduced layer thickness by a factor of 1.7 in comparison to planar surfaces due to the enlarged surface area and the tilted surface normal.

In order to test the influence of the local layer thickness on the surface passivation of our textured samples, we perform the following experiment: We choose the deposition regime with SC = 16 % and prepare a-Si passivation and solar cells on
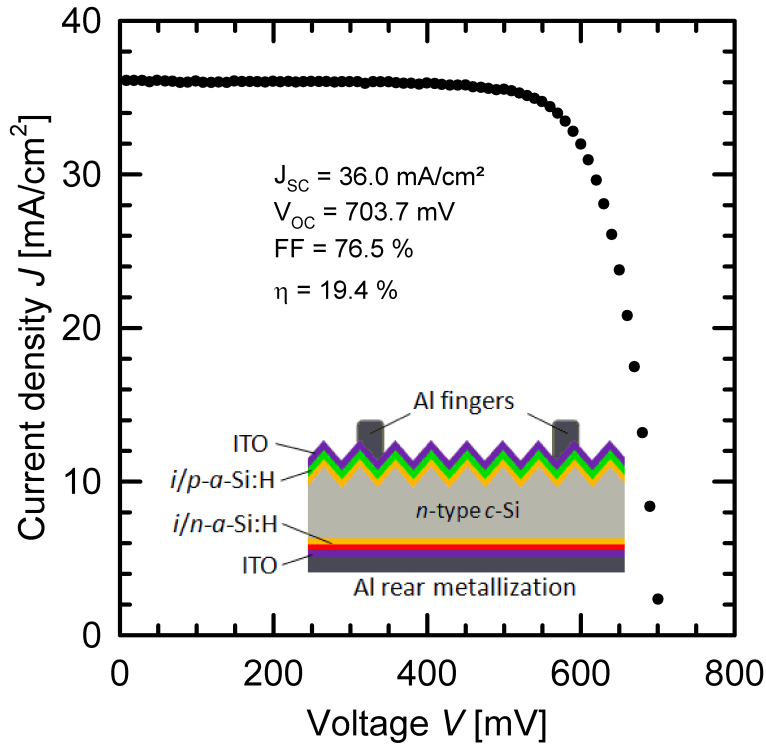
Figure 3.13: *J-V* curve and extracted cell parameters of a $2 \times 2\,\text{cm}^2$ heterojunction solar cell on a textured wafer with a deposition time that produces a $8.7\,\text{nm}$ *i-a*-Si:H layer on planar surfaces.

planar and textured wafers with two different *i-a*-Si:H layer deposition durations. Figure 3.12 shows V_{OC} data of textured and planar wafers coated in the same deposition process that leads to $5\,\text{nm}$ thick *i-a*-Si:H layers on planar surfaces. Also shown in Figure 3.12 are results for textured samples where the *i-a*-Si:H layer deposition process was extended by a factor of 1.7 ("8.7 nm" deposition). The implied open-circuit voltages, as calculated from carrier lifetime data, were measured directly after the *i-a*-Si:H deposition and the V_{OC} data are taken from light *J-V* measurements of the finished solar cells. In accordance with our open-circuit voltage data in Figure 3.10 we observe lower V_{OC} values for the textured samples. However, the textured cells with the prolonged *i-a*-Si:H layer deposition time ("8.7 nm" deposition) achieve the same range of V_{OC} values as the cells with $5\,\text{nm}$ *i-a*-Si:H layer on planar surfaces. Figure 3.13 shows the *J-V* curve of the best solar cell from this batch that reaches a high V_{OC} of $703.7\,\text{mV}$ and a resulting cell efficiency of 19.4%.

3.4.3 Conclusions

We find that the *a*-Si:H surface passivation of (1 0 0)-oriented samples deteriorates with increasing hydrogen concentration in the PECVD process. This can be attributed to the onset of crystalline silicon growth in the deposited films. However, we find that increasing the hydrogen dilution of silane in PECVD is beneficial for the passivation of (1 1 1)-oriented surfaces, whilst the opposite holds true for (1 0 0)-oriented substrates. We find very good agreement between the implied open-circuit voltages ($V_{\mathrm{OC,implied}}$) obtained from the lifetime measurements after the *a*-Si:H depositions and the final silicon heterojunction solar cell open-circuit voltages (V_{OC}) after annealing. The $V_{\mathrm{OC,implied}}$ measurements are therefore well suited for process monitoring during heterojunction solar cell processing. Depending on the silane-to-hydrogen ratio and the crystal orientation of the silicon wafer surfaces we have achieved excellent surface passivation after a final annealing step of the solar cell. After annealing we achieve V_{OC} values $> 710\,\mathrm{mV}$ and energy conversion efficiencies in excess of $19\,\%$.

3.5 Plasma Profiling Time-of-Flight Mass Spectroscopy (PP-TOFMS) measurements of doped *a*-Si:H layers

We investigate our *n*-*a*-Si:H BSF and *p*-*a*-Si:H emitter layers with Plasma Profiling Time-of-Flight Mass Spectroscopy (PP-TOFSM)[2] to obtain information about the composition of the layers. The main focus is on the concentrations of phosphorus and boron atoms as well as on the question if any oxygen is present at the *a*-Si:H/*c*-Si interface.

Measurement technique

Plasma Profiling Time-of-Flight Mass Spectroscopy (PP-TOFMS) combines a plasma source with a time-of-flight mass analyzer. An argon plasma provides both, the sputtering of the sample surface, and ionization of the sputtered neutrals that are then transferred to a time-of-flight mass spectrometer. In this way, variations of ion signals are detected in dependence of the sputter time. By continuous sputtering, a complete mass spectrum at any depth of the sample can be obtained by time-to-depth conversion and a Relative Sensitivity Factor (RSF) calibration of the signals from the detected elements.

Experimental

For the fabrication of the test samples 4 inch polished *n*-type FZ wafers with a resistivity of $3\,\Omega\mathrm{cm}$ are used. The wafers are RCA-cleaned, followed by a $1\,\%$ HF dip, subsequently rinsed in de-ionized (DI) water for 1 minute and dried with dry

---

[2]The PP-TOFMS measurements were performed at Horiba Jobin Yvon, Palaiseau, France.

Table 3.5: Process parameters of *a*-Si:H depositions for PP-TOFMS measurements. The specified temperature is the set-temperature within the bottom electrode of our deposition system. The sample temperature is expected to be about $100\,°C$ lower.

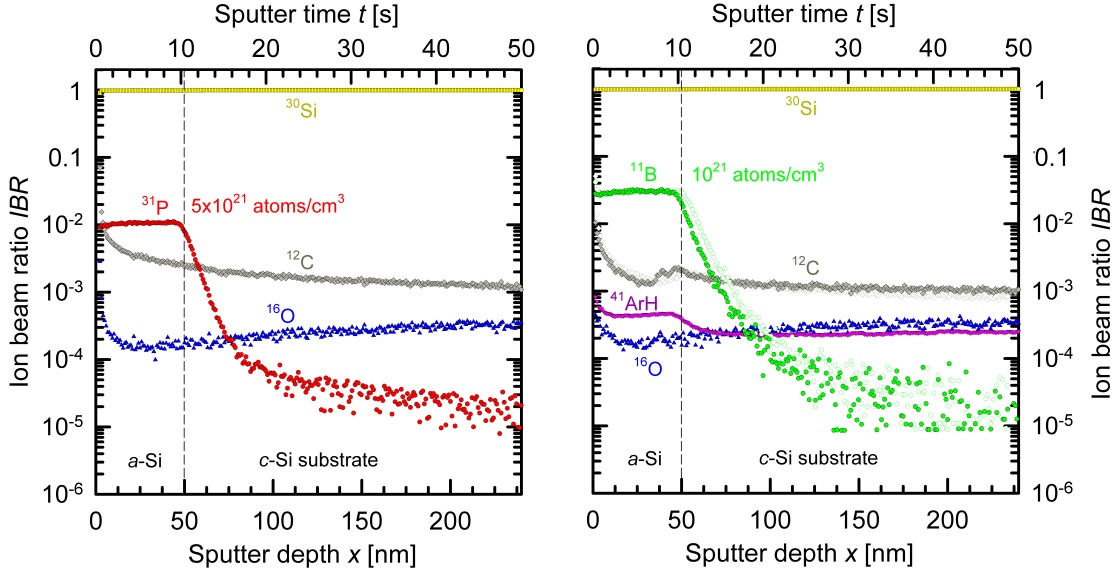|	Set-temperature [°C]	Deposition pressure [mbar]	Electrode distance [mm]	Power density [mW/cm^2]	SiH$_4$ flow [sccm]	H$_2$ flow [sccm]	PH$_3$ flow [sccm]	B$_2$H$_6$ flow [sccm]
n-*a*-Si:H	300	0.85	50	35	20	88	12	-
p-*a*-Si:H	160	0.85	50	35	20	84	-	16

Figure 3.14: Ion beam ratio *IBR* as a function of the sputter depth for a phosphorus doped (left graph) and a boron doped (right graph) sample.

nitrogen. On a first set of wafers we deposit $50\,nm$ *n*-*a*-Si:H onto one side with the parameters given in Table 3.5. On a second set we deposit $50\,nm$ *p*-*a*-Si:H. Before the PP-TOFMS measurements no special preliminary preparation is necessary.

Results and discussion

Figure 3.14 shows the PP-TOFMS measurements. The ion beam ratio (*IBR*) is plotted as a function of the sputter time or depth. The graph on the left-hand side shows the data for the *n*-*a*-Si:H sample and the graph on the right-hand side for the *p*-*a*-Si:H sample. The dominant signal for both samples stem from ^{30}Si. In crystalline Si, the atom density is approximately $5 \times 10^{22}\,cm^{-3}$. However, in *a*-Si:H the Si atom density is lower in the range of 65-95 % compared to *c*-Si [104]. For *a*-Si:H with a hydrogen amount of 20 % a density of approximately 80 % can

be assumed. This correlates to a Si atom density of approximately $4 \times 10^{22}\,\mathrm{cm^{-3}}$. The boron concentration has been calculated from its IBR_B-value and relative sensitivity factor (RSF) that has been calculated from calibration measurement of boron-doped silicon wafers. In this way, a boron concentration of $1 \times 10^{21}\,\mathrm{cm^{-3}}$ was found for our p-a-Si:H layers. That concentration is considerably higher than the effective doping calculated in Section 3.3.1. However, in Section 1.2.5 was stated that only a small amount ($< 10^{-4}$) of the incorporated dopant atoms are active. This effect is even stronger for the boron-doped p-a-Si:H layers than for the phosphorus doped n-a-Si:H layers. The boron and phosphorus signal is constant over the first 50 nm, which equates to the a-Si:H layer thickness. However, at a depth of 50 nm the signal does not decrease abruptly rather than decay constantly over the next 20-30 nm. This effect can be attributed to a certain sample surface roughness.

Oxygen and carbon can only be measured qualitatively. However, two results can be concluded from the data. At the front of the n-a-Si:H sample, $x = 0\,\mathrm{nm}$, a peak is observable for the oxygen and the carbon signals. The oxygen signal may stem from a thin $\mathrm{SiO_x}$ layer at the front or adsorbed oxygen-carbon molecules. The carbon signal additionally may stem from contaminations on the sample surface. Except the peak at the sample surface, the oxygen and carbon signals are almost constant over depth and continuous at the a-Si:H/c-Si interface, which indicates that this signal is a background noise of the measurement.

For the p-a-Si:H sample we observe the same behavior except a small carbon peak at the a-Si:H/c-Si interface. For reliability reasons the sample was measured again at a different location (filled and open symbols) and again shows the small peak in the carbon signal. This peak may stem from insufficient sample cleaning before the p-a-Si:H deposition. Therefore, it can be concluded that excellent wafer cleaning and careful handling of the wafers prior to the a-Si:H depositions is crucial to avoid contaminations.

4

Optical properties and ray-tracing simulations

In this Chapter the optical properties of our a-Si:H and ITO layers are investigated. First, ellipsometric measurements are presented to determine the refractive index n, the extinction coefficient k, and the optical band gap E_{opt}. Based on the obtained values, ray tracing simulations are performed to determine the optical losses due to the a-Si:H and ITO layers of our SHJ solar cells. The simulation results will finally be compared with experimental data.

4.1 Ellipsometric measurements

4.1.1 Measurement technique

We apply variable-angle spectroscopic ellipsometry to determine the refractive index n, the extinction coefficient k and the optical band gap E_{opt} of our a-Si:H and ITO layers. However, these parameters cannot be measured directly, since ellipsometry determines only the polarization change in a beam of reflected or transmitted polarized light, quantified by the amplitude ratio $\tan \Psi$ and the phase difference Δ. Therefore, a model for the complex refractive index characteristics is needed, including the wavelength of the incident light, the angle of incidence, Ψ and Δ, which is then fitted to the measurement data.

For the ellipsometric measurements in this study, a J.A. Woollam Co., Inc. spectroscopic ellipsometer is used. For the data fitting the *WVASE32* software and the *Levenberg-Marquardt* multivariate regression algorithm is used [105]. For the measurements three different angles, 50°, 60°and 70°, and a wavelength spectrum ranging from 240 to 1700 nm is used. Additionally, transmission measurements are performed to obtain additional data for the fitting routine. In order to model the a-Si:H layers, we employ the *Tauc-Lorentz* approach [106], which is widely used for modeling the optical properties of amorphous materials. Additionally, we used the *Cody-Lorentz* approach [107], which in difference to the *Tauc-Lorentz* approach also includes a term that accounts for the absorption in the Urbach tails. However,

we find that for the fitting of our data the Urbach absorption term does not lead to any relevant differences.

4.1.2 Measurement results

For the ellipsometric measurements 15 nm thin a-Si:H layers were deposited onto a 100 nm silicon oxide grown on a polished silicon wafer. The c-Si substrate and the SiO$_2$ are described by standard literature data taken from Palik [108]. Additionally, the a-Si:H layers were deposited onto glass for transmission measurements. The ITO layers with a thickness of 100 nm were deposited on glass.

Fig. 4.1 shows the refractive index n and extinction coefficient k for different anti-reflection coatings and a-Si:H layers. The left graph shows n and k values for two different ITO layers and a SiN$_\text{x}$ anti-reflection coating. The blue triangles represent the ITO used in this work. The green squares represent data of an ITO with a charge carrier density of 2×10^{20} cm^{-3} taken from Holman et al. [109]. The red circles represent data of a typical SiN$_\text{x}$ anti-reflection layer taken from Nagel [110]. The SiN$_\text{x}$ layer has the best optical properties as anti-reflection coating on a silicon solar cell. The extinction coefficient is close to zero, and the refractive index is close to 2 over a broad wavelength range. Our ITO layer (blue triangles) shows a significant absorption in the short wavelength regime due to band-to-band absorption. However, also for higher wavelengths the absorption is not negligible due to free carrier absorption. Additionally, the refractive index decreases strongly for higher wavelengths, which results in a poorer amplitude matching. The right graph shows n and k values for different a-Si:H layers. The i-, n-, and p-a-Si:H layers used in this study are shown as blue, red, and green triangles, respectively. For comparison, the dotted lines represent data of thin a-Si:H layers taken from Holman et al. [22].

When fitting the model to the measured data, the optical bandgap of the a-Si:H layer can be set as a free fitting parameter. In this way, it is possible to extract the optical bandgaps from the fitted experimental data. For our i-a-Si:H layer we find $E_\text{gap} = 1.70 \pm 0.04$ eV, for the p-a-Si:H layer we find $E_\text{gap} = 1.72 \pm 0.03$ eV, and for the n-a-Si:H layer we find $E_\text{gap} = 1.70 \pm 0.03$ eV.

4.2 Ray-tracing simulations

4.2.1 Simulation geometry and parameters

For the optical simulations the ray-tracing program *Sunrays* was used [111]. A schematic representation of the simulated geometry is shown in Fig. 4.2. The simulation was performed for a unit cell, which is defined by its base area of $10 \times 10\,\mu\text{m}^2$ and a height of $180\,\mu$m. On top of this structure one single pyramid is located with a height of $7\,\mu$m, which results from the crystal orientation of the c-Si substrate and the base area. The optical parameters for the c-Si bulk are taken from
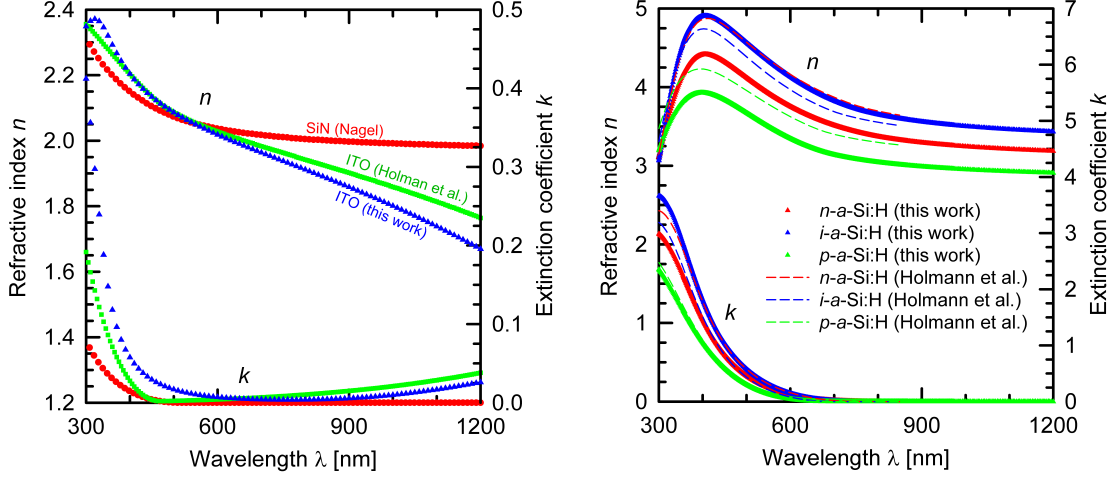
Figure 4.1: The left graph shows the refractive index n and the extinction coefficient k for different anti-reflection coatings. The blue triangles show the ITO used in this work. The green squares show data of an ITO with a charge carrier density of 2×10^{20} cm^{-3} taken from Holman et al. [109]. The red circles show data of a typical SiN$_x$ anti-reflection layer taken from Nagel [110]. The right graph shows n and k values for different a-Si:H layers. The i-, n-, and p-a-Si:H layers used in this study are shown as blue, red, and green triangles, respectively. For comparison, the dotted lines represent data taken from Holman et al. [22].

Green [112]. On the back side a layer stack is present consisting of i-a-Si:H, n-a-Si:H, ITO, and Al metalization. On the front side a layer stack is present consisting of i-a-Si:H, p-a-Si:H, and ITO. The simulation was performed for different i-a-Si:H and p-a-Si:H layer thicknesses. Because our SHJ solar cells have a metal grid on the rear side, i.e. only a fraction of the rear side is metalized, simulations with and without a metal rear reflector were performed. The optical input parameters (n, k) for the a-Si:H and ITO layers were taken from the ellipsometric measurements in 4.1.2. On the rear side 60 % Lambertian reflection was assumed.

4.2.2 Comparison of simulated and experimental results

The ray-tracing simulation was performed for different sets of parameters, which are shown in Table 4.1. The lower half of Table 4.1 shows the input parameters for the simulations. The simulation number 1 represents the standard SHJ solar cell. Layer thickness variations compared to the standard cell are marked as bold numbers. The asterisk marks layers, where the absorption is set at zero ($k = 0$). All simulations are performed without front grid shading. The absorption in the i-a-Si:H layers is assumed to be fully parasitic. The thicknesses given for the front side layers correspond to an axis vertical to the pyramid surface, i.e. on a planar substrate the thicknesses would be increased by a factor of 1.7.

The upper half of Table 4.1 shows the simulation results for the different simulations. The results are the absorbed light in the c-Si bulk (J_{SC}), the surface
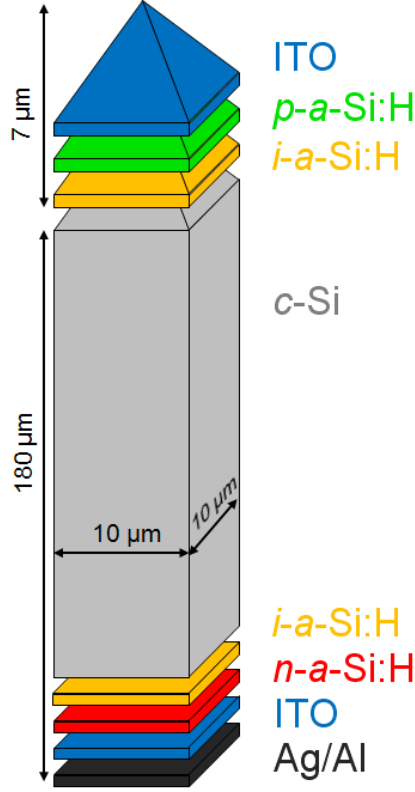
Figure 4.2: Schematic representation of a unit cell of the simulated structure.

Table 4.1: The upper half of the table shows simulation results for different parameters of the studied SHJ solar cells. The lower half of the table shows the input parameters for the simulation according to Fig. 4.2. The simulation #1 represents the standard SHJ solar cell. All layer thickness variations compared to the standard cell are marked as bold numbers. The asterisk marks layers, where the absorption is set to zero ($k = 0$). The absorption in the a-Si:H layers is assumed as fully parasitic. The simulation results have an absolute error of ± 0.01.

| Simulation #	1	2	3	4	5	6	7	8	9	10	11
Absorbed (J_{SC}) [mA/cm^2]	38.5	38.74	39.35	39.54	39.29	41.69	41.78	38.89	37.84	38.25	38.68
Surface reflection [mA/cm^2]	1.22	1.24	1.22	1.19	1.34	1.17	1.18	1.23	1.24	1.16	1.3
Escape reflection [mA/cm^2]	1.46	1.53	1.44	1.44	1.59	1.57	1.75	1.44	1.45	1.45	1.45
Transmitted [mA/cm^2]	0.92	0.15	0.94	0.92	1.04	1.05	1.22	0.93	0.92	0.93	0.92
Parasitic absorption [mA/cm^2]	3.83	4.28	2.99	2.85	2.67	0.45	0.00	3.45	4.48	4.14	3.58
Front ITO thickness [nm]	58	58	58	58	**58***	**58***	**58***	58	58	58	58
Front p-a-Si:H thickness [nm]	8.7	8.7	**8.7***	8.7	8.7	**8.7***	**8.7***	8.7	8.7	**12**	**6**
Front i-a-Si:H thickness [nm]	5	5	5	**5***	5	**5***	**5***	3	**8.7**	5	5
Rear i-a-Si:H thickness [nm]	3	3	3	3	3	3	**3***	3	3	3	3
Rear n-a-Si:H thickness [nm]	15	15	15	15	15	15	**15***	15	15	15	15
Rear ITO thickness [nm]	100	100	100	100	100	100	**100***	100	100	100	100
Rear metallization [μm]	0	**5**	0	0	0	0	0	0	0	0	0
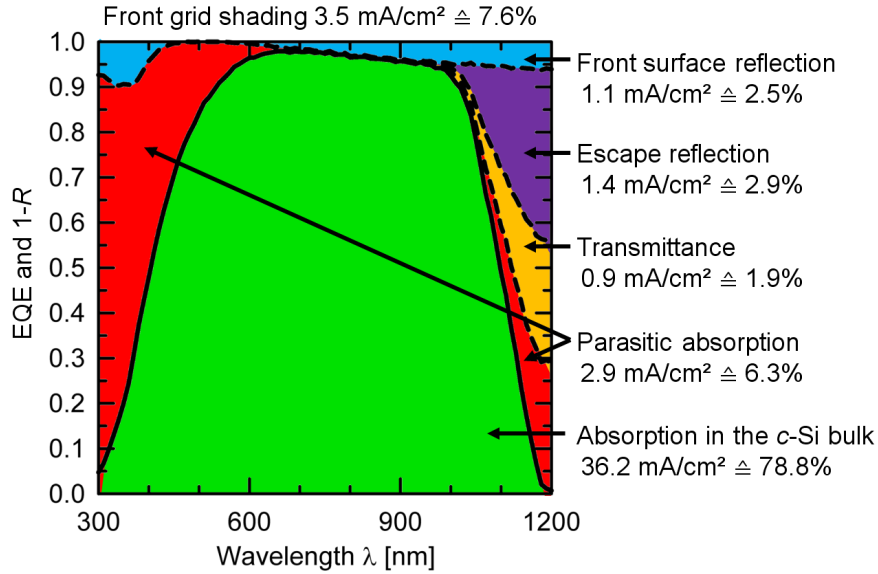
Figure 4.3: Simulated EQE and 1-R data for one of our standard SHJ solar cells (simulation #1 in Table 4.1). The green area represents the absorption in the c-Si bulk and thus the J_{SC}. The red area represents the parasitic absorption in the front and rear a-Si:H and ITO layers. The orange area represents the transmittance, and the blue and violet areas the reflection losses.

reflection, the escape reflection, the transmitted light, and the parasitic absorption in the a-Si:H and ITO layers, expressed as current densities. All the different simulations and their results will be described in detail in the following paragraphs.

Fig. 4.3 exemplarily shows the simulated EQE and 1-R results for the standard parameters of our SHJ solar cells. The corresponding parameters are given by simulation #1 in Table 4.1. Most of our SHJ solar cells are bifacial, i.e. they have a metalization grid on the front and rear side. Whereas simulation #1 was performed without metal on the rear side, simulation #2 represents a simulation where on the rear side a $5\,\mu$m Ag layer is present. A current gain of $0.77\,\mathrm{mA/cm^2}$ is obtained, due to the decreased transmittance on the rear side. However, not all of this better transmittance is translated to a J_{SC} gain which is only $0.24\,\mathrm{mA/cm^2}$. A high amount of the not transmitted (but reflected) light from the rear side is absorbed in the a-Si:H and TCO layers. However, only $7\,\%$ of the rear side of our bifacial solar cells is actually covered with metal.

Simulations #3, #4, and #5 represent cases where the absorption of one of the front layers is set at zero ($k = 0$). By comparing the parasitic absorption losses from these simulations with simulation #1 the absorption in the ITO, p-a-Si:H, and i-a-Si:H layers are $1.16\,\mathrm{mA/cm^2}$, $0.84\,\mathrm{mA/cm^2}$, and $0.98\,\mathrm{mA/cm^2}$, respectively. Since there is no other possibility in the simulation program, the absorption in the i-a-Si:H layer is assumed to be fully parasitic. However, it is known that only about $50\,\%$ of the absorption in the i-a-Si:H layer is parasitic and therefore half of the generated

charge carriers can contribute to J_{SC}. On the contrary, nearly all absorption in the p-a-Si:H layer is parasitic [22]. Assuming that only the half of the generated charge carriers recombine again before they can be collected leads to a value of $0.49\,\text{mA/cm}^2$ for the parasitic absorption in the i-a-Si:H layer. When adding this value to the simulated J_{SC} of the standard cell (simulation #1), and considering a front grid shading of $7.6\,\%$, a J_{SC} of $36.29\,\text{mA/cm}^2$ is obtained. This simulated value fits very well with the experimental value of $J_{\text{SC}} = 36.30\,\text{mA/cm}^2$ from our $10 \times 10\,\text{cm}^2$ SHJ solar cells that will be presented in Section 5.3.2.

In simulation #6 the absorption of all front layers is set at zero ($k = 0$). The simulated parasitic absorption stemming from the layer stack on the rear side is $0.45\,\text{mA/cm}^2$. The absorption on the rear side is much smaller than on the front side, because only light with high wavelengths reaches the rear. In simulation #7 the absorption of all front and rear layers is set at zero ($k = 0$). As expected, the parasitic absorption is equal to zero.

However, the sum of all determined parasitic absorption losses (front p-a-Si:H + front i-a-Si:H + front ITO + rear layer stack) is only $J_{\text{par}} = 3.43\,\text{mA/cm}^2$ and not, as given by simulation #1, $J_{\text{par}} = 3.83\,\text{mA/cm}^2$. The reason is that when only the absorption of one layer is set at zero, the other layers absorb more. Therefore, the values for the absorption in the different layers obtained from subtracting the absorption current from simulations #3, #4 and #5 from simulation #1 are only a lower limit for the absorption in the corresponding layer.

Simulations #8 − #11 represent thickness variations of either the front p-a-Si:H or i-a-Si:H layer. Fig. 4.4 shows the J_{SC} plotted as a function of the layer thicknesses. For the i-a-Si:H layers a parasitic absorption of $50\,\%$ was assumed. The simulated data for the p-a-Si:H layers is represented as green diamonds. The simulated data for the i-a-Si:H layers is represented as blue diamonds. From the slope of the trend line the absorption losses in terms of current per nm layer thickness can be calculated. For the p-a-Si:H layers a current loss of $0.8\,\text{mA/cm}^2\cdot\text{nm}$ was determined. For the i-a-Si:H layers a current loss of $0.9\,\text{mA/cm}^2\cdot\text{nm}$ was determined. For comparison, experimental results for p-a-Si:H (green triangles) and i-a-Si:H (blue triangles) are added to the graph. The absolute values for the experimentally obtained data are much lower, because of the front grid shading, which is not considered in the simulations. Importantly, the determined current losses per nm layer thickness are very close to the simulated values. Hence, we can conclude that our optical ray-tracing simulations agree very well with the solar cell results.
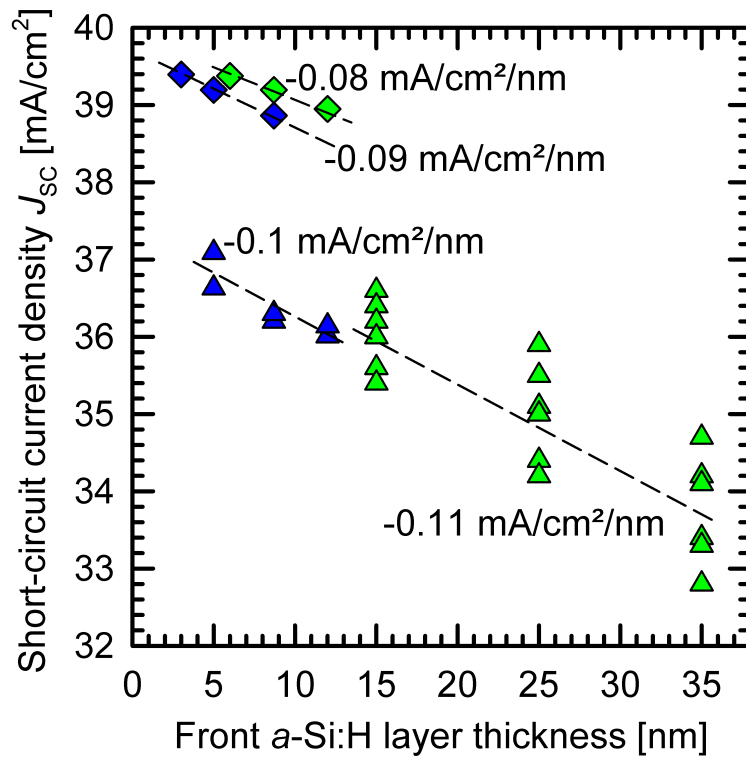
Figure 4.4: Simulated (diamonds) and measured (triangles) J_{SC} values for p-a-Si:H (green) and i-a-Si:H (blue) layers. From the slope of the different data sets the current density loss per nm layer thickness is calculated. The dotted lines are guides to the eye.

<div style="text-align: right;">**5**</div>

Analysis of series resistance and shading losses

In this Chapter, we introduce a novel experimental method to quantify the series resistance $R_{a\text{-Si/ITO}}$ through the a-Si:H layers and the a-Si:H/ITO interface on test structures. In order to optimize $R_{a\text{-Si/ITO}}$, we apply different a-Si:H and ITO deposition parameters. We find the best value for $R_{p\text{-}a\text{-Si/ITO}}$ of $0.42\,\Omega\,\text{cm}^2$ for an ITO double layer with a 10 nm thin starting layer that provides good contact resistance and an additional 90 nm top layer that provides good conductivity. For $R_{n\text{-}a\text{-Si/ITO}}$ we reach values below $0.1\,\Omega\,\text{cm}^2$. We present an analysis of the series resistance and shading losses of our $10 \times 10\,\text{cm}^2$ bifacial screen-printed a-Si:H/c-Si heterojunction solar cells, which show an open-circuit voltage of $V_{\text{OC}} = 733\,\text{mV}$, demonstrating the excellent level of interface passivation. The efficiency of $20.2\,\%$ is limited by a relatively low short-circuit current density of $37.1\,\text{mA/cm}^2$ and fill factors of $76\,\%$.

5.1 Introduction

The concept of both-side contacted a-Si:H/c-Si heterojunction solar cells provides high conversion efficiencies of up to $24.7\,\%$ ($V_{\text{OC}} = 750\,\text{mV}$, $J_{\text{SC}} = 39.5\,\text{mA/cm}^2$, $FF = 83.2\,\%$) [17, 18, 113]. Very high open-circuit voltages V_{OC} can be achieved by excellent surface passivation properties of the thin hydrogenated amorphous silicon (a-Si:H) films [114]. However, the i/p-a-Si:H front emitter limits the short-circuit current density J_{SC} due to absorption losses in the amorphous silicon layers [22] and also the fill factor FF due to resistive losses caused by charge carrier transport through the a-Si:H layers and the a-Si:H/TCO interface [21]. In this Chapter, we present for the first time an experimental method to quantify the series resistance losses through the a-Si:H layers and the a-Si:H/TCO interface on test structures. In order to minimize the a-Si:H/TCO contact resistance, we apply different a-Si:H and ITO deposition parameters on our test structures.
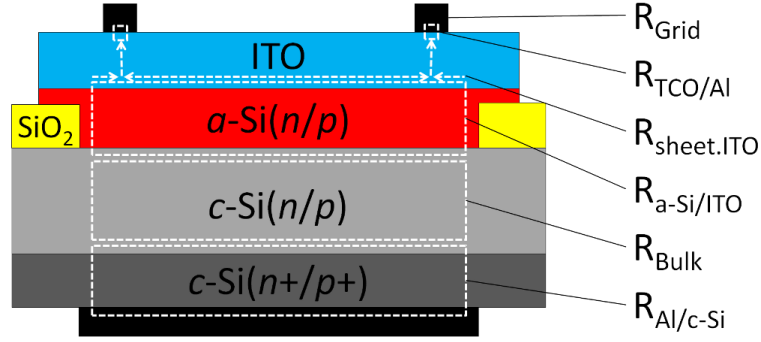
Figure 5.1: Schematic cross section of the test structure to determine the resistance through the *a*-Si:H layers plus *a*-Si:H/ITO interface.

Another major impact on J_{SC} and *FF* stems from the front electrode, i.e. the front TCO and the metallization grid. Absorption losses in the front TCO and shading of the front grid decrease the short-circuit current. The fill factor is strongly influenced by the front grid design depending on the sheet resistance of the TCO (resistance between the metal fingers), the resistivity of the front grid metal and the contact resistance between metallization and TCO.

We present here an analysis of the series resistance and shading losses of our bifacial screen-printed $10 \times 10\,\text{cm}^2$ *a*-Si:H/*c*-Si heterojunction solar cells. Of special interest in our analysis are the resistive losses due to the carrier transport through the *a*-Si:H layers and the *a*-Si:H/TCO interface. We quantify all individual series resistance contributions by characterization on separate test structures.

5.2 Resistance losses through the *a*-Si:H layer and *a*-Si:H/ITO interface

5.2.1 Experimental details

Fig. 5.1 shows a schematic cross section of our test structure to determine the resistance of the current through the *a*-Si:H layers and the *a*-Si:H/ITO interface. We use shiny etched 6 inch $1.5\,\Omega\,\text{cm}$ *p*-type and polished 4 inch $3\,\Omega\,\text{cm}$ *n*-type float zone silicon wafers. After RCA cleaning, a thermal oxide was grown onto the wafer surfaces and subsequently removed on the rear side of the wafers using HF. The remaining oxide on the front side provides a diffusion barrier in the following boron diffusion of the *p*-type wafers and phosphorus diffusion of the *n*-type wafers. After the diffusions the PSG and BSG were etched of in HF and all wafers were laser-cut into $25 \times 25\,\text{mm}^2$ samples. Using an inkjet we print a structured hotmelt etching mask onto the front side of the samples and define a $20 \times 20\,\text{mm}^2$ oxide window by etching off the oxide in the middle of the wafers using HF. The hotmelt was then removed by isopropanol and all wafers were RCA-cleaned. Prior to the following

n-*a*-Si:H and *p*-*a*-Si:H depositions all wafers were dipped in a 1 % HF solution, rinsed in deionized water for 1 minute and dried using dry nitrogen. For the *a*-Si:H depositions we use a *CS 400P* cluster system (von Ardenne, Germany) with a 13.65 MHz parallel-plate PECVD reactor. Prior to the following ITO depositions all wafers were HF-dipped again in a 1 % HF solution, rinsed in deionized water and dried with dry nitrogen. The ITO layer was sputtered through a $21 \times 21 \, \text{mm}^2$ shadow mask to avoid shunts at the edges of the samples. After the ITO depositions we evaporate $7 \, \mu\text{m}$ aluminum onto the full rear side of our test structures. We then evaporate a $21 \, \mu\text{m}$ thick aluminum finger grid onto the front side of our samples. The finger grid allows *J-V* measurements of the samples in the dark as well as under illumination. After the aluminum evaporation we anneal the samples on a hotplate for 5 minutes at 150 °C.

5.2.2 Results and discussions

In order to optimize the *a*-Si:H/ITO contact resistance, we use two different hydrogen-to-silane ratios for the *n*-*a*-Si:H and *p*-*a*-Si:H depositions, respectively: a higher hydrogen-to-silane ratio of 11:1 and a lower hydrogen-to-silane ratio of 5:1. It is known that the hydrogen-to-silane ratio in the PECVD process strongly influences the properties of the *a*-Si:H layers [69, 115, 116]. High hydrogen dilutions promote crystalline growth in the PECVD process. Also the band gap and the work function are influenced by the hydrogen dilution. In the following we refer to the samples with the lower hydrogen-to-silane ratio with *a*-Si:H^{low} and to the samples with the higher hydrogen-to-silane ratio with *a*-Si:H^{high}.

For the optimization of the *a*-Si:H/ITO contact resistance we also use different sputter conditions for the ITO depositions. We vary the plasma power, deposition pressure, deposition temperature and the oxygen dilution $O_2/(O_2 + Ar)$ in the reactive sputter process. Fig. 5.2 shows the ITO resistivity as a function of the O_2 dilution for different ITO sputter powers and temperatures. We find the lowest resistivity values of $\rho = 0.5 \times 10^{-3} \, \Omega \, \text{cm}$ for O_2 dilutions between 0.3 % and 0.6 % which corresponds well with other literature data [117, 118]. Also, with increasing sputter power the resistivity decreases. The heated samples (red diamonds) show a slightly lower resistivity than the samples sputtered at room temperature (black squares). The data points shown as green circles belong to samples sputtered with low power and low O_2 dilution. Because of the higher resistivity values around $\rho = 1.5 \times 10^{-3} \, \Omega \, \text{cm}$, leading to a high sheet resistance, these ITO layers are not suitable as front TCO in heterojunction solar cells. However, the lower power in the sputter process is more gentle and causes less damage to the *a*-Si:H layers due to a reduced ion bombardment. Additionally, we found that low-power, low-oxygen ITO layers provide a low contact resistance to the doped *a*-Si:H layers. The low contact resistance in spite of a higher resistivity is most likely due to the different sputter conditions influencing the barrier formation rather than a bulk effect. However, a reactive sputter process without any O_2 is very unstable and
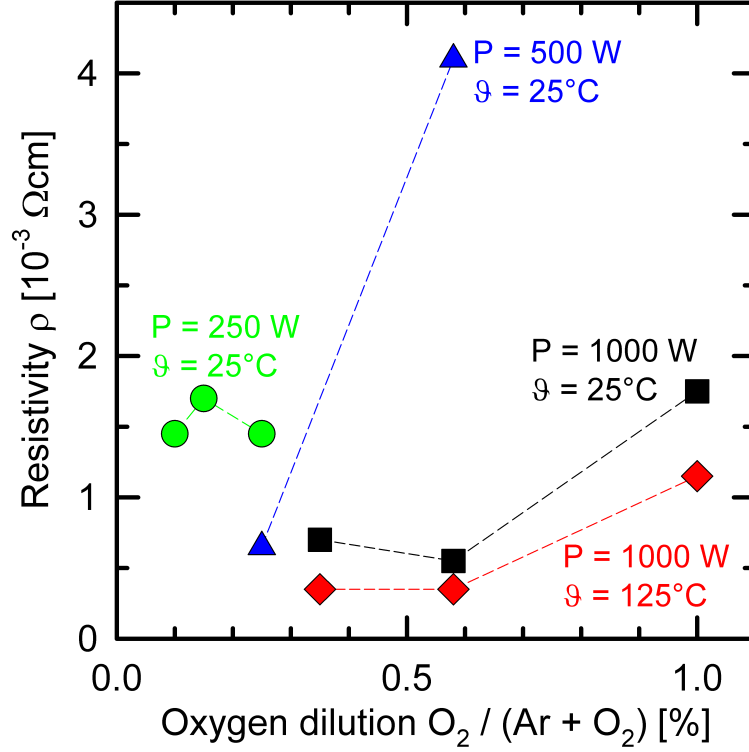
Figure 5.2: ITO resistivity as a function of O_2 dilution for different sputter powers and temperatures. The deposition pressure is 5×10^{-3} mbar.

may damage the sputter target. Therefore, we also apply double-layer ITO stacks to our test structures (Fig. 5.1), where only the first 10 nm are sputtered with low power and low oxygen to provide a low contact resistance, and on top of this first layer we sputter a second ITO layer with higher power and higher oxygen dilution, which provides a good conductivity.

Table 5.1 shows the different sputter conditions we applied in our experiment. Processes $1 - 6$ and 10 represent single-layer depositions. Processes $7 - 9$ represent ITO double-layer depositions, where processes 8 and 9 represent the ITO double layers with a low-oxygen starting layer.

Fig. 5.3 shows J-V measurements of our test structures. The graph exemplarily represents J-V measurements for n-type (red lines) and p-type (green lines) silicon test structures in the dark (dashed lines) and under illumination with 1-sun intensity (solid lines). We observe a perfect linear J-V dependence for the n-type samples. For the p-type samples we observe a slightly asymmetric behavior which may be attributed to the charge carrier transport across the p-a-Si:H/p-c-Si interface or the p-a-Si/ITO interface [21, 119]. From these J-V measurements we extract the total resistance R_{total} of the current through the entire test structure at a current density of $40\,\mathrm{mA}/cm^2$. This current density corresponds to a typical current density at the

Table 5.1: Sputter conditions for the ITO depositions.

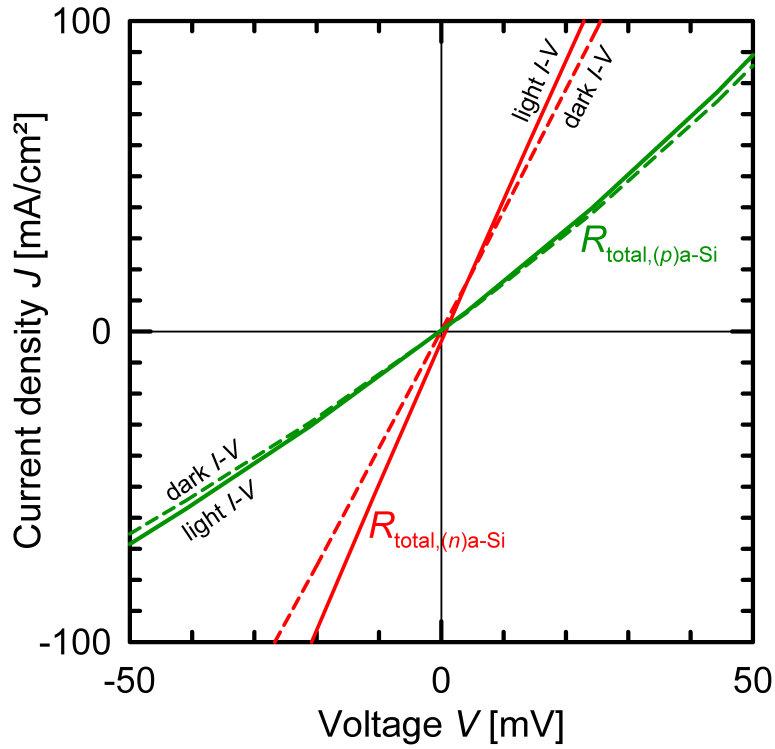| Process #:		1	2	3	4	5	6	7	8	9	10
First layer	O_2 [%]	0.35	0.58	0.35	0.25	0.58	0.35	1	0.1	0	0.58
	Power [kW]	1	1	0.5	0.5	1	0.5	1	0.25	1	1
Second layer	O_2 [%]	-	-	-	-	-	-	0.58	0.58	0.58	-
	Power [kW]	-	-	-	-	-	-	1	1	1	-
	Pressure 10^{-3} mbar	5	5	5	5	3	3	5	5	5	5
	Temperature [°C]	25	25	25	25	25	25	25	25	25	125

Figure 5.3: J-V measurements to determine the total resistance R_{total} of the electric current through the entire test structure. The graph exemplarily represents J-V measurements for n-type (red lines) and p-type (green lines) silicon test structures in the dark (dashed line) and under illumination with 1-sun intensity (solid line). The resistance R_{total} for the n-type and p-type test structures is in each case extracted for the current direction that is relevant for the operating solar cell.

working point of solar cells and all of the measured samples show an almost linear behavior of the *J-V* characteristics up to this current density. The total resistance R_{total} for the *n*-type and *p*-type test structures is extracted for the current direction that is relevant for the operating solar cell.

Fig. 5.4 shows the measured total resistance R_{total} (black + grey bars) of the test samples under illumination plotted for the different ITO deposition parameters shown in Table 5.1. Graphs A and B represent the *p*-type test structures and graphs C and D the *n*-type test structures. The samples with a high hydrogen dilution (a-Si:H^{high}) during the PECVD deposition are shown in graphs A and C, whereas the samples with a low hydrogen dilution (a-Si:H^{low}) are shown in graphs B and D.

The black bars in Fig. 5.4 represent the calculated resistance R_{rest} of the test structures without the contributions of the electrical current through the *a*-Si:H layers plus *a*-Si:H/ITO interface. R_{rest} includes the Al/*c*-Si contact resistance $R_{\text{c-Si/Al}}$, the bulk resistance of the wafer R_{bulk}, the lateral transport through the ITO layer $R_{\text{sheet.ITO}}$, the ITO/Al contact resistance $R_{\text{ITO/Al}}$ and the lateral transport through the front grid R_{grid} as indicated in Fig. 5.1. We determine all these individual series resistance contributions on separate test structures.

1. The contact resistances $R_{\text{c-Si/Al}}$ were determined via *J-V* measurements on symmetrically diffused and aluminum-contacted *p*-type and *n*-type silicon wafers. For the *p*-type samples we measure $R_{\text{c-Si/Al}} = 100\,\text{m}\Omega\,\text{cm}^2$ and for the *n*-type samples $R_{\text{c-Si/Al}} = 10\,\text{m}\Omega\,\text{cm}^2$.

2. The resistance contribution of the silicon wafer is calculated by multiplying the resistivities $\rho_{p\text{-type}} = 1.5\,\Omega\,\text{cm}$ and $\rho_{n\text{-type}} = 3\,\Omega\,\text{cm}$ with the thicknesses of the wafers.

3. The ITO/Al contact resistance $R_{\text{ITO/Al}}$ was measured on TLM [120, 121] structures for each *a*-Si:H and ITO deposition variation. A typical value is $R_{\text{ITO/Al}} = 25\,\text{m}\Omega\,\text{cm}^2$.

4. The sheet resistances of the ITO layers $R_{\text{sheet.ITO}}$ were determined via 4-point probe measurements for each individual ITO deposition condition and lie between 30 and $70\,\Omega/\square$.

5. The resistive losses due to the lateral carrier transport in the front ITO and metallization grid were calculated with an analytical model [122].

Summing up all these resistance contributions leads to a resistance of $R_{\text{rest}} = 320 \pm 10\,\text{m}\Omega\,\text{cm}^2$ for the *p*-type test samples and $R_{\text{rest}} = 200 \pm 10\,\text{m}\Omega\,\text{cm}^2$ for the *n*-type test samples (black bars in Fig. 5.4). The difference between R_{rest} of the *n*-type and *p*-type samples mainly stems from the Al/BSF ohmic contact. We attribute the difference between the measured total resistance of the test structures R_{total} (black + grey bars in Fig. 5.4) and the calculated R_{rest} (black bars in Fig.
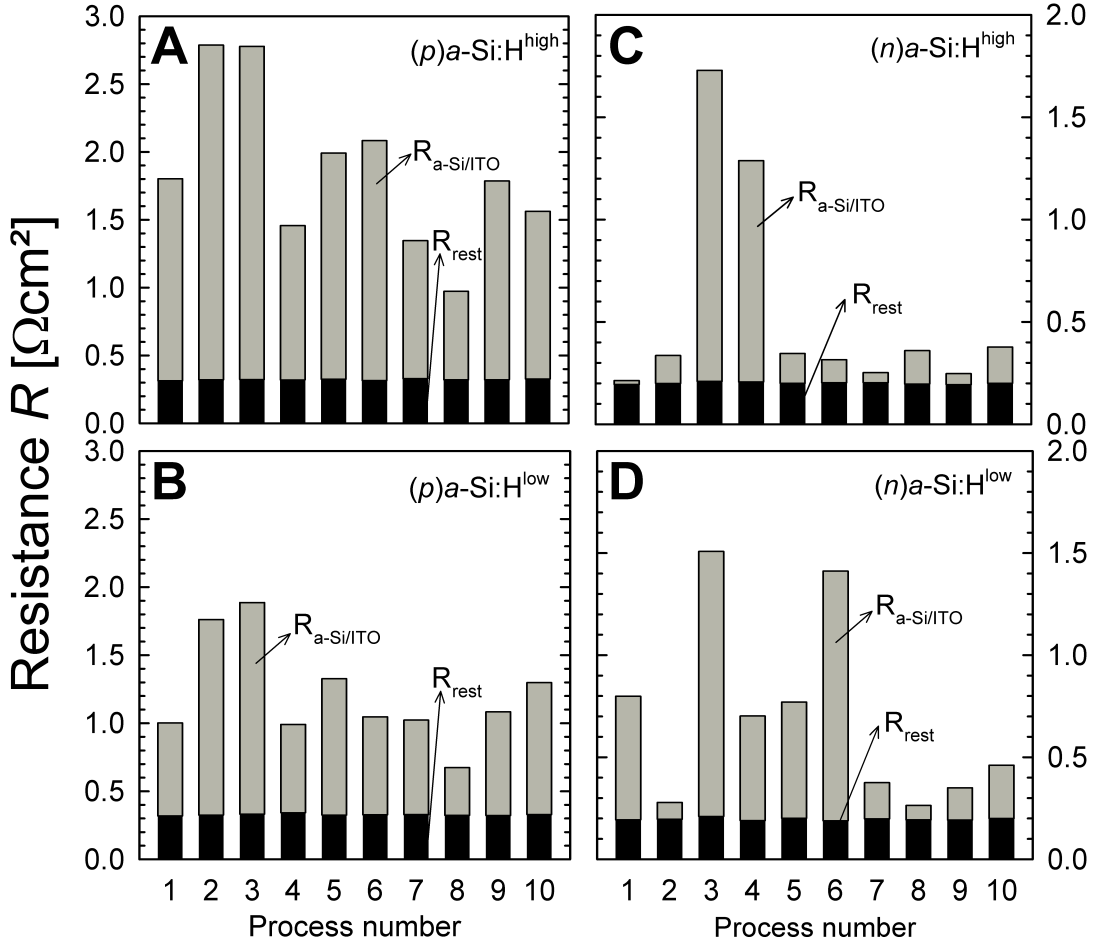
Figure 5.4: Measured total resistance R_{total} (black + grey bars) of the test structures for *p*-type (graph A and B) and *n*-type (graph C and D) samples for high (graph A and C) and low (graph B and D) hydrogen dilutions during the doped *a*-Si:H depositions. The numbers at the x-axis correspond to the ITO deposition conditions shown in Table 5.1. The black bars represent the calculated resistance R_{rest} of the test structures without the contribution of the electric current through the *a*-Si:H layers plus *a*-Si:H/ITO interface. The difference between R_{rest} of the *n*-type and *p*-type samples stems from the Al/BSF ohmic contact. The resistance of the electric current through the *a*-Si:H layers plus *a*-Si:H/ITO interface $R_{a\text{-Si/ITO}}$ (gray bars) can be calculated by subtracting R_{rest} from R_{total}.
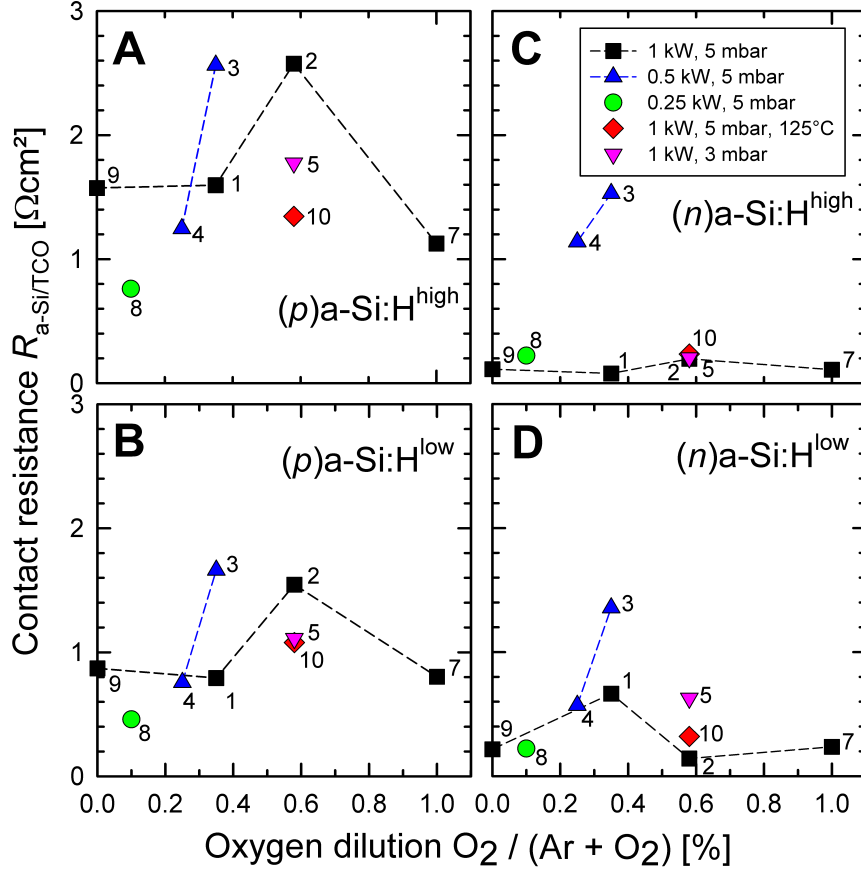
Figure 5.5: Resistance $R_{a\text{-Si/ITO}}$ of the electronic current through the a-Si:H layer plus the a-Si:H/ITO interface as a function of O_2 dilution during the ITO sputter process. Results are shown for p-type (graph A and B) and n-type (graph C and D) test structures for a hydrogen/silane ratio of 11 (graph A and C) and 5 (graphs B and D). The labels of the data points correspond to the process numbers of Table 5.1.

5.4) to the resistance of the current through the a-Si:H layer plus the a-Si:H/ITO interface $R_{a\text{-Si/ITO}}$ (grey bars in Fig. 5.4).

Fig. 5.5 shows $R_{a\text{-Si/ITO}}$ as a function of the O_2 dilution during the ITO sputter process. The two graphs A and B on the left-hand side in Fig. 5.5 show the results for the p-type test structures. The two graphs C and D on the right-hand side show the results for the n-type test structures. The two upper graphs A and C in Fig. 5.5 show the results for the a-Si:H^{high} depositions and the two lower graphs B and D for the a-Si:H^{low} depositions. The p-a-Si:H^{low} samples (Fig. 5.5B) show systematically lower values for $R_{a\text{-Si/ITO}}$ than the p-a-Si:H^{high} samples (Fig. 5.5A). The best value for $R_{p\text{-}a\text{-Si/ITO}} = 0.42\,\Omega\,cm^2$ (green circle in Fig. 5.5B) is reached for the ITO deposition #8 in Table 5.1. This deposition represents an ITO double layer with a 10 nm thick starting layer deposited using a low oxygen

flux (0.5 %) at low power (0.25 kW) and an additional 100 nm thick ITO layer that provides good conductivity. For the n-a-Si:H samples the influence of the hydrogen dilution during the PECVD deposition of the amorphous layers and the oxygen flux during the ITO sputter process is not as crucial as for the p-a-Si:H samples. For the n-a-Si:H samples we reach values $R_{n\text{-}a\text{-Si/ITO}} < 0.1\,\Omega\,\mathrm{cm}^2$ over a broad range of deposition parameters. These values for the a-Si:H/ITO contact resistances are comparable to those reported in other studies. Lee et al. reported values of $R_{p\text{-}a\text{-Si/ITO}} = 0.49\,\Omega\,\mathrm{cm}^2$ and $R_{n\text{-}a\text{-Si/ITO}} = 0.1\,\Omega\,\mathrm{cm}^2$ [123]. Based on these results, we chose the p-a-Si:H^{low} layer and ITO deposition parameters of process #8 in Table 5.1 for the fabrication of our optimized silicon heterojunction solar cells.

5.3 Solar cells

5.3.1 Experimental details

Based on our analysis of the test samples presented in Section 5.2 we have determined the optimal deposition conditions for obtaining the minimum contact resistance of the a-Si:H/ITO junction, which were the p-a-Si:H^{low} conditions, i.e., the depositions with a hydrogen-to-silane ratio of 5:1 and an ITO double layer with the sputter parameters given by process #8 in Table 5.1. In this Section, we apply these deposition parameters for the fabrication of bifacial a-Si:H/c-Si heterojunction solar cells.

We fabricate the solar cells on $125 \times 125\,\mathrm{mm}^2$ $3\,\Omega\,\mathrm{cm}$ Czochralski-grown n-type silicon wafers. The wafers were damage-etched in a KOH solution and RCA-cleaned. In order to obtain single-side textured samples, a wet thermal oxide was grown onto the wafer surfaces and subsequently removed from one side of the wafers by HF. After random-pyramid-texturing in an alkaline solution, the oxide on the rear side was removed by HF. All wafers were then RCA-cleaned again. Prior to the following a-Si:H depositions, all wafers were dipped in a 1 % HF solution and subsequently rinsed in deionized water for 1 minute and dried using dry nitrogen. Between the different a-Si:H depositions of one wafer, no extra HF dip was performed. For the a-Si:H depositions, we use a CS 400P cluster system (von Ardenne, Germany) with a 13.65 MHz parallel-plate PECVD reactor. For optimization purposes, we deposit three different i-a-Si:H layer thicknesses (5, 8.7, and 12 nm) on the front side of our solar cells. All cells were then deposited with 3 nm i-a-Si:H on the rear side. Subsequently, we deposit 15 nm n-a-Si:H onto the rear side and 15 nm p-a-Si:H onto the front side of the wafers. Prior to the following ITO depositions, all wafers were HF-dipped in a 1 % HF solution, rinsed in deionized water for 1 minute, and dried using dry nitrogen. The ITO was sputtered through a $104 \times 104\,\mathrm{mm}^2$ shadow mask. After the ITO deposition, we anneal the cells on a hotplate for 5 minutes at 175 °C. Low-temperature Ag paste was first screen-printed onto the rear side of the wafers and dried for 5 minutes at 190 °C before printing and drying the front side under the same conditions. We measure the illuminated J-V curves of the finished
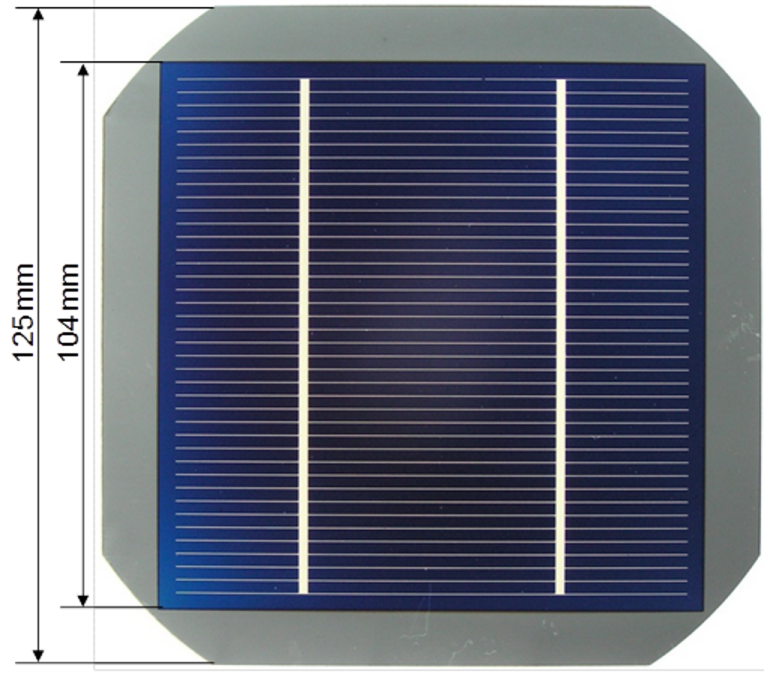
Figure 5.6: Photograph of one of our SHJ solar cells on a $125 \times 125\,\mathrm{mm}^2$ pseudo square wafer. The ITO is sputtered through a $104 \times 104\,\mathrm{mm}^2$ shadow mask. The illuminated *J-V* curves are measured through a $100 \times 100\,\mathrm{mm}^2$ shadow mask.

Table 5.2: Solar cell results.

i-Layer Thickness [nm]	η [%]	V_{OC} [mV]	J_{SC} [mA/cm^2]	*FF* [%]
5	19.9 / 19.9	711 / 712	36.6 / 37.1	76.4 / 75.4
8.7	20.2	728	36.3	76.3
12	19.8 / 19.9	731 / 733	36.0 / 36.1	75.0 / 75.0

solar cells through a $100 \times 100\,\mathrm{mm}^2$ shadow mask using the LOANA system [85]. The rear side of the cell is contacted on a brass chuck, and the two busbars on the front side are contacted with 12 equidistant contact needles. Fig. 5.6 shows a photograph of a representative *a*-Si:H/*c*-Si heterojunction solar cell.

5.3.2 Solar cell results

Fig. 5.7 and Table 5.2 show the measured cell parameters at one sun ($100\,\mathrm{mW/cm^2}$ light intensity) and $25\,°\mathrm{C}$ of our *a*-Si/*c*-Si heterojunction solar cells as a function of the *i*-*a*-Si:H layer thickness. We achieve very high open-circuit voltages V_{OC} up to $733\,\mathrm{mV}$ and efficiencies up to $20.2\,\%$.We observe an increase in V_{OC} and a decrease in J_{SC} with increasing *i*-*a*-Si:H layer thickness, as had also been reported in other studies [13]. The increase in V_{OC} is due to an improved surface passivation

for thicker i-a-Si:H layers. The decrease in J_{SC}, on the other hand, is due to a higher parasitic absorption for an increased front i-a-Si:H layer thickness.

Fig. 5.8 shows the spectrally resolved external quantum efficiency (EQE) and the reflectance data measured using the LOANA system for two different solar cells with 5 nm (green triangles) and 12 nm (red circles) i-a-Si:H layer thickness on the front side. At short wavelengths below $\lambda = 550$ nm, the solar cell with 5 nm i-a-Si:H layer shows a higher EQE that leads to a 0.65 mA/cm² increase in J_{SC} compared to the solar cell with the 12 nm i-a-Si:H layer. Unfortunately, even for the solar cells with a thin 5 nm i-a-Si:H layer, the absolute J_{SC} value of 37.1 mA/cm² is relatively poor due to a very large shading fraction of 7.8 % of the nonoptimal front metallization grid and a high absorption in the amorphous layers. The front grid coverage alone of 7.8 % of our solar cells causes a J_{SC} loss of 3 mA/cm². The absorption losses in the i-a-Si:H layer can be estimated from the slope of the J_{SC} values plotted versus the i-a-Si:H layer thickness (see Fig. 5.7). We find a current density loss of 0.1 mA/cm² per 1 nm i-a-Si:H layer thickness. The absorption losses in the p-a-Si:H layer were investigated on separate solar cells with different p-a-Si:H layer thicknesses. Here we determined current density losses of 0.12 mA/cm² per 1 nm p-a-Si:H layer thickness. This results in a total absorption loss of 2.7 mA/cm² for our best solar cell with an 8.7 nm thick i-a-Si:H layer and a 15 nm thick p-a-Si:H layer.

Using spectral ellipsometry measurements, we determine $E_{gap} = 1.72$ eV for the p-a-Si:H and $E_{gap} = 1.7$ eV for the i-a-Si:H layers. Despite the lower band gap of the i-a-Si:H layers, the current loss is less, because not all absorption in the i-a-Si:H layer is parasitic [22]. Our results are in good agreement with that of other studies. Holman et al. found J_{SC} losses of 2.8 mA/cm² from front grid shading and 3.9 mA/cm² from parasitic absorption in the a-Si:H and TCO layers [124]. Note that in our study, the absorption losses in the front TCO are not included.

5.3.3 Loss analysis

On the basis of our a-Si/c-Si heterojunction solar cells, we analyze series resistance and optical losses. We use an analytical series resistance and shading model [122] and combine this model with the recombination properties measured on our solar cells. We determine the recombination properties of our finished solar cells using $J_{SC} - V_{OC}$ measurements, as well as photoconductance decay (PCD) [125] measurements on cell precursors after ITO deposition.

Fig. 5.9 shows the $J_{SC} - V_{OC}$ (orange diamonds) and PCD (green squares) results of our best a-Si:H/c-Si heterojunction solar cell. The pseudo $J - V$ curve in Fig. 5.9 (green squares) deduced from the PCD measurement on the cell precursor before screen-printing the front grid is shifted by a current that corresponds to the J_{SC} of the finished solar cell plus the shading fraction of the front grid metallization. We describe the recombination properties of the cells using a one-diode model with variable ideality factor (see dashed lines in Fig. 5.9). For the $J_{SC} - V_{OC}$ as well as for the PCD measurements, we find that the ideality factor n at the maximum

power point of all our solar cells lies around $n = 1.2$. This imposes a fundamental limitation onto the pseudo *FF* of $82.7\,\%$ [86].

The series resistance model accounts for the resistance of the electrical current through the *a*-Si:H layers plus the *a*-Si:H/ITO interface $R_{a\text{-Si/ITO}}$, the sheet resistance of the ITO $R_{\text{sheet.ITO}}$, the contact resistance between ITO and grid metallization $R_{\text{ITO/grid}}$, the finger and busbar resistance of the front grid metallization, and the front grid geometry. We quantify all these individual series resistance contributions by the characterization of separate test structures.

For the resistance of the electrical current through the *a*-Si:H layers plus the *a*-Si/ITO interface $R_{a\text{-Si/ITO}}$, we determine values of $R_{p\text{-}a\text{-Si/ITO}} = 0.42\,\Omega\,\text{cm}^2$ and $R_{n\text{-}a\text{-Si/ITO}} = 0.1\,\Omega\,\text{cm}^2$ on our test structures as described in Section 5.2. The sheet resistance of the ITO layer is $R_{\text{sheet.ITO}} = 60\,\Omega/\square$, as determined by four-point-probe measurements. For the front and rear grid metallization, we apply low-temperature Ag screen-printing. The contact resistance between the ITO and the front grid metallization after typical drying conditions of the paste is $R_{\text{ITO/grid}} = 5\,\text{m}\Omega\,\text{cm}^2$, as measured on TLM test structures. The resulting finger width and height after the drying of the low-temperature Ag paste is $120\,\mu\text{m}$ and $18\,\mu\text{m}$, respectively. By calculating the finger cross section and measuring the finger line resistance, we determine the paste resistivity to be $14\,\mu\Omega\,\text{cm}$, which is a good value for state-of-the-art low-temperature Ag pastes [126, 127, 128]. The busbar width is $1.6\,\text{mm}$, and the finger spacing is $2.5\,\text{mm}$. This front grid geometry leads to a relatively high geometrical shading fraction of $7.8\,\%$.

Using these measured values, we are able to determine the total series resistance of our *a*-Si/*c*-Si heterojunction solar cells and calculate the $J - V$ curves under illumination (see red solid line in Fig. 5.9) on the basis of the quasi $J - V$ curves extracted from the $J_{\text{SC}} - V_{\text{OC}}$ measurements (orange diamonds in Fig. 5.9). An excellent agreement is obtained between the calculated (red solid line) and measured (red circles) $J - V$ curves in Fig. 5.9.

For the calculation of our solar cells with a $5\,\text{nm}$ *i*-*a*-Si:H layer, we use values for $R_{a\text{-Si/ITO}} = 0.53\,\Omega\,\text{cm}^2$ which are in perfect agreement with the values determined on our test structures ($R_{a\text{-Si/ITO}} = 0.52\,\Omega\,\text{cm}^2$). To adequately simulate the measured $J - V$ curves of our solar cells with $12\,\text{nm}$ *i*-*a*-Si:H layer, slightly higher values for $R_{a\text{-Si/ITO}} = 0.72\,\Omega\,\text{cm}^2$ are necessary. Hence, it is likely that the series resistance is linked to the *i*-*a*-Si:H layer thickness. However, further investigations are needed to clarify the exact physical mechanism. The higher resistance of the solar cells with a thicker *i*-*a*-Si:H layer results in a reduced fill factor and a higher offset between pseudo fill factor and actual fill factor, as can be seen in Fig. 5.7. The total series resistance of our best *a*-Si/*c*-Si heterojunction solar cell is $1.44\,\Omega\,\text{cm}^2$, which leads to a reduced fill factor of $76.3\,\%$ compared with the pseudo fill factor of $82.7\,\%$.

Fig. 5.10 and Table 5.3 show the efficiency losses in absolute percentages for each of the individual series resistance and shading contributions for our best *a*-Si/*c*-Si heterojunction solar cell. The efficiency losses that arise from carrier transport through the *a*-Si:H layers and *a*-Si:H/ITO interface lie between $0.7\,\%_{\text{abs}}$ for $5\,\text{nm}$
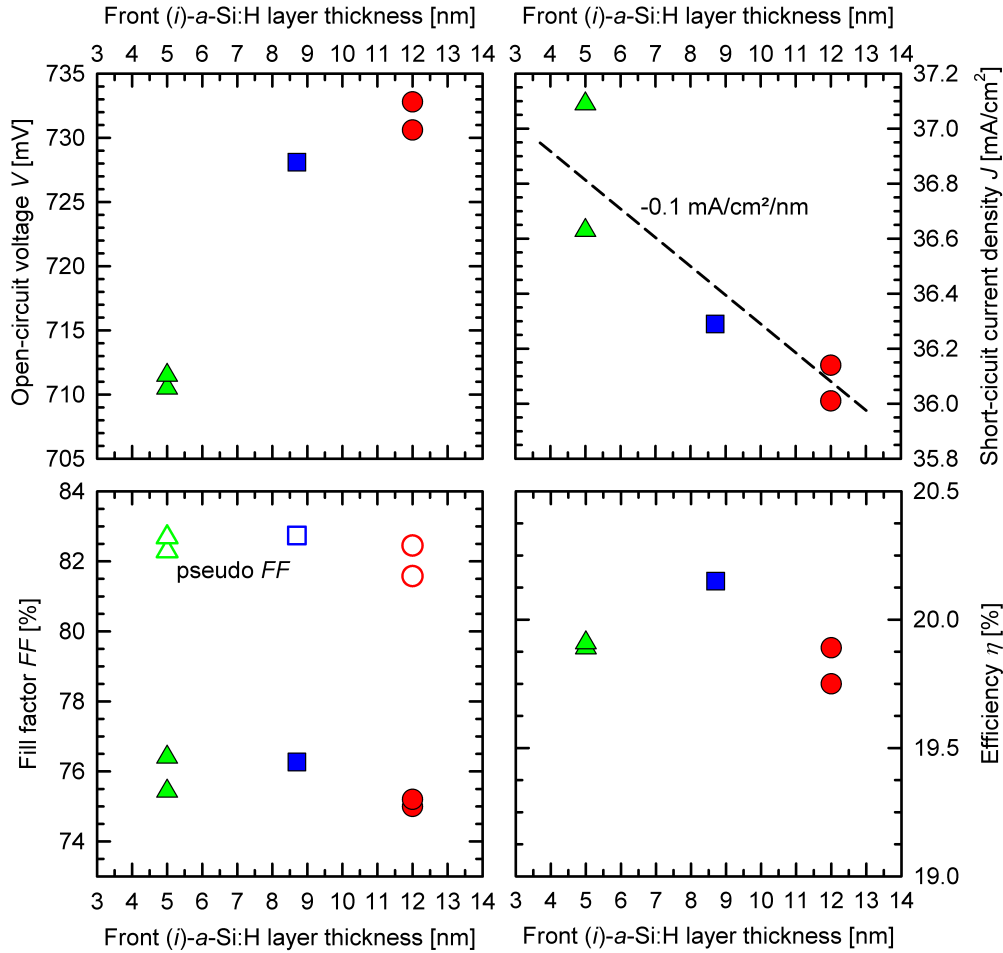
Figure 5.7: Performance of the heterojunction solar cells fabricated in this study. V_{OC}, J_{SC}, *FF*, and efficiency are plotted as a function of the (i-a-Si:H layer thickness on the front side. V_{OC} increases and J_{SC} decreases with increasing i-a-Si:H layer thickness. *FF* slightly decreases for thicker i-a-Si:H layers due to an increased series resistance.

Table 5.3: Summary of the resistance and shading losses of our solar cells.

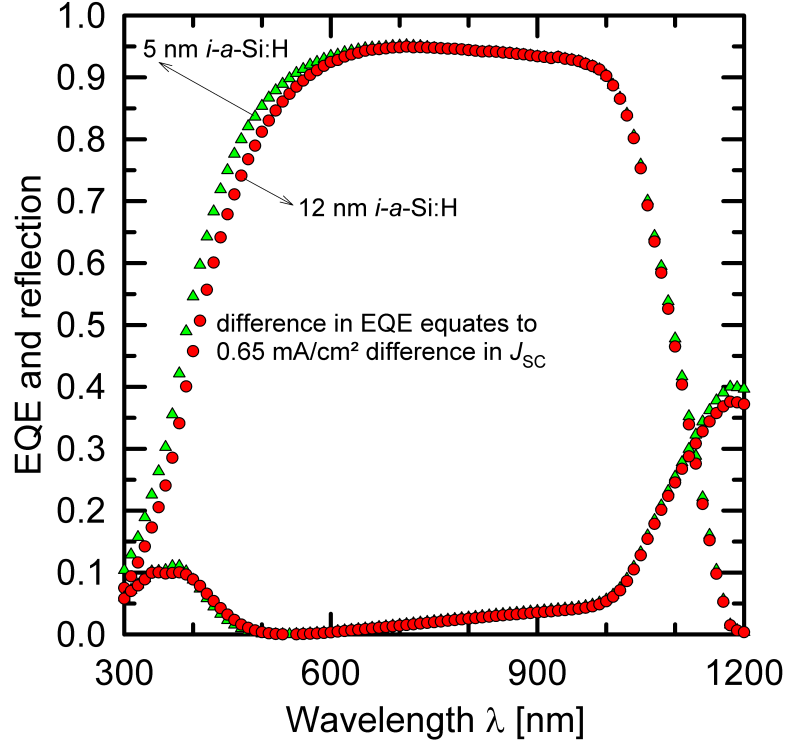| Solar Cell Efficiency:	20.2 %	Losses
. . . without the a-Si:H + a-Si:H/ITO resistance losses:	20.9 %	$0.7\,\%_{abs}$
. . . without the (lateral) ITO resistance losses:	21.3 %	$0.4\,\%_{abs}$
. . . without the Ag-paste resistance losses	22.2 %	$0.9\,\%_{abs}$
. . . without the front grid shading losses	23.8 %	$1.6\,\%_{abs}$
. . . without the front a-Si:H absorption losses	25.2 %	$1.4\,\%_{abs}$

Figure 5.8: EQE and reflectance measurements of two different solar cells with 5 nm (green triangles) and 12 nm (red circles) *i-a*-Si:H layer thickness. In the short wavelengths regime, the solar cell with only 5 nm *i-a*-Si:H layer shows a higher EQE that leads to a J_{SC} gain of 0.65 $^{mA}/_{cm^2}$ compared to the solar cell with 12 nm *i-a*-Si:H.

i-a-Si:H layers and 1.0 %$_{abs}$ for 12 nm *i-a*-Si:H layers. For the front electrode with our actual grid design with 120 μm wide and 18 μm high Ag fingers and a finger spacing of 2.5 mm, we determine efficiency losses of 1.3 %$_{abs}$ from resistive losses and 1.6 %$_{abs}$ from contact shading. The absorption losses in the amorphous layers are 1.4 %$_{abs}$. Note that this analysis does not include the absorption losses in the ITO.

5.4 Chapter summary

In this Chapter, we have presented a novel experimental method to quantify the series resistance $R_{a\text{-}Si/ITO}$ through the *a*-Si:H layers and the *a*-Si:H/ITO interface on test structures. We have presented results for $R_{a\text{-}Si/ITO}$ in dependence of the *a*-Si:H and ITO deposition parameters. The best value for for $R_{p\text{-}a\text{-}Si/ITO}$ of 0.42 Ω cm^2 was obtained for a *p-a*-Si:H deposition with a hydrogen dilution of 5 and an ITO double layer with a 10 nm thin starting layer deposited with low power and low oxygen flux that provides a low contact resistance and an additional 100 nm top layer that
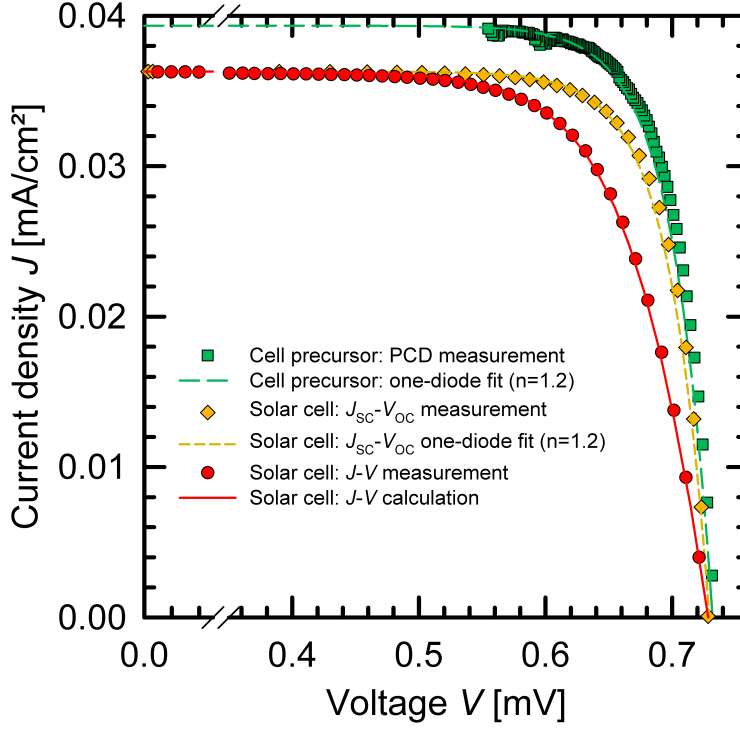
Figure 5.9: Measured (data points) and calculated (lines) *J-V* curves for our best SHJ solar cell. Recombination properties obtained from J_{SC}-V_{OC} (orange diamonds) and PCD (green squares) measurements can be well described with an one-diode model with ideality factor of $n = 1.2$ (dashed lines). Combining the recombination properties with the series resistance contributions measured on separate test structures leads to excellent agreement between calculated (red solid line) and measured (red circles) *J-V* curves.

provides good conductivity. The deposition parameters were found to be not as crucial for the *n-a*-Si:H/ITO contact. For the *n-a*-Si:H samples, we have achieved values of $R_{n\text{-}a\text{-}Si/ITO}$ below $0.1\,\Omega\,cm^2$ over a broad range of deposition parameters. Including these findings, we have performed an analysis of the series resistance and shading losses of our $100\,cm^2$ bifacial screen-printed *a*-Si:H/*c*-Si heterojunction solar cells. The efficiency losses that arise from carrier transport through the *a*-Si:H layers and the *a*-Si:H/ITO interface lie between $0.7\,\%_{abs}$ for $5\,nm$ *i-a*-Si:H layers and $1.0\,\%_{abs}$ for $12\,nm$ *i-a*-Si:H layers. The efficiency loss of $1.4\,\%_{abs}$ due to absorption in our $15\,nm$ thick *i/p-a*-Si:H front emitter can be reduced by using thinner layers. However, the largest efficiency losses of $1.6\,\%_{abs}$ and $0.9\,\%_{abs}$ were found to stem from front grid shading and resistive losses, respectively. Optimizing of the front metallization grid (finger aspect ratio, paste conductivity) would strongly increase the efficiency of our still technologically limited cell process.
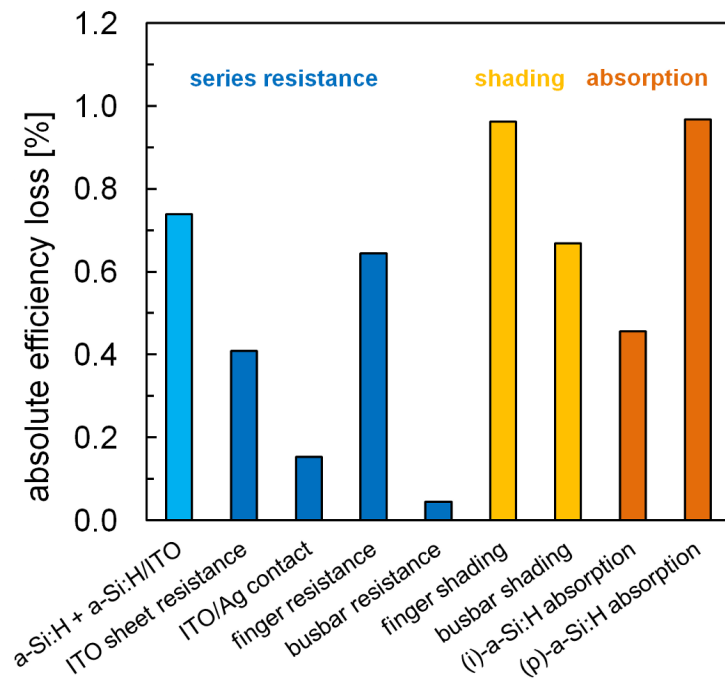
Figure 5.10: Efficiency losses in absolute percentages for each of the individual series resistance and shading contributions for our best a-Si:H/c-Si heterojunction solar cell.

6

Interdigitated back-contacted back-junction silicon heterojunction (IBC-SHJ) solar cells

The combination of the amorphous/crystalline silicon (a-Si:H/c-Si) heterojunction (SHJ) [13] and interdigitated back-junction back-contacted (IBC) [10] solar cell concepts provides a very high efficiency potential [11, 12]. In the IBC solar cell concept, the contacts for both polarities are located on the rear side of the cell. This offers the possibility to optimize the layers on the front side in terms of light trapping. Another advantage is the absence of a front metalization grid and thus the avoidance of shading losses. Therefore, this solar cell concept provides very high short-circuit current densities. Combined with the SHJ technique, which provides very high open-circuit voltages due to an excellent surface passivation and decoupling of the metalization from the c-Si surface, IBC SHJ solar cells are expected to have a very high efficiency potential.

A major challenge of the IBC SHJ concept is the potentially very high process complexity compared to two-sides contacted solar cells, because the interdigitated contact pattern of emitter and BSF fingers has to be structured on the rear side. For this reason, techniques for the structuring of the a-Si:H emitter and BSF regions as well as for the metal contacts on the rear side have to be identified. A common structuring technique in microelectronics is photolithography. In cooperation with the Helmholtz Zentrum Berlin (HZB), we have developed an IBC SHJ concept using this structuring technique. In Section 6.1, the fabricated proof-of-principle solar cells are presented. They reach efficiencies of 20.2 % which was a world record at the time of publication. However, photolithography is a much too expensive and complex process technology to be implemented in solar cell production lines. Therefore, one main focus of this Chapter is the investigation of alternative structuring techniques that are well compatible with the SHJ concept. In homo-junction IBC solar cells the structuring of the emitter and BSF regions is often done via laser ablation. However, the application to SHJ solar cells is new and therefore will be investigated in detail
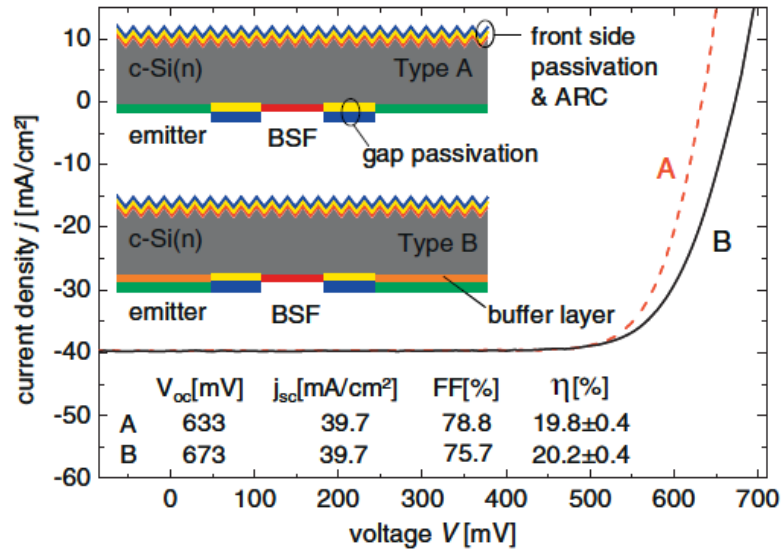
Figure 6.1: *J-V* characteristics of the fabricated IBC SHJ proof-of-principle solar cells with (B) and without (A) *i-a*-Si:H buffer layer under the *p-a*-Si:H emitter layer. The inset shows schematic cross sections and the performances values of the solar cells.

in Section 6.2. Another investigated approach is the wet-chemical structuring with etching masks, deposited using inkjet technology.

After the identification of suitable processing techniques, the fabrication of IBC SHJ solar cells with a simplified process flow will be presented in Section 6.3. In order to monitor the influence of the different process steps, process attendant lifetime measurements are performed. These measurements show pseudo efficiencies up to 24 %. The losses of the finished solar cells will be analyzed. Especially the series resistance losses will be identified using resistive network simulations. In Section 6.4, the results of the chapter will be summarized.

6.1 Proof-of-principle solar cells

In cooperation with the Helmholtz Zentrum Berlin (HZB) IBC SHJ solar cells were fabricated as described in our joined publications [99, 129, 130, 131]. The aperture area of the solar cells were $1 \times 1\,\mathrm{cm}^2$ fabricated on 4 inch, $3\,\Omega\mathrm{cm}$ FZ *n*-type silicon wafers. A schematic cross section as well as the performances for the best two solar cells are given in Fig. 6.1. The front side of the solar cells is textured and consists of a $200\,\Omega/\square$ phosphorus-diffused front surface field (FSF), passivated by thermally grown $\mathrm{SiO_2}$ and a PECVD $\mathrm{SiN_x}$ anti-reflection coating [132]. On the rear side are the amorphous emitter and BSF layers as well as a gap region, which separates both polarities. The area fractions for the *p-a*-Si:H emitter, the *n-a*-Si:H BSF and the gap region are 60 %, 28 %, and 12 %, respectively. The

gap region is passivated with a SiO_2/SiN_x stack, which provides very low surface recombination velocities [132, 133]. The front side of the solar cell as well as the gap passivation were processed at ISFH. The emitter and BSF *a*-Si:H depositions as well as the structuring steps at the rear side of the solar cells were carried out at HZB. For the BSF, a single *n*-*a*-Si:H layer was used without an intrinsic buffer layer. For the emitter, a single *p*-*a*-Si:H layer as well as an *i/p*-*a*-Si:H stack were used. The insertion of an *i*-*a*-Si:H buffer layer significantly increases the open-circuit voltage V_{OC} of the solar cells, however, at the same time decreases the fill factor due to an increased series resistance. A high efficiency of 20.2 % ($V_{OC} = 673\,mV$, $J_{SC} = 39.7\,mA/cm^2$, $FF = 75.7\,\%$) was reached, which represented a world record efficiency for this type of solar cell at the time of publication in 2011.[1]

However, the process complexity of these solar cells is very high. Taking into account all cleaning, masking, and etching sequences, 50 process steps are necessary, which is much too high for an industrial transfer. The front side itself needs 15 process steps. Another drawback is the photolithography technique for the structuring of the rear side, which includes deposition, exposure, and strip-off of the photo-resist. Three structuring processes are necessary for the structuring of the *n*-*a*-Si:H BSF, the *p*-*a*-Si:H emitter, and the gap region. Additionally, many capping layers are necessary, only to protect the layers that should not be etched during an etching step, which subsequent to the etching step then have to be removed again. Another issue of this particular solar cells is the fact that the rear interdigitated Al finger grid was directly evaporated onto the *a*-Si:H layers. In this case, the Al has to be deposited very slowly, to avoid a chemical reaction of the Al with the *a*-Si:H. However, in terms of long-term stability, a capping layer between the metalization and *a*-Si:H is of crucial importance. Such a capping layer usually is provided by a TCO. For these reasons, in the following Sections fabrication processes are investigated to simplify the fabrication complexity of the IBC SHJ solar cells.

6.2 Simplification of the solar cell process

In the previous Section a proof-of-principle IBC SHJ solar cell was presented, proving the feasibility of the concept. However, the process complexity of that solar cell is relatively high and therefore techniques are required to reduce the process complexity. Thus, in this Section different structuring techniques for the rear side of our IBC SHJ solar cells are investigated. One challenge is the structuring of the *a*-Si:H layers. Especially the partial etching of the *p*-*a*-Si:H emitter layer in

---

[1]At that time the efficiencies of IBC SHJ solar cells were in the range of 13.9 to 15.7 % [134, 135, 136]. In all cases, a limiting factor appeared to be a low fill factor of the rear contact system, attributed to different mechanisms: a contact barrier at the a-Si:H-emitter/metal interface [137], a large emitter fraction which is not covered by the contact material [138], minority carrier transport barriers [139] or resistive losses [136]. In some cases, the exploitation of the full current potential was hampered by optical losses [135, 136].
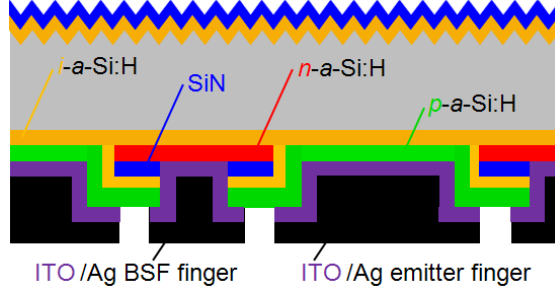
Figure 6.2: Schematic cross section of an exemplary structure to calculate the shunt resistance in the IBC SHJ solar cells without gap between emitter and BSF fingers.

presence of the *n-a*-Si:H BSF layer is critical. Another challenge is the contact separation of the rear emitter and BSF metalization. For this reason laser and inkjet techniques are investigated, and a detailed analysis of the influence of these structuring techniques on the solar cell performance will be given.

6.2.1 Gap between emitter and BSF fingers

The process complexity can easily be reduced by omitting the gap region between the emitter and BSF fingers. In this case, the *n-a*-Si:H and *p-a*-Si:H regions will be in direct contact or even overlap. A possible back side structure is shown in Fig. 6.2.[2] In this case, the *n-a*-Si:H BSF and the *p-a*-Si:H emitter regions are connected by the BSF ITO/metal finger. Here it is important to know if this would lead to shunts that negatively influence the solar cell performance. Therefore, in the following, a calculation of the shunt resistance through the *p-a*-Si:H layer will be performed.

In Section 3.3.1, the *p-a*-Si:H conductivity was identified to be $10^{-5}\,\mathrm{S/cm}$. The lateral resistance through the *p-a*-Si:H can be calculated using the equation

$$R = \rho \cdot b \cdot \frac{1}{l \cdot d}\,, \tag{6.1}$$

where ρ is the resistivity of the *p-a*-Si:H layer, b is the width of the contact openings, l is the length of the metal fingers, and d is the thickness of the *p-a*-Si:H layer. For the shunt resistance R_{shunt} of the entire solar cell, the number of fingers and the cell area A must be considered:

$$R_{\mathrm{shunt}} = R \cdot \frac{A}{\text{number of fingers}}\,. \tag{6.2}$$

---

[2]This structure is chosen here because it represents the actual structure of the fabricated IBC SHJ cells presented in Section 6.3.

Assuming a $2 \times 2\,\text{cm}^2$ solar cell with a finger index of $1\,\text{mm}$, a p-a-Si:H layer thickness of $20\,\text{nm}$, and a contact opening width of $100\,\mu\text{m}$, and the given p-a-Si:H conductivity of $10^{-5}\,\text{S/cm}$, the resulting shunt resistance is $R_{\text{shunt}} = 25\,\text{k}\Omega\,\text{cm}^2$. This value is large enough to avoid any detrimental impact on the solar cell performance. Consequently, when the spacing between emitter and BSF fingers is not too narrow, the shunt resistance is negligible. Therefore, a gap region between the p-a-Si:H and n-a-Si:H layer is not necessary and will not be considered in the following concepts.

6.2.2 Laser structuring

A possibility to simplify the IBC SHJ fabrication process is the substitution of the photolithography steps by laser structuring. The advantage of laser processing is the omission of several masking, drying, and stripping steps of the photo-resist. However, while laser ablation is a well established process for the fabrication of homo-junction IBC solar cells, it was not investigated for the structuring of SHJ solar cells so far. A special challenge is the ablation of the a-Si:H layers from the c-Si substrate without inducing a damage to the silicon crystal or a sufficient post treatment which removes the induced laser damage and allows for a sufficient re-passivation with a-Si:H. For this reason different laser processes and parameters are investigated in the following Section.

Rear Interdigitated Single Evaporation (RISE) heterojunction solar cells

In this Section the adaption of the RISE (Rear Interdigitated Single Evaporation) concept [140, 141] for the fabrication of IBC SHJ solar cells is investigated. The RISE process was developed at the ISFH for the fabrication of high-efficiency IBC homo-junction solar cells, comprising an elegant process flow for the structuring of the emitter and BSF regions as well as for the metal contact separation. However, the feasibility of the RISE process flow for the fabrication of IBC SHJ solar cells has to be investigated. A possible process flow is schematically shown in column A of Fig. 6.3. For simplicity, only the process steps for the rear side are presented. (1) On a RCA cleaned wafer the i/n-a-Si:H BSF is deposited and capped with a SiN$_\text{x}$. (2) Then the i/n-a-Si:H/SiN$_\text{x}$ stack is ablated with a laser, thereby inducing damage to the silicon crystal. (3) Subsequently, the damaged c-Si is etched away in a KOH solution, where the SiN$_\text{x}$ serves as etching barrier in the non-ablated areas. A consequence are trenches in the regions where the KOH etches the silicon. The resulting steps are typically 5-20 μm high. (4) The sample is then RCA cleaned again and deposited with the i/p-a-Si:H emitter stack. (5) In a subsequent laser step, the emitter stack is ablated from the SiN$_\text{x}$ capping layer. The challenge here is not to damage the c-Si crystal in the ablated areas. This technique will be investigated in the following Section. (6) Afterwards, the SiN$_\text{x}$ capping layer is removed in HF and (7) the full rear side is deposited with ITO and (8) metal. (9) On the flanks of the trenches the metal is very thin and porous and can be
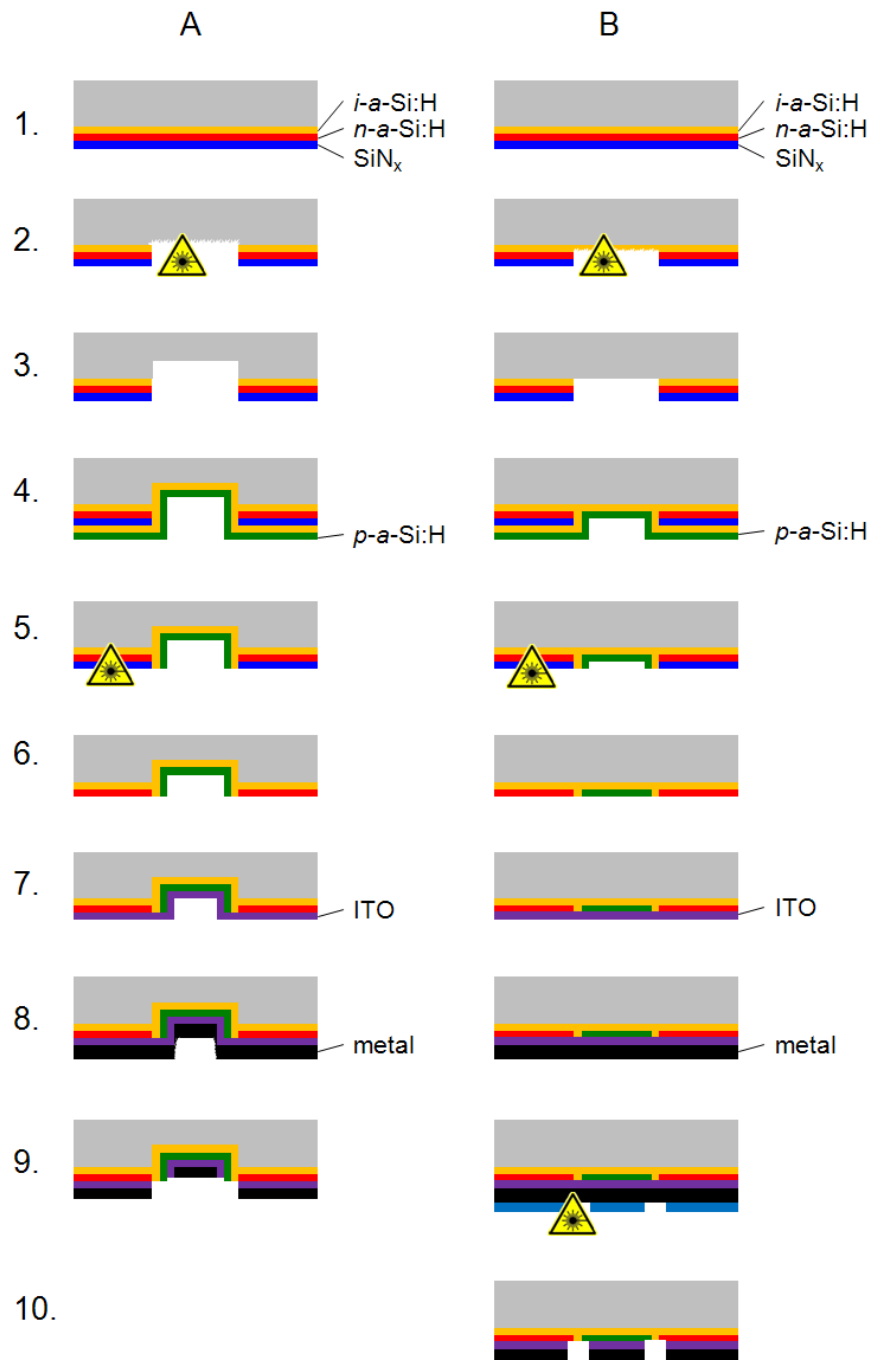
Figure 6.3: Schematic process flows with laser structuring techniques. Column A represents a process with laser damage in the *c*-Si substrate. Etching off the induced crystal damage leads to steps on the rear side, which could be used for the RISE contact separation. Column B represents a process with a damage-free laser ablation of the *a*-Si:H layers.
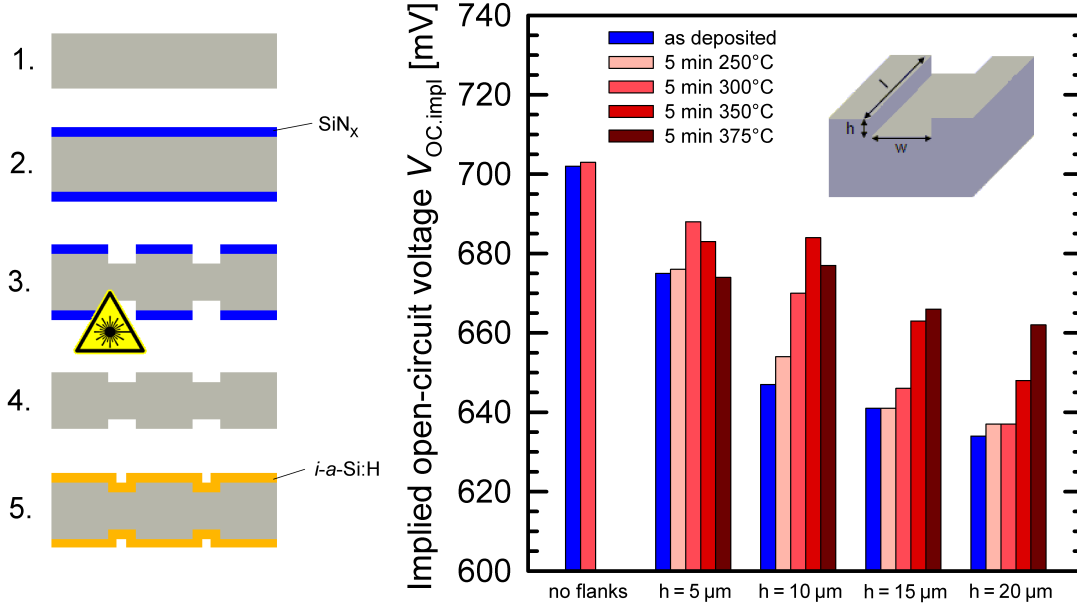
Figure 6.4: On the left-hand side, the process flow of the test samples for the *i*-*a*-Si:H passivation of different flank heights is presented schematically. In the graph on the right-hand side, the $V_{OC.impl}$ values of the test samples are shown for different flank heights h. The blue bars represent the initial $V_{OC.impl}$ values after the *a*-Si:H deposition, and the red bars after gradual annealing. The $V_{OC.impl}$ values decrease with increasing flank height.

selectively etched off in an etching solution. Also the ITO is etched in this process step, and so the contact separation is performed.

In the IBC SHJ solar cell process, the trenches that arise from the KOH damage etch in step (3) have to be re-passivated with the i/p-*a*-Si:H emitter stack. To test the passivation quality of such trenches, test samples were fabricated as schematically shown on the left side of Fig. 6.4. On $3\,\Omega$cm *n*-type Czochalski-grown silicon wafers, we deposit a SiN_x layer, which subsequently is partially ablated with a line pattern. The width of the lines is $w = 1\,\text{mm}$, the length $l = 2.5\,\text{mm}$ and the index $2\,\text{mm}$. As a reference some samples were not laser-ablated. Afterwards, the samples are etched in KOH for different durations, so that the resulting heights h of the flanks are 0, 5, 10, 15, and $20\,\mu\text{m}$. Then, the SiN_x is removed in HF and after an RCA cleaning sequence, the sample is passivated by a $10\,\text{nm}$ thin *i*-*a*-Si:H layer and measured using PCD. The resulting $V_{OC.impl}$ values are presented as blue bars in the graph in Fig. 6.4. The $V_{OC.impl}$ values decreases with increasing flank heights. Therefore, we calculate the effective surface recombination velocity S_{flank} on the flanks. Using the equation

$$\frac{1}{\tau_{\text{eff. with flanks}}} = \frac{1}{\tau_{\text{eff. without flanks}}} + \frac{\text{area fraction of flanks}}{W} \cdot S_{\text{flank}} \qquad (6.3)$$

Table 6.1: Calculated S_{eff} values for samples with different flank heights.

flank height h	$S_{\text{flank before anneal}}$	$S_{\text{flank after anneal}}$
$5\,\mu$m	$9451\,\text{cm}/\text{s}$	$4557\,\text{cm}/\text{s}$
$10\,\mu$m	$12891\,\text{cm}/\text{s}$	$2723\,\text{cm}/\text{s}$
$15\,\mu$m	$11168\,\text{cm}/\text{s}$	$4520\,\text{cm}/\text{s}$
$20\,\mu$m	$10670\,\text{cm}/\text{s}$	$4120\,\text{cm}/\text{s}$

we obtain

$$S_{\text{flank}} = \left(\frac{1}{\tau_{\text{eff. with flanks}}} - \frac{1}{\tau_{\text{eff. without flanks}}} \right) \cdot \frac{W \cdot \text{area of sample}}{l \cdot h \cdot \text{number of flanks}} . \qquad (6.4)$$

The calculated S_{flank} values are shown in Table 6.1. Independent of the flank heights we determine values of $S_{\text{flank}} \approx 10^4\,\text{cm}/\text{s}$. This very high surface recombination velocity on the vertical flanks stems from a much thinner effective thickness of the i-a-Si:H passivation layer at the flank surfaces. Annealing at high temperatures increases the $V_{\text{OC.impl}}$. However, the resulting $V_{\text{OC.impl}}$ is still low after annealing at $375\,°$C. Therefore, using the RISE structuring in the fabrication of IBC SHJ solar cells, the major advantage of the SHJ concept, i.e. the outstanding V_{OC} potential, is lost. Consequently, the RISE technique is not favorable for the fabrication of IBC SHJ solar cells.

Laser ablation of *a*-Si:H

In the previous Section, laser ablation of an a-Si layer from a c-Si substrate with inducing damage to the subjacent silicon crystal and subsequent etching of the laser damage was elucidated. In this Section, it will be investigated if the a-Si:H layers can in principle be laser-ablated without inducing damage to the c-Si crystal. This is of importance because in contrast to highly doped diffused homo-junction solar cells, the surface passivation quality of a-Si:H layers in SHJ cells is extremely sensitive to the surface properties and thus to an induced laser damage.

A possible process flow for such a solar cell is schematically shown in column B of Fig. 6.3. For simplicity, only the process steps for the rear side are presented. (1) On an RCA-cleaned silicon wafer, the i/n-a-Si:H BSF is deposited and capped with a SiN$_x$ layer. (2) Subsequently, the i/n-a-Si:H stack is partially laser-ablated. (3) The wafer surface is then prepared/cleaned in a way that (4) it can be re-passivated with an i/p-a-Si:H emitter stack. (5) In a subsequent laser step, the i/p-a-Si:H emitter stack is ablated from the SiN$_x$ capping layer without damaging the i/n-a-Si:H BSF stack and a-Si:H/c-Si interface in the ablated areas. (6) Afterwards, the SiN$_x$ capping layer is removed in HF and (7) the full rear side is coated with ITO and (8) metal. (9) A possibility for the contact separation is the deposition of an etch resist onto the metal layer, which then is structured by a laser. (10) In the
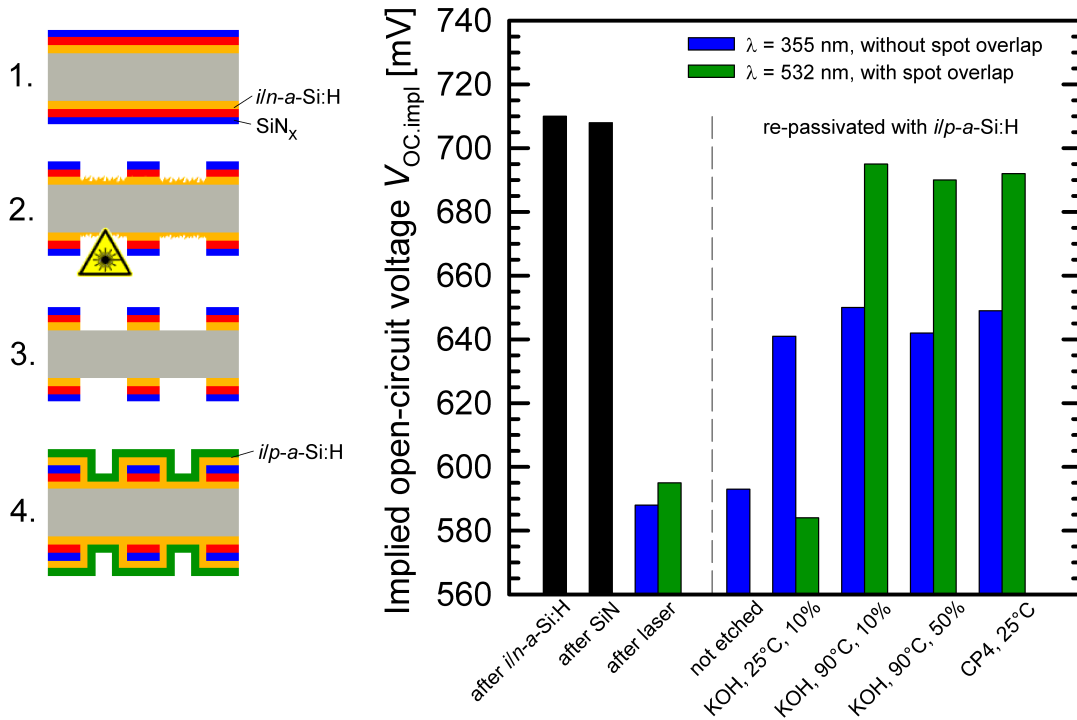
Figure 6.5: On the left-hand side, the process flow of the test samples is shown schematically. The graph on the right-hand side shows the measured $V_{OC.impl}$ values after the SiN_x and i/n-a-Si:H depositions as well as after re-passivation of the ablated area with a i/p-a-Si:H stack after different damage etches.

final step, the metal and ITO are etched in a chemical solution to separate both polarities.

We first investigate the feasibility of the damage-free laser ablation of the i/n-a-Si:H BSF stack represented by process steps (2)-(4) in Fig. 6.3. For this reason, symmetrical test structures were fabricated as schematically shown on the left side of Fig. 6.5. On 2.5×2.5 cm^2, $3\,\Omega$cm, n-type Cz-Si wafers an i/n-a-Si:H stack (5 nm/15 nm) and a SiN_x capping layer ($n = 1.9$, $d = 100$ nm) was deposited. Then, the i/n-a-Si:H/SiN$_x$ stack was ablated with a pico-second laser (Lumera, SuperRapid, Nd:YVO$_4$, pulse duration 8 ps, repetition rate 200-300 kHz) with two different wavelengths, i.e. 532 nm and 355 nm. The laser power was adjusted in a way that it was just high enough to ablate the i/n-a-Si:H/SiN$_x$ stack. The width of the ablated lines is 500 μm and the index 1000 μm.

To ablate the i/n-a-Si:H/SiN$_x$ stack over the desired area, the circular laser spots have to overlap. With the 532 nm wavelength laser we ablated the layers in a way, that the laser spots overlap. For the 355 nm wavelength, the laser was adjusted in a way that the spots do not overlap. However, in this case only 70 % of the area is really ablated. The optical microscope image on the left-hand side of Fig.6.6
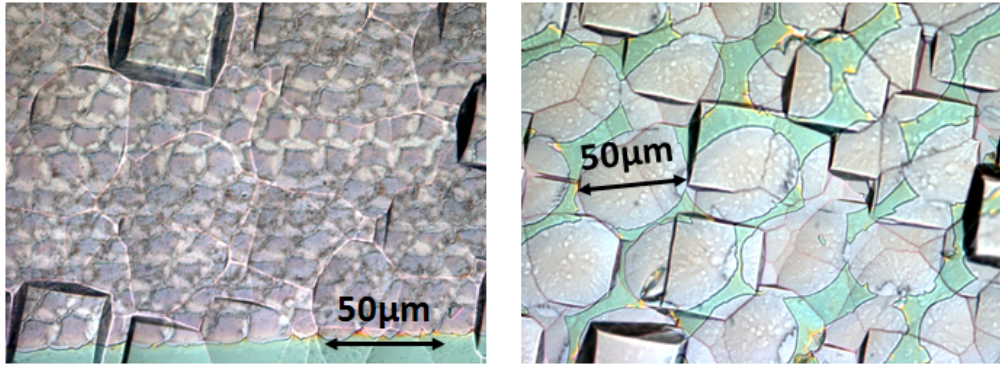
Figure 6.6: Left: Optical microscope image of a test wafer after laser ablation with 532 nm wavelength with laser spot overlap. The gray areas indicate a damaged silicon crystal. Right: Optical microscope image of a test wafer after laser ablation with 355 nm wavelength without laser spot overlap. In this case, the a-Si:H/SiN$_x$ is not ablated completely, which can be seen as green areas.

shows a sample after laser ablation using the 532 nm laser and spot overlap. The gray areas in the image can be interpreted as a laser damage induced to the silicon crystal. Therefore, also samples without overlap were fabricated. The microscope image on the right-hand side of Fig.6.6 shows a sample after laser ablation using 355 nm wavelength without laser spot overlap. The non-ablated regions are visible as green areas. No laser damage is visible.

It can be expected that the a-Si:H layer is not ablated completely from the c-Si substrate after the laser ablation process. Therefore, in order to remove all residuals, the samples are exposed to different chemical solutions to remove the remaining and damaged a-Si:H before re-passivation with an i/p-a-Si:H stack. For this purpose a 10 % concentrated KOH solution at 25 °C for 10 minutes and at 90 °C for 1 minute, as well as a 50 % concentrated KOH solution at 90 °C for 20 seconds, and a CP4 etching solution at 25 °C for 20 minutes were used. As a reference, some of the samples were not etched before re-passivation. After an additional RCA cleaning sequence the samples were then re-passivated by an i/p-a-Si:H stack (5 nm/15 nm) and measured using PCD.

The graph in Fig. 6.5 shows the $V_{\text{OC.impl}}$ values of the test samples before and after applying the different etching solutions. The initial $V_{\text{OC.impl}}$ values after the i/n-a-Si:H and SiN$_x$ deposition lie at 710 mV. After ablation of the i/n-a-Si:H/SiN$_x$ stack the $V_{\text{OC.impl}}$ is drastically decreased to values of 590 mV for both laser wavelengths with and without spot overlap. Direct re-passivation with an i/p-a-Si:H stack without etching of the wafer surface does not lead to an increase of $V_{\text{OC.impl}}$. However, re-passivation after 532 nm laser with overlap leads to $V_{\text{OC.impl}}$ values of approximately 690 mV for all damage etches except the 25 °C KOH. We assume that in this case the etching solution can not sufficiently remove the "baked" i/n-a-Si:H residuals. Re-passivation after 355 nm laser without overlap leads to maximum $V_{\text{OC.impl}}$ values of approximately 650 mV, independent of the damage
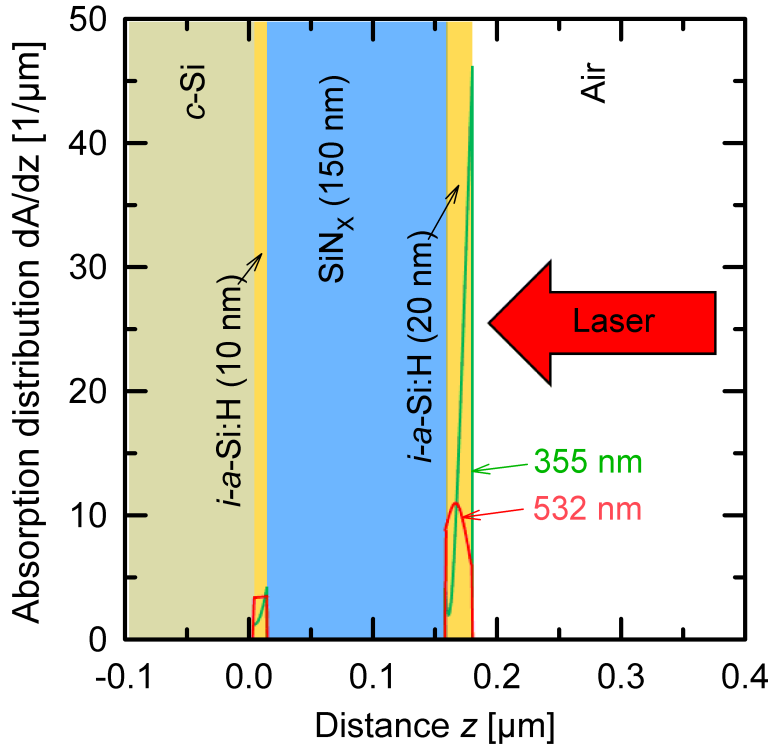
Figure 6.7: Absorption distribution against the penetration depth for a c-Si/a-Si:H/SiN$_\text{x}$/a-Si:H stack and two different wavelengths of the incoming laser light.

etch applied. A plausible explanation for the reduced $V_{\text{OC.impl}}$ values of the samples without laser spot overlap is under-etching of the remaining i/n-a-Si:H/SiN$_\text{x}$ stack. In this case, the remaining SiN$_\text{x}$ shields the under-etched regions from re-deposition with the i/p-a-Si:H stack.

It can be concluded that laser ablation of an a-Si:H layer on a c-Si wafer requires damage etching before re-passivation. However, the initial passivation quality cannot be fully regained, even after damage etching. A possible explanation for this observation is that the edges of the structured regions (including the remainig "islands" without spot overlap) cannot be sufficiently re-passivated because of under-etching of the SiN$_\text{x}$ capping layer.

A second application for laser ablation is the structuring of the i/p-a-Si:H emitter stack. In a solar cell structure, the i/p-a-Si:H emitter would be positioned above a layer stack of the i/n-a-Si:H BSF and a SiN$_\text{x}$ capping layer, as indicated in step 5 of Fig. 6.3. The challenge is to ablate the i/p-a-Si:H emitter without damaging the subjacent i/n-a-Si:H BSF layer and the a-Si:H/c-Si interface. Fig. 6.7 shows simulations of the absorption distribution in an a-Si:H/SiN$_\text{x}$/a-Si:H layer stack. The absorption is dependent on the laser wavelength (355 nm and 532 nm), as well as on the refractive index and thickness of the a-Si:H and SiN$_\text{x}$ layers. In the
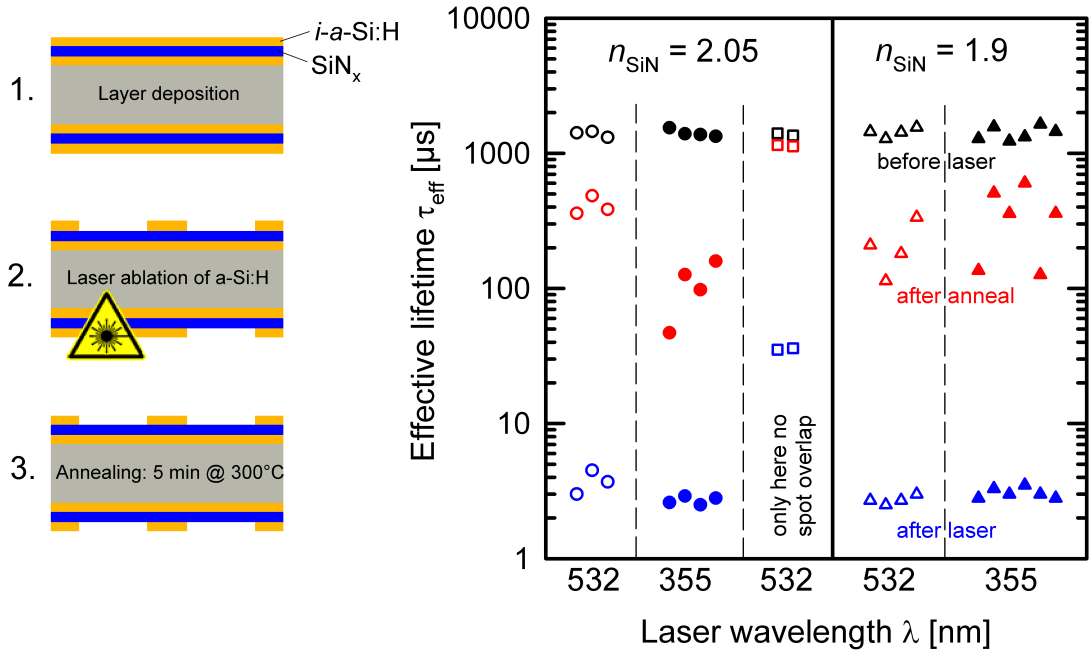
Figure 6.8: On the left-hand side, the process flow of the test samples is shown schematically. The graph on the right-hand side shows the measured effective lifetimes of samples before and after laser ablation, and after an additional annealing step. The effective lifetime is given for different SiN_x layers, laser wavelengths (open/closed symbols), and for samples with (circles and triangles) and without (squares) overlap of the laser spots.

simulation, it is observable that most of the incoming laser light is absorbed in the first a-Si:H layer. However, a non-negligible fraction is also absorbed in the a-Si:H passivation layer located between the c-Si wafer and the SiN_x capping layer, which could lead to a decreased passivation quality.

In order to verify this assumption experimentally, symmetrical test samples were fabricated on $2.5 \times 2.5\,\text{cm}^2$, $1.5\,\Omega\text{cm}$, p-type FZ silicon wafers. A schematic representation of the samples is shown in Fig. 6.8. After RCA cleaning, the wafers were deposited with $10\,\text{nm}$ i-a-Si:H, serving as a dummy for the i/n-a-Si:H BSF stack. Afterwards, a $100\,\text{nm}$ SiN_x layer was deposited onto the samples. Two different refractive indices ($n = 1.9$ and $n = 2.05$ at $\lambda = 632\,\text{nm}$) and therefore different optical absorption properties were applied. The higher the refractive index at $632\,\text{nm}$, the higher is the absorption in the SiN_x layer. Then, the samples were deposited with $20\,\text{nm}$ i-a-Si:H, serving as a dummy for the i/p-a-Si:H emitter stack. In a next step the first a-Si:H layer was laser-ablated with two different wavelengths ($355\,\text{nm}$ and $532\,\text{nm}$). The laser power was adjusted in a way that is was just high enough to ablate the first a-Si:H layer. However, a distinct threshold for the laser power does not exist, because lowest inhomogeneities of the layer thicknesses change the ablation characteristics. Fig. 6.9 shows optical microscope images of
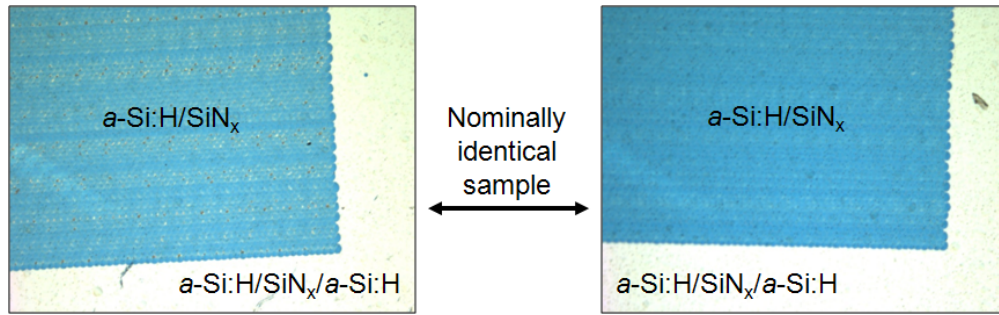
Figure 6.9: Optical microscope images of two nominally identical test samples for the ablation of an a-Si:H layer from an a-Si:H/SiN$_x$ stack. The gray area represents the a-Si:H/SiN$_x$/a-Si:H layer stack, whereas the blue area represents the ablated region. Although the samples were ablated with the same laser parameters, the gray spots in the left image indicate residuals of a-Si:H on the ablated area or damaging of the subjacent c-Si.

two nominally identical samples. Although both samples were ablated with the same laser power, they differ in appearance. The lighter spots of the image on the left-hand side indicate residuals of a-Si:H on the ablated area or an induced damage to the c-Si substrate.

For each variation of wavelength and refractive index, Fig. 6.8 shows lifetime results from QSSPC measurements, after deposition of the a-Si:H/SiN$_x$/a-Si:H layer stack (black symbols), after laser structuring (blue symbols), and after an annealing step at 300 °C for 5 minutes (red symbols). The circles and triangles represent samples, where the a-Si:H layer was ablated with spot overlap. The filled symbols belong to laser ablations with 355 nm wavelength and the open symbols belong to laser ablations with 532 nm wavelength. It can be observed that the passivation quality is drastically decreased after the laser ablation (blue data points). Even the annealing step cannot fully restore the initial lifetime, independent of laser wavelength or SiN$_x$ refractive index (red data points). Instead, the two squared data points represent samples which were laser-ablated without spot overlap. For these samples the damage directly after laser-ablation (blue squares) is not as high as for the samples which are ablated with spot overlap. Additionally, the passivation quality of these samples can be regained by an annealing step at 300 °C for 5 minutes (red open squares).

A possible explanation is illustrated in Fig. 6.10. With the first laser shot, the a-Si:H layer is already ablated. A part of the second shot is therefore not absorbed in the first a-Si:H layer, reaches the second a-Si:H passivation layer, and damages the a-Si:H/c-Si interface. In this way, every further shot additionally decreases the passivation quality. Instead, when ablating without overlapping laser spots, less power reaches the buried a-Si:H passivation layer and therefore the effective lifetime of the sample is higher.

It can be concluded that laser ablation of an a-Si:H layer from an a-Si:H/SiN$_x$/a-Si:H layer stack with laser spot overlap leads to not-curable damage of the subjacent
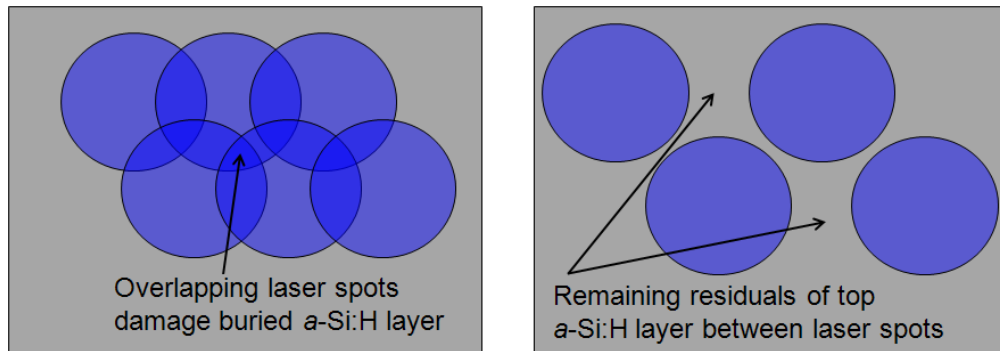
Figure 6.10: Schematic presentation for the laser ablation of an *a*-Si:H layer with (left picture) and without (right picture) laser spot overlap.

a-Si:H passivation layer. Instead, local ablation without laser spot overlap is possible in a way that after an additional annealing step the initial passivation quality can be fully restored. In principle, the edge of the structured region is not critical in this case. However, a punctual ablation of the upper *a*-Si:H emitter layer allows only a punctual contacting of the subjacent *a*-Si:H BSF layer. In the case of poor contact resistances, this will increase the transport losses across the heterojunction.

Conclusions: laser structuring techniques

Laser ablation is not an easy method for the structuring of *a*-Si:H layers in the fabrication of IBC SHJ solar cells. Laser ablation for the structuring of IBC SHJ solar cells is potentially applicable for individual processes, however, it will often require compromises in terms of process flow, device design, and performance. In general, laser ablation of an *a*-Si:H layer directly located on the *c*-Si wafer seems to be inapplicable, because a wet-chemical post treatment is necessary and the passivation quality is decreased. We have shown however, that laser ablation can be applied in the case of non-overlapping laser spots and a post-annealing treatment. For this case we demonstrated the full regain of the passivation quality.

6.2.3 Inkjet structuring

An alternative technique for laser ablation is the wet-chemical structuring of the *a*-Si:H layers through etching masks. A disadvantage of this method is the higher process complexity due to additional depositions of etching masks or capping layers. However, a distinct advantage is the possibility of low-damage structuring of the *a*-Si:H layers. Besides photolithography, these etching masks can also be deposited with the industrially relevant inkjet technology. Using an inkjet tool (PixDro LP50) a hot-melt wax (Crystal Hep 9522 Clear, SunChemical), which dries at ambient air and serves as etching mask, can be structured onto the sample. The used hot-melt wax resists to acids, but etches off in alkaline solutions. Since we
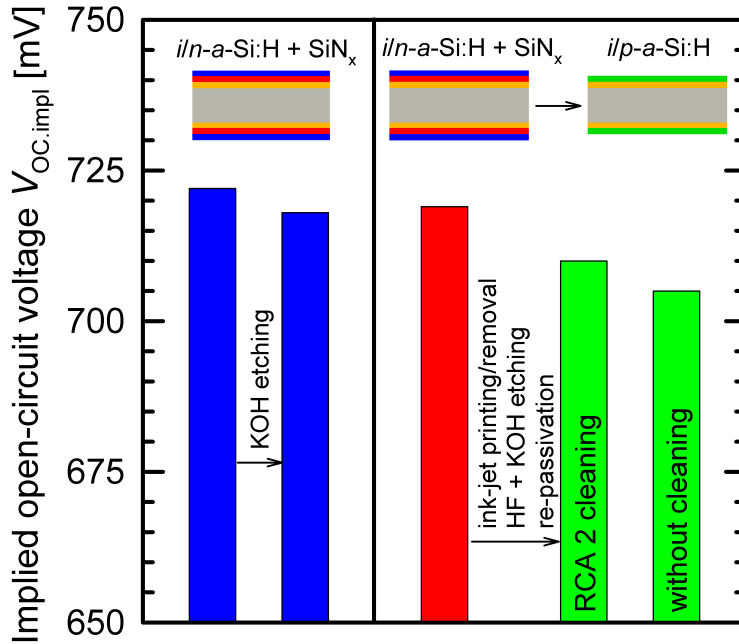
Figure 6.11: Implied open-circuit voltages $V_{\text{OC.impl}}$ of samples to test the passivation quality after different inkjet process steps.

use a $10\,\%$ concentrated KOH solution at $25\,°C$ for etching the $i/n\text{-}a$-Si:H BSF stack, an additional capping layer for the structuring is needed. For this purpose, we use a SiN_x capping layer, which is structured with HF through the printed hot-melt etching mask. Afterwards, the hot-melt wax is removed with IPA and the structured SiN_x layer serves as etching mask against the KOH solution during the $i/n\text{-}a$-Si:H BSF removal. The durability of the SiN_x capping layer and the passivation quality of the subjacent $i/n\text{-}a$-Si:H BSF stack during the KOH etching are investigated on test samples, as can be seen on the left-hand side of Fig. 6.11. The test samples were symmetrically deposited with an $i/n\text{-}a$-Si:H/SiN_x stack and exposed to the KOH etching solution for $5\,$minutes. The most left blue bar in Fig. 6.11 shows the initial $V_{\text{OC.impl}}$ before etching and the right blue bar shows the $V_{\text{OC.impl}}$ after etching the sample in the KOH solution for $5\,$minutes. Although the necessary time for etching the $i/n\text{-}a$-Si:H layer stack is only $1\,$minute, even after $5\,$minutes etching only a slight decrease of the $V_{\text{OC.impl}}$ is observable.

In a solar cell process, the etched regions need to be re-passivated with an $i/p\text{-}a$-Si:H emitter stack. Therefore, we also tested if additional cleaning steps are necessary to remove potential residuals of the hot-melt wax after the structuring sequence and to clean the c-Si surface sufficiently for the following a-Si:H deposition. To simulate the etching process we again fabricated samples symmetrically deposited with an $i/n\text{-}a$-Si:H/SiN_x stack, which were then fully printed with the hot-melt wax. Afterwards, the wax was removed with IPA, the SiN_x was etched in HF,

and the i/n-a-Si:H BSF was etched in KOH. Before the re-passivation by the i/p-a-Si:H emitter stack, half of the samples were cleaned in HCl + H_2O_2 (RCA 2 cleaning) and the other half received no extra cleaning. The samples with the extra cleaning show higher $V_{OC.impl}$ values, and therefore this cleaning is implemented in our process flow which will be presented in Section 6.3. Note that all measured $V_{OC.impl}$ values lie well above $700\,mV$. Hence, an excellent passivation level can be maintained during inkjet processing.

6.2.4 Metal contact separation

The n-a-Si:H BSF and p-a-Si:H emitter regions that have to be contacted are present in an interdigitated finger pattern on the rear side of the solar cell. The electrical separation of the metal fingers of both polarities is crucial for an IBC solar cell to avoid shunts. For a practically feasible and long-term stable contact formation, the direct contact between a-Si:H layers and metal has to be avoided. Instead ITO/metal stacks are used. To avoid additional process and alignment steps, the simultaneous structuring of the ITO and metal layers is preferred. Hence, we examine the structuring of a full-area deposited ITO/metal stack through a capping layer. The capping layer can be structured using inkjet or laser technology. The ITO/metal stack can then be structured wet-chemically in one process step. As an attractive alternative, an Ag finger grid was screen-printed onto a full-area-deposited ITO layer. In this case, the Ag grid serves as etching mask during the ITO etching.

  The simultaneous etching of the ITO/metal stack turned out to be challenging. The etching rate of the ITO is much higher compared to that of the metal, which locally leads to uncontrollable under-etching to the point of lift-off of the metal layer. Optical microscope images of test structures are shown in Fig. 6.12 for two different etching solutions.

  In contrast to that, structuring of the ITO layer via screen-printed Ag metalization grid was identified to be successful. In this case, a less aggressive etching solution was used, so that an uncontrollable under-etching of the ITO layer was avoided. This technique for contact separation is adapted to our IBC SHJ solar cell fabrication in Section 6.3.

6.3 Fabrication and characterization of simplified IBC SHJ solar cells

In this Section, fabricated IBC SHJ solar cells with a simplified process flow are presented. First, an overview of the process flow will be given. Then, process-monitoring lifetime measurements and the solar cell results will be presented and discussed. Afterwards, series resistance losses will be analyzed in detail using resistive network simulations.
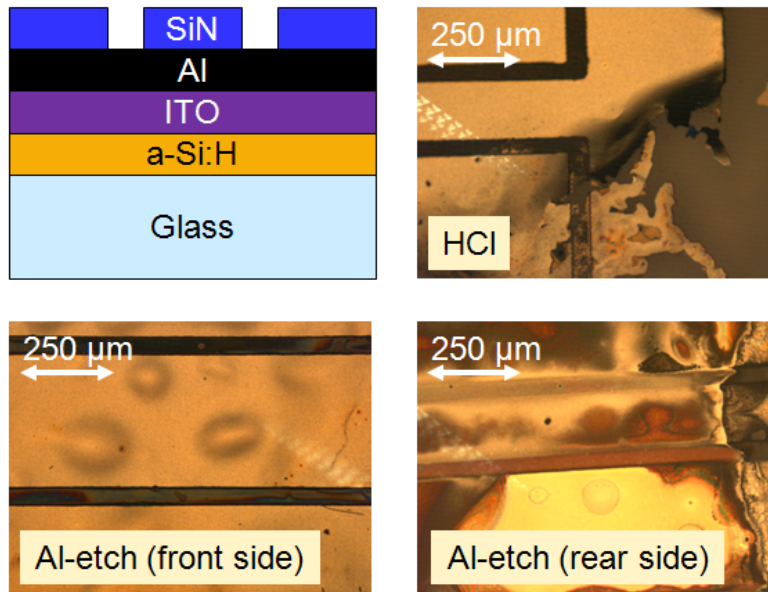
Figure 6.12: Top left: Schematic representation of the test samples for contact separation. Top right: Optical microscope image of a test sample after etching in HCl. The dark lines represent the separated contacts, but due to strong under-etching also the Al fingers are lifted off. Bottom left and right: Front and rear view of a test structure etched with Al-etchant. Also a strong under-etching is observable here.

6.3.1 Simplified solar cell process

A schematic view and a photograph of a fabricated solar cell is shown in Fig. 6.13 For the fabrication we use $3\,\Omega$cm n-type Czochralski-grown silicon wafers with a thickness of $200\,\mu$m. The active cell area is $2 \times 2\,\text{cm}^2$ on a $2.5 \times 2.5\,\text{cm}^2$ substrate. The finger index is $1.6\,$cm. The i/p-a-Si:H emitter fingers are $714\,\mu$m wide, shown in green in Fig. 6.13. The emitter busbar is partially located outside the active cell area of $2 \times 2\,\text{cm}^2$ because of the geometrical layout of the contact needles of the measurement chuck in our J-V tester. The BSF busbar lies completely outside the active cell area. The width of the i/n-a-Si:H BSF region is $886\,\mu$m, whereas the width of the BSF contact opening is only $250\,\mu$m, indicated as red area in Fig. 6.13.

Fig. 6.14 gives an overview of the process steps for the fabrication of the IBC SHJ solar cells. The wafers were damage-etched in a KOH solution and RCA-cleaned. In order to obtain single-side-textured samples, a wet thermal oxide was grown onto the wafer surfaces and subsequently removed from the front side of the wafers by HF. After random-pyramid-texturing in an alkaline solution, the oxide on the rear side was removed by HF (steps 1-3). All wafers were then RCA-cleaned again. Prior to the following a-Si:H depositions, all wafers were dipped in a $1\,\%$ HF solution and subsequently rinsed in deionized water for 1 minute and dried using dry nitrogen.
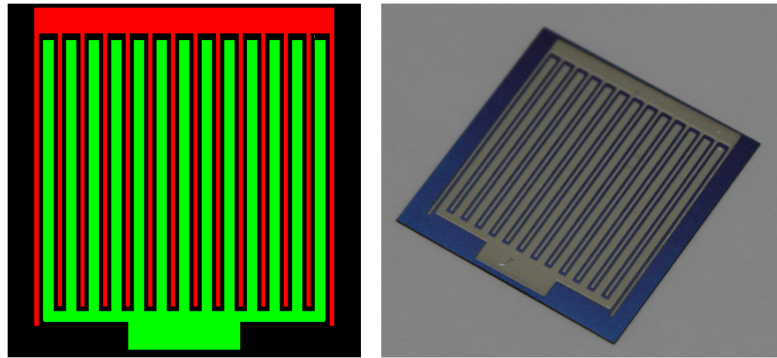
Figure 6.13: On the left hand side a schematic top view of the fabricated SHJ IBC solar cell is shown. On the right hand side a photograph of a fabricated SHJ IBC solar cell is shown.

First, the i-a-Si:H layer on the front side was deposited, followed by the i/n-a-Si:H stack on the rear side. Between the different a-Si:H depositions of one wafer, no extra HF dip was performed (step 4). Afterwards, SiN_x was deposited onto the front and rear side of the wafer (step 5). On the front side the SiN_x acts as anti-reflection coating and on the rear side as capping layer for the following structuring step. PCD measurements were performed to monitor the samples lifetimes at this stage of the production process. Subsequently, the i/n-a-Si:H BSF stack was structured (step 6-8). The full front side was printed with hot-melt wax. On the rear side, the BSF structure was printed. Afterwards, the SiN_x was etched by a 5 % HF solution in those regions, where no hot-melt was printed. Then, the wax was removed with IPA. Subsequently, the i/n-a-Si:H stack was etched with a 50 % concentrated KOH solution at 25 °C for 1 minute in the regions where no SiN_x capping layer is present. Afterwards, the samples were cleaned in HCl as described in Section 6.2.3. Prior to the following i/p-a-Si:H emitter deposition, the samples were dipped in a 1 % HF solution and subsequently rinsed in deionized water for 1 minute and dried using dry nitrogen. Another SiN_x capping layer was deposited onto the rear side of the samples and we measured the lifetime again using PCD (step 9). Afterwards, the i/p-a-Si:H emitter stack was structured (steps 10-12). The full front side of the sample was protected by hot-melt wax. On the rear side, the wax was printed onto the i/p-a-Si:H emitter regions and also 300 μm above the edges of the i/n-a-Si:H BSF regions, because of potential alignment uncertainties. Then, the SiN_x was etched in a 5 % HF solution in those regions, where no wax was printed. Then, the hot-melt wax was removed with IPA. Subsequently, the i/p-a-Si:H stack was etched using a "poly-etch" solution (HNO_3 (65 %) : H_3PO_4 (85 %) : HF (50 %) : H2O at the ratio of 30 : 10 : 1 : 15) for 15 seconds in the regions where no SiN_x capping layer was present. Again, PCD measurements were performed to monitor the lifetimes during the process flow. In a next step, the SiN_x was etched off using a 5 % HF solution (step 13). This process step is necessary to later contact

1.		Oxidation
2.		Oxide removal + texturing
3.		Oxide removal + RCA cleaning
4.		*i/n-a*-Si:H depositions
5.		SiN$_x$ (200°C) + PCD measurement
6.		Inkjet + SiN$_x$ structuring
7.		Inkjet removal
8.		*a*-Si:H structuring + HCl
9.		*p-a*-Si:H + SiN$_x$ + PCD measurement
10.		Inkjet + SiN structuring
11.		Inkjet removal
12.		*p-a*-Si:H structuring + PCD measurement
13.		SiN$_x$ removal
14.		SiN$_x$ deposition
15.		ITO deposition + screen printing
16.		Contact separation
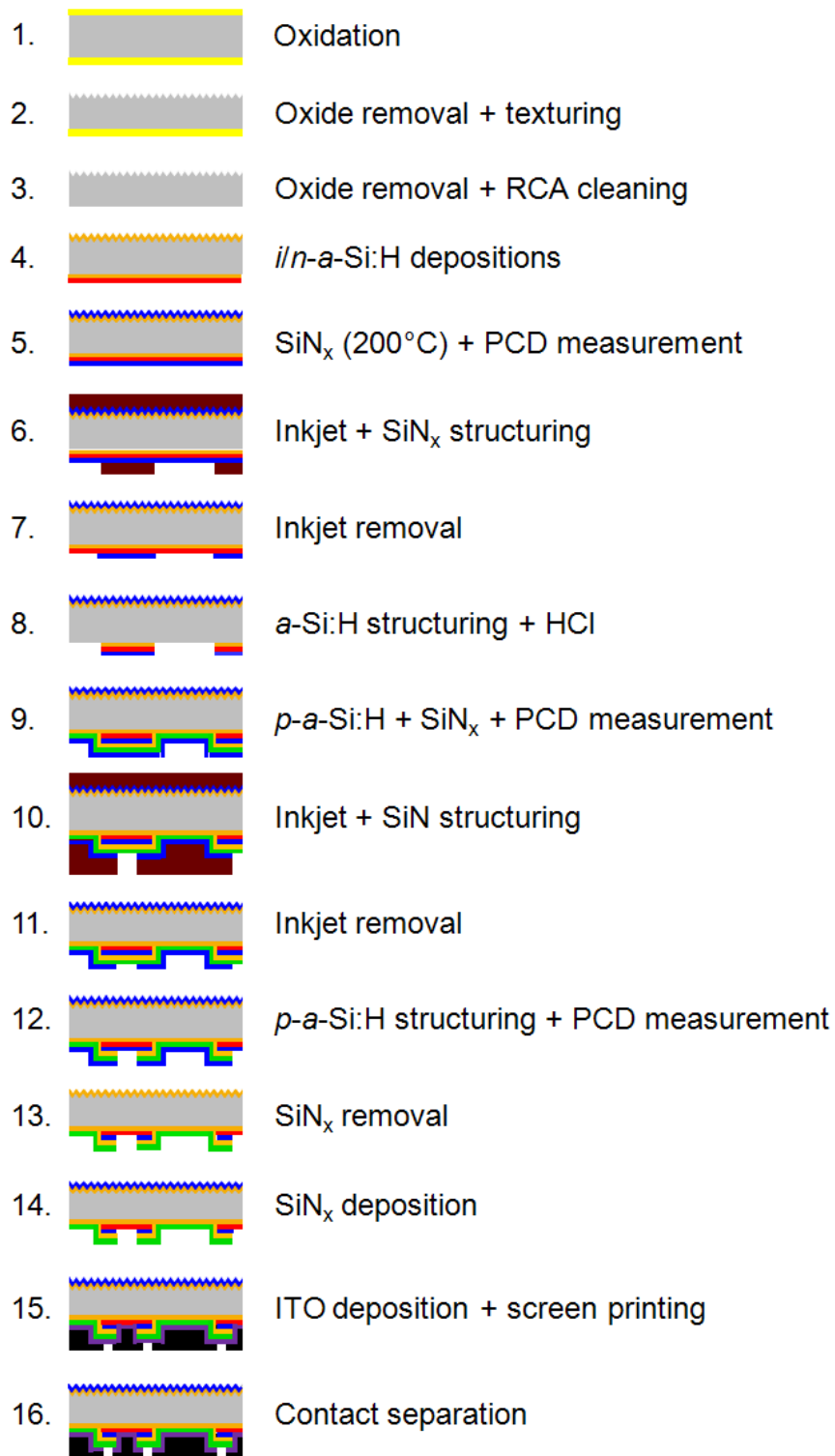
Figure 6.14: Schematic process flow of the fabricated IBC SHJ solar cells.

Estimated J_{SC} = 41 mA/cm²	$V_{OC,impl.}$ [mV]			Ideality factor @ 650 mV			pseudo *FF* [%]	pseudo η [%]	
	700	720	740	1.0	1.4	1.8		24	25
after *i/n-a*-Si:H + capping SiN		724			1.19		83.6		24.8
after *i/p-a*-Si:H + capping SiN		717			1.31		82.1	24.1	
after *i/p-a*-Si:H structuring		716			1.31		81.9	24.0	

Figure 6.15: Implied performance of the IBC SHJ solar cells measured with PCD after different process steps during solar cell fabrication. For the calculation a J_{SC} of $41\,\mathrm{mA/cm^2}$ was assumed.

the i/p-a-Si:H emitter. Because during this HF etching also the front side SiN_x dissolves, a new SiN_x anti-reflection layer was deposited onto the front side of the wafers (step 14). Afterwards, an ITO layer was sputtered onto the full rear side of the solar cell and the interdigitated finger pattern was screen-printed on the rear side (step 15). As a last process step, the ITO between the emitter and BSF fingers was etched off in a 5 % HF solution for 15 seconds. The performances of the finished IBC SHJ solar cells were then measured using the LOANA system. Because the front SiN_x ARC suffered from the various etching steps in HF, we thickened up the SiN_x on the front side in a second deposition and re-measured the $J - V$ curves.

6.3.2 Solar cell results and discussion

To monitor the potential solar cell performance during the fabrication process, PCD measurements were performed after certain process steps. The PCD measurements were performed (i) after the deposition of the i/n-a-Si:H BSF stack plus SiN_x capping layer (step 5), (ii) after the deposition of the i/p-a-Si:H emitter stack plus SiN_x capping layer (step 9), and (iii) after the structuring of the i/p-a-Si:H emitter stack (step 12). The measurement results (avarage values) for 10 solar cells are shown in Fig. 6.15. We observe high implied V_{OC} values of above $715\,\mathrm{mV}$ after all three process steps, indicating that this kind of solar cell is working very well in principle. As has also been shown in Chapter 5 the ideality factor n at MPP increases to a value of $n \approx 1.3$ after the i/p-a-Si:H deposition, which, however, still enables an efficiency of 24.0 %, assuming a realistic J_{SC} value for IBC solar cells of $41\,\mathrm{mA/cm^2}$.

Table 6.2: Performance of two fabricated SHJ IBC solar cells before and after new SiN_x anti-reflection coating.

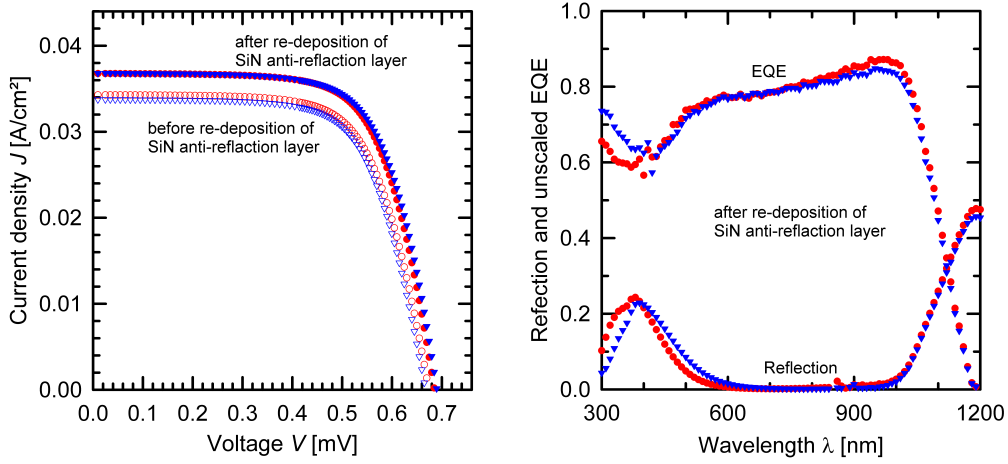|	V_{OC} [mV]	J_{SC} [mA/cm²]	FF [%]	η [%]
Solar cell 1	667.4	33.8	67.9	15.3
Solar cell 1 (new ARC)	689.7	36.8	68.7	17.5
Solar cell 2	674.0	34.3	67.9	15.7
Solar cell 2 (new ARC)	685.3	36.8	68.5	17.3

Figure 6.16: The graph on the left hand side shows *J-V* curves of two fabricated IBC SHJ solar cells before and after the deposition of a new SiN_x anti-reflection coating. The graph on the right hand side shows the EQE and reflection data of two fabricated IBC SHJ solar cells after the deposition of a new SiN_x anti-reflection coating.

The results of two finished solar cells are shown in Table 6.2 and Fig. 6.16. In Table 6.2 the measured cell parameters are summarized directly after the contact separation and also after re-deposition of the front-side SiN_x anti-reflection coating. Surprisingly, the measured V_{OC} values are relatively low compared to the lifetime results of Fig. 6.15. Even after re-deposition of the SiN_x ARC, the V_{OC} does not exceed 690 mV. Also, the J_{SC} is relatively moderate: before the new ARC is deposited, J_{SC} values of about 34 mA/cm² are measured and after re-deposition values of 36.8 mA/cm² are obtained. The moderate V_{OC} values indicate a non-optimal passivation quality. In combination with the moderate J_{SC} values and the low EQE in the short-wavelengths regime (right graph in Fig. 6.16), a decrease of the front side passivation is identified as main issue. Since the passivation quality was still excellent after process step 12, the most likely process steps for the degradation are 13 or 16.

Another limitation of the solar cells is the relatively low *FF* below 70 %, due to high series resistance values. However, a shunt resistance is not visible in the
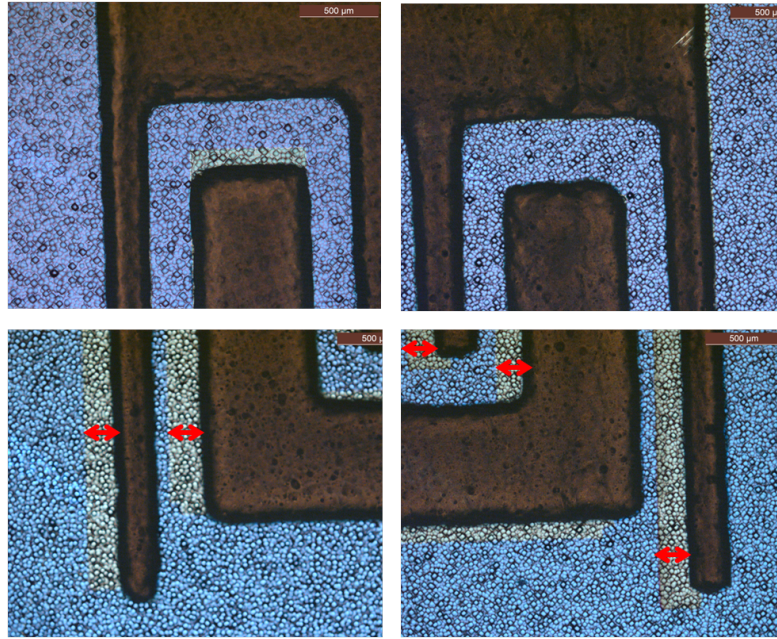
Figure 6.17: Four optical microscope images of the rear side of a fabricated solar cell. Each of the pictures represents one edge of the solar cell, respectively. The red arrows illustrate the tilted metalization grid (brown regions) compared to the contact openings (bright regions).

linearly scaled $J - V$ plot in Fig. 6.16, which proves that the contact separation is sufficient and that the overlap of the emitter and BSF regions does not negatively affect the shunt resistance, in good agreement with our calculation of Section 6.2.1. The high series resistances stem from different sources: (i) the contact resistance through the a-Si:H layers plus a-Si:H/ITO interface, and (ii) the resistance of the low-temperature Ag metalization paste. Another contribution to the high series resistance is (iii) a tilted finger grid on the rear side of the solar cell, i.e. the metal fingers do not align with the a-Si:H emitter and BSF fingers in every position. Optical microscope images of the tilted finger grid are shown in Fig. 6.17. Each of the four images represents one corner of the back side of the solar cell, respectively. The brown areas represent the metal paste. The blue areas are the regions between the emitter and BSF regions, where a layer stack of i/n-a-Si:H/SiN$_x$/i/p-a-Si:H is present. The bright areas in the image are the structured emitter and BSF regions. In the case of a perfect alignment, these areas would not be visible, because they would be covered by the Ag paste. However, in our experimental cells the metal grid is tilted compared to the emitter and BSF openings, indicated by the red arrows in Fig. 6.17. Consequently, the reduced contact area also increases the series resistance. A detailed analysis and simulation of the losses will be presented in the next Section.
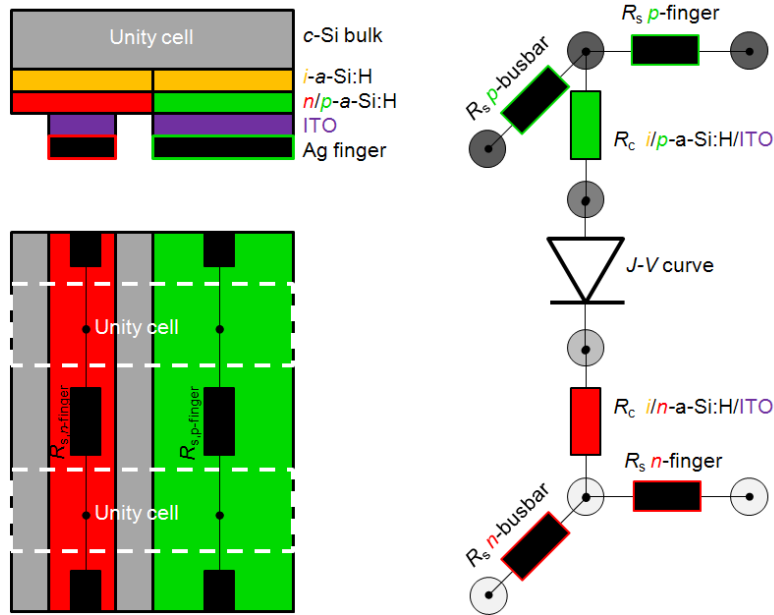
Figure 6.18: Top left: Schematic cross section of a unit cell in the simulation of the IBC SHJ solar cell. Bottom left: Zoomed-in top-view on the simulated solar cell. The green area represents the i/p-a-Si:H emitter finger, and the red area the i/n-a-Si:H BSF finger. The dotted white lines indicate the unity cells, which are connected by series resistances. Right: Representation of one unity cell, consisting of the J-V curve and the contact resistances $R_{c,i/p\text{-}a\text{-Si:H}}$ and $R_{c,i/n\text{-}a\text{-Si:H}}$.

6.3.3 Simulation of series resistance losses

In this Section the origin of the high series resistance of the fabricated IBC SHJ solar cells is examined. For the analysis of the series resistance losses, a network simulation of the entire cell grid and contact resistances applying an in-house developed graphical user interface for LTSpice [142, 143] is performed. Fig. 6.18 shows a schematic representation of the simulated network. The network contains 20×13 nodes; 13 nodes parallel to the busbar, which is the number of emitter and BSF fingers, and 20 parallel to the fingers to assure a sufficient resolution in the potential drop alongside each finger. The simulated cell size is $2 \times 2\,\text{cm}^2$. Therefore, the distance between each node alongside the fingers is $1\,\text{mm}$. The cell pitch is $1.6\,\text{mm}$, which results in 13 emitter and BSF fingers. Each node in the simulation consists of five levels, as indicated on the right-hand side of Fig. 6.18.

The first level represents the emitter finger and busbar grid. The input parameter is the resistivity of the paste ,which was determined to be $14\,\mu\Omega\text{cm}$ in chapter 5. The second level represents the contact resistance through the p-a-Si:H layer and p-a-Si:H/ITO interface, which is $R_{p\text{-}a\text{-Si/ITO}} = 0.42\,\Omega\,\text{cm}^2$, as determined in

Table 6.3: IBC SHJ solar cell simulation results. The corresponding *J*-*V* curves can be seen in Fig. 6.19.

	V_{OC} [mV]	J_{SC} [mA/cm²]	FF [%]	η [%]
Fabricated solar cell	685.3	36.8	68.5	17.3
Simulation "real cell"	686	36.8	68.7	17.4
Simulation "good front side"	716	41	68.4	20.1
Simulation "without R_{c}"	716	41	77.7	22.8
Simulation "without R_{c} and R_{s}"	716	41	81.7	24
Simulation "ideality factor $n = 1$"	716	41	85.1	25.3

Chapter 5. In the third level, the $J - V$ curve of the solar cell is generated. In this simulation, the $J - V$ curve is parameterized by a diode equation:

$$J = J_0 \left(e^{\frac{qV}{n\,kT}} - 1 \right) - J_{\mathrm{ph}} \, , \qquad (6.5)$$

with the elementary charge q, the voltage V, the Boltzmann constant k, and the absolute temperature T. The input parameters are the ideality factor n, the saturation current density J_0, and the photogeneration current density J_{ph}. For the input parameters two different sets of values are used; one set is extracted from the implied $J - V$ curves calculated from the PCD measurements, representing the non-degraded passivation, and one set of values that describes the actual solar cell with degraded front side passivation. Level four represents the contact resistance through the *n*-*a*-Si:H layer and *n*-*a*-Si:H/ITO interface which is $R_{n\text{-}a\text{-Si/ITO}} = 0.1\,\Omega\,\mathrm{cm}^2$, also taken from Chapter 5. The last level represents the BSF finger and busbar grid. The contact points in the simulations are positioned at the same position as the contact needles in the actual $J - V$ measurement, i.e at the middle of the busbars, represented by nodes (1,7) and (20,7).

In the previous Section the PCD measurements of the solar cell precursors showed $V_{\mathrm{OC,impl}}$ values of 716 mV and implied FF of 81.9 %. Assuming a realistic short-circuit current density of $J_{\mathrm{SC}} = 41\,\mathrm{mA/cm^2}$ leads to an implied efficiency of $\eta_{\mathrm{implied}} = 24\,\%$. The corresponding $J - V$ curve is shown in Fig. 6.19 as long-dashed blue line. Now, the resistances are switched on. The resulting solar cell performances are shown in Table 6.3 and Fig. 6.19. The dashed-dotted green curve represents the $J - V$ curve with only considering the resistance of the metalization grid. The short-dashed red curve represents the $J - V$ curve considering the resistance of the metalization grid plus the contact resistance through the *a*-Si:H layers and *a*-Si:H/ITO interfaces. As an approximation, the tilted metalization grid is considered by increasing the base contact resistance by a factor of 1.5. Because of the actual cell design, the tilted finger grid does not influence the emitter contact resistance. In our simulations, the recombination is assumed as measured in the PCD measurement before the metalization. However, the fabricated solar cells
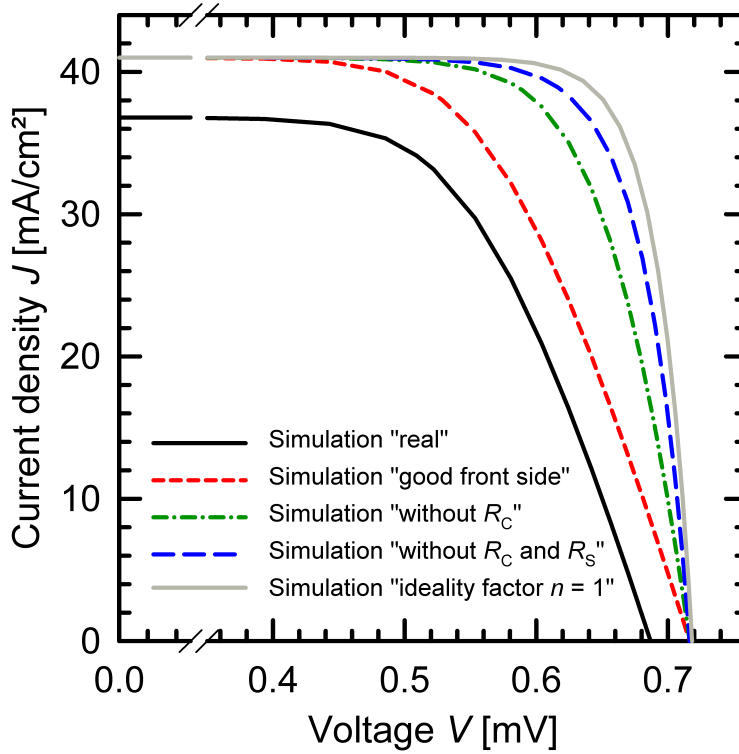
Figure 6.19: Simulated J-V curves. The solid black curve represents the simulation of an actual fabricated IBC SHJ solar cell. The other curves represent simulations, where different loss mechanisms were gradually switched off. The corresponding performance parameters are shown in Table 6.3.

suffer from a poor front side passivation due to a degradation during the contact separation etching, and therefore the V_{OC} and even J_{SC} are reduced. Therefore, in the network simulations the diode input parameters were adjusted to reproduce the actual V_{OC} of our solar cells, i.e. the saturation current density was increased to a value of $5 \times 10^{-11}\,\mathrm{mA/cm^2}$, whereas the ideality factor is kept constant at $n = 1.31$. The resulting performance is shown as solid black line in Fig. 6.19 and Table 6.3. The simulated values fit very well with the experimental results, which proves that the input parameters describe our cell very well. It can be concluded that the efficiency loss due to the different series resistance contributions is dominant. The contact resistance through the a-Si:H layer and a-Si:H/ITO interface was already a main loss mechanism in our both-sides-contacted SHJ solar cells. In the IBC SHJ solar cells, the contact area is even smaller, due to the fact that both contacts are placed on the rear side of the cell, and therefore the resulting series resistance loss is larger. Also, the rear grid reduces the fill factor, and thus the efficiency significantly, which is due to the rather low conductivity of the low-temperature

Ag paste and also to the position of the contact points that are only located on the middle of the busbars.

6.4 Chapter conclusions

In this Chapter, IBC SHJ solar cells were presented with efficiencies of 20.2 %. However, the fabrication process of this particular cell type was very complicated and required 50 process steps. As a major challenge the structuring techniques for the *a*-Si:H emitter and BSF layers on the back side were identified. In general, laser structuring techniques were shown to degrade the surface passivation quality. We have shown however, that laser-ablation can be applied in the case of non-overlapping laser spots and post annealing treatment with a full regain of the passivation quality. Wet-chemical structuring techniques were shown to have the potential of damage-free ablation of the *a*-Si:H layers, however, they require different capping layers and the deposition and removal of etching masks. The high contact resistances through the *a*-Si:H layer plus *a*-Si:H/ITO interface proved a challenge, because of the reduced contact area compared to two-sides contacted solar cells. This seems to be a general issue, because after publication of our results for the contact resistances, other groups found comparable values also [144, 123]. However, in conclusion, our results have demonstrated that the efficiency potential of IBC SHJ solar cells is very high (>24 %) and that simplified process sequences are possible to implement. Using a process consisting of only 16 steps we have achieved a remarkable efficiency of 17.5 %, mainly limited by series resistance efffects.

7

Conclusions

In this thesis, we have investigated the surface passivation quality of thin i-a-Si:H films in dependence of annealing and H_2-plasma post treatment steps. We have found that with an optimized PECVD deposition process no additional post treatment is necessary to obtain very low surface recombination velocities. We have demonstrated the excellent level of surface passivation of our a-Si:H layers in SHJ solar cells with open-circuit voltages in excess of $730\,\mathrm{mV}$. Furthermore, we have shown for the first time that increasing the hydrogen dilution during the PECVD process is beneficial for the passivation of $(1\,1\,1)$-oriented surfaces, whereas the opposite holds true for $(1\,0\,0)$-oriented substrates, which is of major importance for textured wafer surfaces on the front side of solar cells, where the $(1\,0\,0)$ surface changes to pyramids with $(1\,1\,1)$-oriented facets. Moreover, we have shown that the effective doping of our p-a-Si:H layers is maximal for a gas phase doping with boron of $4000\,\mathrm{ppm}$ and of our n-a-Si:H layers for a gas phase doping with phosphorus of $2000\,\mathrm{ppm}$ during the PECVD deposition, and that the doping level is proportional to the V_{OC} of finished solar cells.

We have investigated the optical properties of our a-Si:H and ITO layers, whereby optical constants were determined via ellipsometry. We have performed ray-tracing simulations to quantify the absorption losses in the different layers and have found a very good agreement to experimentally obtained J_{SC} values of our finished SHJ solar cells. We have extracted absorption losses of $0.02\,\mathrm{mA/cm^2 \cdot nm}$ for our ITO layer, and $0.10\,\mathrm{mA/cm^2 \cdot nm}$ and $0.11\,\mathrm{mA/cm^2 \cdot nm}$ for our i-a-Si:H and p-a-Si:H layers, respectively.

We have introduced a novel experimental approach to measure the resistance losses across the a-Si:H/c-Si and a-Si:H/ITO interfaces, which enables the quantification of these losses for the first time. For our best a-Si:H and ITO recipes we have determined values for $R_{p\text{-}a\text{-}\mathrm{Si/ITO}}$ of $0.42\,\Omega\,\mathrm{cm}^2$ and for $R_{n\text{-}a\text{-}\mathrm{Si/ITO}}$ below $0.1\,\Omega\,\mathrm{cm}^2$.

Based on our optimization studies, we have fabricated bifacial screen-printed SHJ solar cells featuring a very high open-circuit voltage of $V_{\mathrm{OC}} = 733\,\mathrm{mV}$, demonstrating the excellent level of interface passivation. The efficiency of $20.2\,\%$ was

limited by the relatively low short-circuit current density of $37.1\,\mathrm{mA/cm^2}$ and a fill factor of $76\,\%$. We have performed an in-depth analysis of the series resistance, shading and absorption losses of our SHJ solar cells. Absolute efficiency losses of $2 - 2.5\,\%_{\mathrm{abs}}$ stem from series resistance contributions, including $1.3\,\%_{\mathrm{abs}}$ from the front electrode and $0.7 - 1.2\,\%_{\mathrm{abs}}$ from the transport through the a-Si:H layers and a-Si:H/ITO interface. The efficiency losses due to absorption in the a-Si:H and ITO layers are $1.4\,\%_{\mathrm{abs}}$. The shading losses of the actual front metalization grid contributes with $1.3\,\%_{\mathrm{abs}}$ efficiency loss. Optimizing the finger aspect ratio and paste conductivity of the front metalization grid would strongly increase the efficiency of our still technologically-limited cell performance.

As a second type of solar cell with increased efficiency potential, we have developed IBC SHJ cells and demonstrated an efficiency of $20.2\,\%$, which was a world record for this cell type at the time of publication. However, the fabrication process of this particular cell type was very complex and required in total 50 process steps. Therefore, we have investigated alternative process flows and fabrication techniques to simplify the process. For the first time, laser techniques were investigated for the structuring of a-Si:H layers in IBC SHJ solar cells and were demonstrated to be potentially applicable for individual processes, but require compromises in terms of device design and performance. As a second structuring technique we examined wet-chemical structuring based on inkjet technology and demonstrated the potential of damage-free ablation of a-Si:H layers. In addition, we have introduced a novel technique for the contact separation on the rear side of the solar cell via a screen-printed interdigitated Ag finger pattern. Using a process consisting of only 16 steps we have presented solar cells with a remarkable measured pseudo efficiency of $24.0\,\%$ and with actually achieved efficiencies of only $17.5\,\%$, where the V_{OC} and J_{SC} values were, however, limited only by technological aspects. Using resistive network simulations, we have shown that very high *FF* losses stem from the contact resistance ($9.3\,\%_{\mathrm{abs}}$) and from the resistance in the metal fingers ($4.0\,\%_{\mathrm{abs}}$). The series resistance losses in the metal grid can be avoided by using thicker fingers. However, the high contact resistance through the a-Si:H/ITO interface proved to be a more general challenge, because of the reduced contact area compared to two-sides-contacted solar cells. Therefore, decreasing the contact resistance between the a-Si:H/c-Si and a-Si:H/ITO interfaces is considered to be the most important approach for further optimization.

References

[1] R. Brendel, T. Dullweber, R. Gogolin, H. Hannebauer, N.-P. N.-P. Harder, J. Hensen, S. Kajari-Schroeder, J. H. R. Peibst, R. andPetermann, U. Römer, J. Schmidt, H. Schulte-Huxel, and Steckenreiter V. Recent progress and options for future crystalline silicon solar cells. *European Photovoltaic Solar Energy Conference and Exhibition*, 28th:676–690, 2013.

[2] S.W. Glunz, R. Preu, and D. Biro. *Chapter 1.16 in "Comprehensive renewable energy", Vol. 1.* Elsevier, 2012.

[3] A. Metz, D. Adler, S. Bagus, H. Blanke, M. Bothar, E. Brouwer, S. Dauwe, K. Dressler, R. Droessler, T. Droste, M. Fiedler, Y. Gassenbauer, T. Grahl, N. Hermert, W. Kuzminski, A. Lachowicz, T. Lauinger, N. Lenck, M. Manole, M. Martini, R. Messmer, C. Meyer, J. Moschner, C. Ramspeck, P. Roth, R. Schönfelder, B. Schum, J. Sticksela, K. Vaas, M. Volk, and K. Wangemann. Industrial high performance crystalline silicon solar cells and modules based on rear surface passivation technology. *Solar Energy Materials and Solar Cells*, 120, Part A:417, 2014.

[4] International technology roadmap for photovoltaic. (ITRPV): Results 2012, (semi PVGroup, 2013), Fig. 34.

[5] P. J. Verlinden, W. Deng, Y. Zhang, X. Yang, Z. Xiong, J. Xu, P. Shu, Y. Quan, J. Sheng, Y. Chen, S. Zhang, J. Bao, F. Ping, Y. Zhang, and Z. Feng. Strategy, development and mass-production of high-efficiency crystalline silicon pv modules. *Proc. 6th World Conference on Photovoltaic Energy Conversion*, pages 485–488, 2014.

[6] T. Weber, G. Fischer, A. Oehlke, C. Kusterer, K. Strauch, R. Schiepe, M. Mühlbauer, M. Müller, F. Wolny, R. Köhler, G. Grupp-Mueller, E. E. Schneiderlöchner, K. H. Stegemann, and H. Neuhaus. High volume

pilot production of high efficiency perc solar cells-analysis based on device simulation. *Energy Procedia*, 38:474, 2013.

[7] A. Richter, M. Hermle, and S.W. Glunz. Reassessment of the limiting efficiency for crystalline silicon solar cells. *IEEE Journal of Photovoltaics*, 3 (4):1184–1191, 2013.

[8] H. Hannebauer, M. Sommerfeld, J. Müller, T. Dullweber, and R. Brendel. Analysis of the emitter saturation current density of industrial type silver screen-printed front contacts. *European Photovoltaic Solar Energy Conference, Frankfurt, Germany*, 27th:2BV.5.10, 2012.

[9] T. Dullweber, H. Hannebauer, U. Baumann, T. Falcon, K. Bothe, S. Steckemetz, and R. Brendel. Fine-line printed 5 busbar perc solar cells with conversion efficiencies beyond 21*European PV Solar Energy Conference*, 29th, 2014.

[10] M. D. Lammert and R. J. Schwartz. The interdigitated back contact solar cell: a silicon solar cell for use in concentrated sunlight. *IEEE Trans. Electron Dev.*, 24:337–342, 1977.

[11] R.M. Swanson. Approaching the 29% limit efficiency of silicon solar cells. *Proc. 31st IEEE PVSC, Lake Buena Vista*, pages 889–894, 2005.

[12] K. Masuko, M. Shigematsu, T. Hashiguchi, D. Fujishima, M. Kai, N. Yoshimura, T. Yamaguchi, Y. Ichihashi, T. Mishima, N. Matsubara, T. Yamanishi, T. Takahama, M. Taguchi, E. Maruyama, and S. Okamoto. Achievement of more than 25.6% conversion efficiency with crystalline silicon heterojunction solar cell. *IEEE Journal of Photovoltaics*, 4(6):1433–1435, 2014.

[13] M. Tanaka, M. Taguchi, T. Matsuyama, T. T. Sawada, S. Tsuda, S. Nakano, H. Hanafusa, and Kuwano Y. Development of new a-si/c-si heterojunction solar cells:acj-hit (artificially constructed junction-heterojunction with intrinsic thin layer). *Jpn. J. Appl. Phys.*, 31:3518–3522, 1992.

[14] S. de Wolf, A. Descoeudres, Z. C. Holman, and C. Ballif. High-efficiency silicon heterojunction solar cells: A review. *Green*, 2:7–24, 2012.

[15] D. Baetzner, Y. Andrault, L. Andreetta, A. Buechel, W. Frammelsberger, C. Guerin, N. Holm, D. Lachenal, J. Meixenberger, P. Papet, B. Rau, B. Strahm, G. Wahli, and F. Wuensch. Characterisation of over 21developed at roth & rau switzerland. In *Proceedings of the 26th EU PVSEC, Hamburg, Germany, 1073-1075*, 2011.

[16] (2013, sept. 23). panasonic data sheet. [online]. available: `http://www.aeetenergy.com/pdf/VBHNxxxSE10_DE.pdf`.

[17] M. A. Green, K. Emery, Y Hishikawa, W. Warta, and E. D. Dunlop. Solar cell efficiency table (version 43). *Progress in Photovoltaics: Research and Applications*, 22:1–9, 2014.

[18] A. Yano, S. Tohoda, K. Matsuyama, Y. Nakamura, T. Nishiwaki, K. Fujita, M. Taguchi, and E. Maruyama. 24.7 % record efficiency hit solar cell on thin silicon wafer. In *Proc. 28th Eur. Photovoltaic Solar Energy Conf. Exhib., Paris, France, pp.748-751*, 2013.

[19] L. Korte, T. F. Schulze, C. Leendertz, M. Schmidt, and B. Rech. Band alignment at amorphous/crystalline silicon hetero-interfaces. In *Symposium A - Amorphous and Polycrystalline Thin-Film Silicon Science and Technology of MRS Proceedings, Vol, 1321*, 2011.

[20] F.A. Rubinelli. Amorphous-crystalline silicon anisotype heterojunctions: Built-in potential, its distribution and depletion widths. *Solid-State Electronics*, 30(3):345–351, 1987.

[21] T. F. Schulze, L. Korte, E. Conrad, M. Schmidt, and B. Rech. Electrical transport mechanisms in a-si:h/c-si heterojunction solar cells. *J. Appl. Phys.*, 107:023711–1–023711–13, 2010.

[22] Z. C. Holman, A. Descoeudres, L. Barraud, F. Zicarelli Fernandez, J. P. Seif, S. De Wolf, and C. Ballif. Current losses at the front of silicon heterojunction solar cells. *IEEE J. Photovoltaics*, 2:7–15, 2012.

[23] R. M. Young and W. D. Partlow. Amorphous silicon, amorphous carbon and amorphous silicon carbide deposited by remote chemical vapor deposition. *Thin solid films*, 213:170, 1992.

[24] F. W. Smith. Optical probabilities and local atomic bonding in hydrogenated amorphous carbon and silicon-carbon alloys. *Mat. Sci. Forum*, 52:323, 1990.

[25] W. Favre, J. Coignus, N. Nguyen, R. Lachaume, R. Cabal, and Munoz D. Influence of the transparent conductive oxide layer deposition step on electrical properties of silicon heterojunction solar cells. *Appl. Phys. Lett.*, 102:181118, 2013.

[26] B. Demaurex, S. De Wolf, A. Descoeudres, Z.C. Holman, and C. Ballif. Damage at hydrogenated amorphous/crystalline silicon interfaces by indium tin oxide overlayer sputtering. *Appl. Phys. Lett.*, 101:171604, 2012.

[27] R. A. Street. *Hydrogenated Amorphous Silicon*. Cambridge University Press, 1991.

[28] K. Tanaka, E. Maruyama, T. Shimada, and H. Okamoto. *Amorphous Silicon*. John Wiley & Sons, 1999.

References

[29] W. H. Zachariasen. The atomic arrangement in glass. *J. Am. Chem. Soc.*, 54:3841, 1932.

[30] D. E. Polk. Structural model for amorphous silicon and germanium. *J. Non-Cryst. Solids*, 5:365, 1971.

[31] W. Schulke. Structural investigation of hydrogenated amorphous silicon by x-ray diffraction. *Philos. Mag. B*, 43:451, 1981.

[32] J. Fortner and J. S. Lannin. Radial distribution functions of amorphous silicon. *Phys. Rev. B*, 39:5527(R), 1989.

[33] J. C. Phillips. Topology of covalent non-crystalline solids i: Short-range order in chalcogenide alloys. *J. Non-Cryst. Solids*, 34:153, 1979.

[34] P. W. Anderson. Absence of diffusion in certain random lattices. *Physical Review*, 109:1492–1505, 1958.

[35] C. M. Soukoulis, M. H. Cohen, and E. N. Economou. Exponential band tails in random systems. *Physical Review Letters*, 53:616–619, 1984.

[36] N. F. Mott and E. A. Davis. *Electronic processes in non-crystalline materials.* Oxford University Press, 1979.

[37] L. Korte. *Die elektronische Struktur des amorph-kristallinen Silizium-Heterostruktur-Kontakts.* PhD thesis, Fachbereich Physik der Philipps-Universität Marburg, 2006.

[38] P. G. LeComber and W. E. Spear. Electronic transport in amorphous silicon films. *Phys. Rev. Lett.*, 25:509, 1970.

[39] R. A. Street, J. Kakalios, and M. Hack. The electron drift mobility in doped amorphous silicon. *Phys. Rev. B*, 38:5603, 1988.

[40] R. A. Street, C. C. Tsai, M. Stutzmann, and J. Kakalios. The role of dangling bonds in the transport and recombination of a-si:h alloys. *Philos. Mag. B*, 56:289, 1987.

[41] J. Tauc. *Optical Properties of Solids.* 1972.

[42] R. C. Ross and J. Jaklik. Plasma polymerization and deposition of amorphous hydrogenated silicon from rf and dc silane plasmas. *J. Appl. Phys.*, 55:3785, 1984.

[43] H. Meiling, W. Lenting, J. Bezemer, and W. F. van der Weg. The influence of electrode shape and hydrogen dilution of sih4 on the optical properties of glow-discharge hydrogenated amorphous silicon. *Philos. Mag. B*, 62:19–28, 1990.

112

[44] A. J. M. Berntsen, W. F. van der Weg, P. A. Stolk, and F. W. Saris. Separating the effects of hydrogen and bond-angle variation on the amorphous-silicon band gap. *Phys. Rev. B*, 48:14656, 1993.

[45] N. Maley and J. S. Lannin. Influence of hydrogen on vibrational and optical properties of a-si1-xhx alloys. *Phys. Rev. B*, 36:1146, 1987.

[46] C. C. Street, R. A. andTsai, J. Kakalios, and W. B. Jackson. Hydrogen diffusion in amorphous silicon. *Philos. Mag. B*, 56:305, 1987.

[47] K. Tanaka, E. Maruyama, T. Shimada, and H. Okamoto. *Amorphous Silicon.* John Wiley & Sons, 1999, p.60.

[48] K. Tanaka, E. Maruyama, T. Shimada, and H. Okamoto. *Amorphous Silicon.* John Wiley & Sons, 1999, p.65.

[49] R. A. Street. The density of states in hydrogenated amorphous silicon. In *Proc. SPIE 0763, Physics of Amorphous Semiconductor Devices, 10*, 1987.

[50] L. Korte, E. Conrad, H. Angermann, R. Stangl, and M. Schmidt. Advances in a-si:h/c-si heterojunction solar cell fabrication and characterization. *Solar Energy Materials and Solar Cells*, 93:905–910, 2009.

[51] S. de Wolf and M. Kondo. Boron-doped a-si:h/c-si interface passivation: degradation mechanism. *Appl. Phys. Lett.*, 91:112109, 2007.

[52] H. Curtins, N. Wyrsch, and A. V. Shah. High-rate deposition of amorphous hydrogenated silicon: effect of plasma excitation frequency. *Electron. Lett.*, 23:228, 1987.

[53] A. H. Mahan, J. Carapella, B. P. Nelson, R. S. Crandall, and I. Balberg. Deposition of device quality, low h content amorphous silicon. *J. Appl. Phys.*, 69:6728, 1991.

[54] P. R. i Cabarrocas. Plasma enhanced chemical vapor deposition of amorphous, polymorphous and microcrystalline silicon films. *Journal of Non-Crystalline Solids*, 266-269 (Part 1):31–37, 2000.

[55] W. M. M. Kessels, A. H. M. Smets, D. C. Marra, E. S. E. S. Aydil, D. C. Schram, and M. C. M. van de Sanden. On the growth mechanism of a-si:h. *Thin Solid Films*, 383(1-2):154–160, 2001.

[56] J. Robertson. Deposition mechanism of hydrogenated amorphous silicon. *J. Appl. Phys.*, 87:2608–2617, 2000.

[57] P. R. i Cabarrocas, Y. Bouizem, and Theye M. L. Defect density and hydrogen bonding in hydrogenated amorphous silicon as functions of substrate temperature and deposition rate. *Philosophical Magazine B*, 65(5):1025–1040, 1992.

References

[58] G. Ganguly and A. Matsuda. Defect formation during growth of hydrogenated amorphous silicon. *Phys. Rev. B*, 47:3661–3670, 1993.

[59] M. J. Kushner. A model for the discharge kinetics and plasma chemistry during plasma enhanced chemical vapor deposition of amorphous silicon. *J. Appl. Phys.*, 63:2532, 1988.

[60] G. J. Nienhuis, W. J. Goedheer, E. A. G. Hamers, W. G. J. H. M. van Sark, and J. Bezemer. A self-consistent fluid model for radio-frequency discharges in sih4-h2 compared to experiments. *J. Appl. Phys.*, 82:2060, 1997.

[61] J. Perrin, O. Leroy, and M. C. Bordage. Cross-sections, rate constants and transport coefficients in silane plasma chemistry. *Contrib. Plasma Phys.*, 36:3–49, 1996.

[62] A. Gallagher and J. Scott. Gas and surface processes leading to hydrogenated amorphous silicon films. *Solar Cells*, 21(1-4):147–152, 1987.

[63] R. Robertson and A. Gallagher. Mono- and disilicon radicals in silane and silaneargon dc discharges. *J.Appl. Phys.*, 59(10):3402–3411, 1986.

[64] A. Matsuda, K. Nomoto, Y. Takeuchi, A. Suzuki, A. Yuuki, and J. Perrin. Temperature dependence of the sticking and loss probabilities of silyl radicals on hydrogenated amorphous silicon. *Surface Science*, 227(1-2):50–56, 1990.

[65] R. Robertson and A. Gallagher. Reaction mechanism and kinetics of silane pyrolysis on a hydrogenated amorphous silicon surface. *J. Chem. Phys*, 85(6):3623–3630, 1986.

[66] A. Matsuda. Plasma and surface reactions for obtaining low defect density amorphous silicon at high growth rates. *J. Vac. Sci. Technol. A*, 16:365–368, 1998.

[67] H. Fujiwara and M. Kondo. Impact of epitaxial growth at the heterointerface of a-si/c-si solar cells. *Appl. Phys. Lett.*, 90:013503, 2007.

[68] U.K. Das, M.Z. Burrows, M. Lu, S. Bowden, and R.W. Birkmire. Surface passivatrion and heterojunction cells on (1 0 0) and (1 1 1) wafers using dc and rf plasma deposited si:h thin films. *Applied Physics Letters*, 92:063504, 2008.

[69] R. Gogolin, R. Ferre, M. Turcu, and N.-P. Harder. Silicon heterojunction solar cells: Influence of h2-dilution on cell performance. *Sol. Energ. Mat. Sol. Cells*, 106:47–50, 2012.

[70] S. de Wolf and M. Kondo. Abruptness of a-si:h/c-si interface revealed by carrier lifetime measurements. *Appl. Phys. Lett.*, 90:042111, 2007.

[71] R. Tsu, J. Gonzalez-Hernandez, S. S. Chao, S. C. Lee, and K. Tanaka. Critical volume fraction of crystallinity for conductivity percolation in phosphorus doped si:f:h alloys. *Appl. Phys. Lett.*, 40:534, 1982.

[72] C. Droz, E. Vallat-Sauvain, J. Bailat, L. Feitknecht, J. Meier, and A. Shah. Relationship between raman crystallinity and open-circuit voltage in microcrystalline silicon solar cells. *Solar Energy Materials and Solar Cells*, 81:61–71, 2004.

[73] W. E. Spear and P. G LeComber. Substitutional doping of amorphous silicon. *Solid State Commun.*, 17:1193, 1975.

[74] M. Stutzmann, D.K. Biegelsen, and Street. R.A. Detailed investigation of doping in hydrogenated amorphous silicon and germanium. *Physical Review B*, 35:5666–701, 1987.

[75] W. E. Spear and P. G. LeComber. Doped amorphous semiconductors. *Adv. Phys*, 26:811, 1977.

[76] M. A. Green. "review of semiconductor properties," in solar cells: Operating principles, technology, and system applications. *Englewood Cliffs, NJ, USA: Prentice-Hall*, 1992.

[77] J. Perrin, Y. Takeda, N. Hirano, Y. Takeuchi, and A. Matsuda. Sticking and recombination of the sih3 radical on hydrogenated amorphous silicon: The catalytic effect of diborane. *Surface Science*, 210(1-2):114–128, 1989.

[78] D. L. Staebler and C. R. Wronski. Reversible conductivity changes in discharge-produced amorphous si. *Appl. Phys. Lett.*, 31:292, 1977.

[79] D. L. Staebler and C. R. Wronski. Optically induced conductivity changes in discharge-produced hydrogenated amorphous silicon. *J. Appl. Phys.*, 51:3262, 1980.

[80] M. Stutzmann, W. B. Jackson, and C. C. Tsai. Light-induced metastable defects in hydrogenated amorphous silicon: A systematic study. *Phys. Rev. B*, 32:23, 1985.

[81] H. M. Branz. Hydrogen collision model of light-induced metastability in hydrogenated amorphous silicon. *Solid State Commun.*, 105:387–391, 1998.

[82] J. Clemens. Characterization of a-si/tco-contacts for silicon based heterojunction solar cells. Master's thesis, Georg-August-University Goettingen, 2011.

[83] J. Matthijn Dekkers, Guus Rijnders, and Dave H. A Blank. Role of sn doping in in2o3 thin films on polymer substrates by pulsed-laser deposition at room temperature. *Applied Physics Letters*, 88(15):151908, 2006.

References

[84] H.-N. Cui, V. Teixeira, L.-J. Meng, R. Martins, and E. Fortunato. Influence of oxygen/argon pressure ratio on the morphology, optical and electrical properties of ito thin films deposited at room temperature. *Vacuum*, 82:1507–1511, 2008.

[85] (2014, mar. 11). pv-tools. hamelin, germany. [online]. available: `http://www.pv-tools.de/products/loana-system/loana-start.html`.

[86] M. A. Green. "efficiency limits, losses, and measurement," in solar cells: Operating principles, technology, and system applications. *Englewood Cliffs, NJ, USA: Prentice-Hall*, 1992.

[87] R.A. Sinton and A. Cuevas. Contactless determination of current-voltage characteristics and minority carrier lifetimes in semiconductors from quasi-steady-state photoconductance data. *Appl. Phys. Lett.*, 69:2510–2512, 1996.

[88] J.M. Dorkel and P. Leturcq. Carrier mobilities in silicon semi-emirically related to temperature, doping and injection-level. *Solid-State Electron.*, 24:821–825, 1981.

[89] H. Angermann, T. F. Schulze, E. Conrad, J. Rappich, L. Korte, and M. Schmidt. Cleaning and passivation of structured n-type si substrates: Preparation and interface properties of a-si:h/c-si hetero solar cells. In *Proc.of the 23rd Eur. PVSEC*, 2008.

[90] W. Kern and D.A. Puotinen. Cleaning solutions based on hydrogen peroxide for use in silicon semiconductor technology. *RCA Review*, 31:187, 1970.

[91] T. F. Schulze, H. N. Beushausen, C. Leendertz, A. Dobrich, B. Rech, and L. Korte. Interplay of amorphous silicon disorder and hydrogen content with interface defects in amorphous/crystalline silicon heterojunctions. *Applied Physics Letters*, 96:252102, 2010.

[92] A. Descoeudres, L. Barraud, S. De Wolf, B. Strahm, D. Lachenal, C. Guérin, Z.C. Holman, F. Zicarelli, B. Demaurex, J. Seif, J. Holovsky, and C. Ballif. Improved amorphous/crystalline silicon interface passivation by hydrogen plasma treatment. *Appl. Phys.Lett.*, 99:123506–123506–3, 2011.

[93] S. de Wolf and M. Kondo. Nature of doped a-si:h/c-si interface recombination. *J. Appl. Phys.*, 105:103707, 2009.

[94] W. E. Spear and P.G. LeComber. Electronic properties of substitutionally doped amorphous si and ge. *Phil. Mag.*, 33:935–949, 1976.

[95] W. E. Spear and H. L. Steemers. The reversal of drifting excess carriers in an amorphous silicon junction. *Phil. Mag. B*, 47:L107–L112, 1983.

[96] J. Kakalios. Microscopic mobility in hydrogenated amorphous silicon. *Phil. Mag. Lett.*, 55:129–134, 1987.

[97] A. Descouedres, L. Barraud, R. Bartlome, G. Choong, S. De Wolf, F. Zicarelli, and C. Ballif. The silane depletion fraction as an indicator for the amorphous/crystalline silicon interface passivation quality. *Applied Physics Letters*, 97:183505, 2010.

[98] U.K. Das, M.Z. Burrows, M. Lu, S. Bowden, and R.W. Birkmire. Surface passivation quality and structure of thin a-si:h layers on n-type crystalline si (1 0 0) and (1 1 1) wafers. In *22th European Photovoltaic Solar Energy Conference and Exhibition, Milan, Italy*, 2007.

[99] N. Mingirulli, J. Haschke, R. Gogolin, R. Ferre, T.F. Schulze, J. Duesterhoeft, N.-P. Harder, L. Korte, and B. Rech. Efficient interdigitated back-contacted silicon heterojunction solar cells. *Phys. Stat. Sol. RRL*, 5 (Issue 4):159–161, 2011.

[100] R.A. Sinton, A. Cuevas, and M. Stuckings. Quasi-steady-state photoconductance, a new method for solar cell material and device characterization. In *Proceedings of the 25th IEEE Photovoltaics Specialist Conference, Washington, D.C., USA, pp. 457-460*, 1996.

[101] T.H. Wang, Q. Wang, E. Iwaniczko, M.R. Page, D.H. Levi, Y. Yan, C.W. Teplin, Y. Xu, X.Z. Wu, and H.M. Branz. Heterojunction silicon solar cells with high open-circuit voltages by interface optimization. In *19th European Photovoltaic Solar Energy Conference, Paris, France, pp. 1296-1299*, 2004.

[102] C. Ross, Y. Mai, R. Carius, and F. Finger. Use of seed layers for structure, optical, and electronic transport measurements on microcrystalline silicon on glass. *Progress in Photovoltaics: Research and Applications*, 19:715–723, 2011.

[103] S. Olibet. *Properties of Interface of Amorphous/Crystalline Silicon Heterojunction*. PhD thesis, pp. 142-143, 2009.

[104] K. Tanaka, E. Maruyama, T. Shimada, and H. Okamoto. *Amorphous Silicon.* John Wiley & Sons, 1999, p.70.

[105] K. Levenberg. A method for the solution of certain non-linear problems in least squares. *Quarterly Journal of Applied Mathmatics*, 2:164–168, 1944.

[106] G.E. Jellison Jr. and F.A. Modine. Parameterization of optical functions of amorphous materials in the interband region. *Appl. Phys. Lett.*, 69:2137, 1996.

References

[107] A.S. Ferlauto, G.M. Ferreira, J.M. Pearce, C.R. Wronski, R.W. Collins, X. Deng, and G. Ganguly. Analytical model for the optical functions of amorphous semiconductors from the near-infrared to ultraviolet: Applications in thin film photovoltaics. *J. Appl. Phys.*, 92:2424, 2002.

[108] E. Palik. *Handbook of Optical Constants of Solids Vol I*. Academic Press, Orlando, 1985.

[109] Z. Holman, M. Filipic, A. Descoeudres, S. De Wolf, F. Smole, M. Topic, and C. Ballif. Infrared light management in high-efficiency silicon heterojunction and rear-passivated solar cells. *Journal of Applied Physics*, 113(1):013107, 2013.

[110] H. Nagel. *Analyse und Reduktion der optischen und elektrischen Verluste in multikristallinen Silizium-Solarzellen*. PhD thesis, Universitaet Hannover, 2002.

[111] R. Brendel. Sunrays: a versatile ray trracing program for the photovoltaic community. In *12th european photovoltaic solar energy conference*, 1994.

[112] M. Green. Self-consistent optical parameters of intrinsic silicon at 300k including temperature coefficients. *Solar Energy Materials & Solar Cells*, 92:1305–1310, 2008.

[113] J. L. Hernandez, D. Adachi, D. Schroos, N. Valckx, N. Menou, T. T. Uto, M. Hino, M. Kanematsu, H. Kawasaki, R. Mishima, K. Nakano, H. Uzu, T. Terashita, K. Yoshikawa, T. Kuchiyama, M. Hiraishi, N. Nakanishi, M. Yoshimi, and K. Yamamoto. High efficiency copper electroplated heterojunction solar cells and modules - the path towards 25 In *Proc. 28th Eur. Photovoltaic Solar Energy Conf. Exhib., Paris, France, pp. 741-743*, 2013.

[114] T. Kinoshita, D. Fujishima, A. Yano, A. Ogane, S. Tohoda, K. Matsuyama, Y. Nakamura, N. Tokuoka, H. Kanno, H. Sakata, M. Taguchi, and E. Maruyama. The approaches for high efficiency hit solar cell with very thin $(100\,\mu\text{m})$ silicon wafer over 23 In *Proc. 26th Eur. Photovoltaic Solar Energy Conf. Exhib., Hamburg, Germany, pp. 871-874*, 2011.

[115] J. Koh, A. S. Ferlauto, P. I. Rovira, C. R. Wronski, and R. W. Collins. Evolutionary phase diagrams for plasma enhanced chemical vapor deposition of silicon thin films from hydrogen-diluted silane. *Appl. Phys. Lett.*, 75:2286–2288, 1999.

[116] M.W.M. van Cleef, J. K. Rath, F. A. Rubinelli, C. H. M. van derWerf, R. E. I. Schropp, and W. F. van derWeg. Performance of heterojunction p+ microcrystalline silicon n crystalline silicon solar cells. *J. Appl. Phys.*, 82:6089–6095, 1997.

118

[117] M. Balestrieri, J.-P. Pysch, D. andBecker, M. Hermle, W. Warta, and S. W. Glunz. Characterization and optimization of indium tin oxide films for heterojunction solar cells. *Solar Energy Mater. Solar Cells*, 95:2390–2399, 2011.

[118] D. Munoz, A. Favier, A. S. Ozanne, C. Denis, and P. J. Ribeyron. Analysis of o2 content in front ito layers for a-si:h/c-si heterojunction solar cells. In *Proc. 25th Eur. Photovoltaic Solar Energy Conf. Exhib.,Valencia, Spain, pp. 2255-2258.*, 2010.

[119] A. Descoeudres, Z. C. Holman, L. Barraud, S. Morel, S. D. Wolf, and C. Ballif. >21wafers compared. *IEEE J. Photovoltaics*, 3:83–89, 2013.

[120] W. Shockley. Theory and experiments on current transfer from alloyed contact to diffused layer. appendix b of research and investigation of inverse epitaxial uhf power transistors. *Shockley Res. Lab., Palo Alto, CA, USA, Tech. Rep.*, pages 64–207, 1964.

[121] S. Eidelloth and R. Brendel. Analytical theory for extracting specific contact resistances of thick samples from the transmission line method. *IEEE Electron Device Lett.*, 35:9–11, 2014.

[122] M. A. Green. "design of silicon solar cells," in solar cells: Operating principles, technology, and system applications. *Englewood Cliffs, NJ, USA: Prentice-Hall*, pages 145–161, 1992.

[123] S.-Y. Lee, H. Choi, H. Li, K. Ji, S. Namb, J. Choi, S.-W. Ahn, H.-M. Lee, and B. Park. Analysis of a-si:h/tco contact resistance for the si heterojunction back-contact solar cell. *Solar Energy Mater. Solar Cells*, 120:412–416, 2014.

[124] Z. C. Holman, A. Descoeudres, S. De Wolf, and C. Ballif. Record infrared internal quantum efficiency in silicon heterojunction solar cells with dielectric/metal rear reflectors. *IEEE J. Photovoltaics*, 3:1243–1249, 2013.

[125] A. Cuevas and R.A. Sinton. Prediction of the open-circuit voltage of solar cells from the steady-state photoconductance. *Prog. Photovoltaics, Res. Appl.*, 5:79–90, 1997.

[126] A. Khanna, Z. P. Ling, V. Shanmugan, M. Boreland, I. Hayashi, D. J. Kirk, H. Akimoto, A. G. Aberle, and T. Mueller. Screen printed metallization for silicon heterojunction solar cells. In *Proc. 28th Eur. Photovoltaic Solar Energy Conf. Exhib., Paris, France, pp. 1336-1339*, 2013.

[127] (2014, mar. 11). heraeus product spotlight. [online]. available: http://heraeus-pvsilverpaste.com/en/products/novelcellpastes/sol500series/sol9383_2.aspx.

References

[128] (2014, mar. 11). dupont solamet pv416 data sheet. [online]. available: `http://www2.dupont.com/Photovoltaics/en_US/products_services/metallization/solamet_lowtemp_silver.html`.

[129] N. Mingirulli, J. Hascke, R. Gogolin, R. Ferré, T.F. Schulze, J. Dessterhoeft, N.-P. Harder, and L. Korte. Interdigitated back-contacted silicon hetero-junction solar cells with improved fill factor and efficiency. *Proc. 37th IEEE Photovoltaic Specialists Conference, Seattle, USA*, 2011.

[130] N. Mingirulli, J. Hascke, R. Gogolin, T.F. Schulze, R. Rößler, J. Düsterhöft, R. Ferré, R. Meyer, J. Moschner, H. Plagwitz, N.-P. Wagner, T. Harder, L. Korte, R. Brendel, and B. Rech. Application of amorphous silicon buffer layers to interdigitated back contacted silicon heterojunction solar cells. *Proc. 26th European Photovoltaic Solar Energy Conference and exhibition, Hamburg, Germany*, pages 999–1003, 2011.

[131] J. Haschke, N. Mingirulli, R. Gogolin, R. Ferre, T. F. Schulze, J. Duesterhoeft, N.-P. Harder, and L. Korte. Interdigitated back-contacted silicon heterojunction solar cells with improved fill factor and efficiency,. *IEEE Journal of Photovoltaics*, 1(2):130–134, 2011.

[132] J. Schmidt, M. Kerr, and A. Cuevas. Surface passivation of silicon solar cells using plasma-enhanced chemical-vapour-deposited sin films and thin thermal sio_2/plasma sin stacks. *Semicond. Sci. Technol.*, 16:164–170, 2001.

[133] Y. Larionova, V. Mertens, N.-P. Harder, and R. Brendel. Surface passivation of n-type czochralski silicon substrates by thermal-sio_2/plasma-enhanced chemical vapor deposition sin stacks. *Appl. Phys. Lett.*, 96(3):032105/1–3, 2010.

[134] R. Stangl, M. Bivour, E. Conrad, I. Didschuns, L. Korte, K. Lips, and M. Schmidt. A novel high efficiency buried grid rear contact amorphous/crystalline silicon heterojunction solar cell concept. *22nd European Photovoltaic Solar Energy Conference, Milan, Italy*, 22:870–874, 2007.

[135] M. Tucci, L. Serenelli, E. Salza, L. Pirozzi, G. de Cesare, D. Caputo, M. Ceccarelli, P. Martufi, S. De Iuliis, and L.J. Geerligs. Back enhanced heterostructure with interdigitated contact - behind - solar cell. *Conference on Optoelectronic and Microelectronic Materials and Devices, 2008. COMMAD 2008.*, pages 242–245, 2008.

[136] T. Desrues, F. Souche, A. Vandeneynde, D. Muñoz, A.-S. Ozanne, and Ribeyron P.J. Emitter optimization for interdigitated back contact (ibc) silicon heterojunction (si-hj) solar cells. *25th European Photovoltaic Solar Energy Conference and Exhibition, Valencia, Spain*, pages 2374–2377, 2010.

[137] R. Stangl, J. Haschke, M. Bivour, L. Korte, M. Schmidt, K. Lips, and B. Rech. Planar rear emitter back contact silicon heterojunction solar cells. *Solar Energy Materials and Solar Cells*, 93(10):1900–1903, 2009.

[138] T. Desrues, P-J. Ribeyron, A. Vandeneynde, A.-S. Ozanne, D. Muñoz, F. Souche, C. Denis, and D. Heslinga. Progress in contactig a-si:h/c-si heterojunction solar cells and its application to interdigitated back contact structure. *24th European Photovoltaic Solar Energy Conference, Hamburg, Germany*, pages 2202–2205, 2009.

[139] M. Lu, U. Das, S. Bowden, and R. Birkmire. Rear surface passivation of interdigitated back contacted silicon heterojunction solar cell and 2d simulation study. *33rd IEEE Photovoltaic Specialists Conference, San Diego, CA, USA*, page 1651, 2008.

[140] P. Engelhart, N.P. Harder, T. Neubert, H. Plagwitz, B. Fischer, Meyer R., and R. Brendel. Laser processing of 22% efficient back-contacted silicon solar cells. *Proc. 21st EUPVSEC (WIP, Munich)*, page 773, 2006.

[141] R. Peibst, A. Merkle, S. Kirstein, T. Neubert, F. Dross, N. P. Harder, and R. Brendel. High-efficiency rise-ibc solar cells: influence of rear side passivation on pn-junction meander recombination. *28th European Photovoltaic Solar Energy Conference and Exhibition*, pages 971–975, 2014.

[142] S. Eidelloth, F. Haase, and R. Brendel. Simulation tool for equivalent circuit modeling of photovoltaic devices. *IEEE Journal of Photovoltaics*, 2 (4):572–579, 2012.

[143] (2015, feb. 26) [online]. available: http://www.linear.com/designtools/software/.

[144] A. Tomasi, B. Paviet-Salomon, D. Lachenal, S. Martin de Nicolas, A. Descoeudres, J. Geissbuehler, S. De Wolf, and C. Ballif. Back-contacted silicon heterojunction solar cells with efficiency >21%. *IEEE Journal of Photovoltaics*, 4(4):1046–1054, 2014.

List of publications

Parts of this thesis have previously been published in several of the following publications:

Refereed journal papers

1. R. Gogolin, R. Ferré, M. Turcu, N.-P. Harder. Silicon heterojunction solar cells: Influence of H_2-dilution on cell performance. *Solar Energy Materials & Solar Cells*, 106, p.47-50, 2012

2. R. Gogolin, M. Turcu, R. Ferré, J. Clemens, N.-P. Harder, R. Brendel, J. Schmidt. Analysis of series resistance losses in a-Si:H/c-Si heterojunction solar cells. *IEEE Journal of Photovoltaics*, Vol. 4 (5), p.1169-1176, 2014

3. N. Mingirulli, J. Hascke, R. Gogolin, R. Ferré, T.F. Schulze, J. Düsterhöft, N.-P. Harder, L. Korte, R. Brendel, B. Rech, Efficient interdigitated back-contacted silicon heterojunction solar cells, *Physica Status Solidi RRL*, 5, p.159-161, 2011

4. J. Haschke, N. Mingirulli, R. Gogolin, R. Ferré, T. F. Schulze, J. Düsterhöft, N.-P. Harder, L. Korte. Interdigitated Back-Contacted Silicon Heterojunction Solar Cells With Improved Fill Factor and Efficiency. *IEEE Journal of Photovoltaics*, 1(2), p.130 -134, 2011

Refereed conference papers

1. R. Gogolin, M. Turcu, R. Ferré, R. Brendel, N.-P. Harder, J. Schmidt. 730 mV bifacial screen-printed a-Si:H/c-Si heterojunction solar cells: open-circuit voltage and fill factor effects from a-Si:H layer thickness and front metallization,

28th European Photovoltaic Solar Energy Conference and Exhibition, 2BV.1.4, Paris, France, 2013

2. N. Mingirulli, J. Hascke, R. Gogolin, R. Ferré, T.F. Schulze, J. Düsterhöft, N.-P. Harder, L. Korte. Interdigitated back-contacted silicon heterojunction solar cells with improved fill factor and efficiency. *Proc. 37th IEEE Photovoltaic Specialists Conference*, Seattle, USA, 2011

3. N. Mingirulli, J. Hascke, R. Gogolin, T.F. Schulze, R. Rößler, J. Düsterhöft, R. Ferré, R. Meyer, J. Moschner, H. Plagwitz, T. Wagner, N.-P. Harder, L. Korte, R. Brendel, B. Rech. Application of amorphous silicon buffer layers to interdigitated back contacted silicon heterojunction solar cells. *Proc. 26th European Photovoltaic Solar Energy Conference and exhibition*, Hamburg, Germany, p.999-1003, 2011

4. R. Brendel, T. Dullweber, R.Gogolin, H. Hannebauer, N.-P. Harder, J. Hensen, S. Kajari-Schröder, R. Peibst, J. H. Petermann, U. Römer, J. Schmidt, H. Schulte Huxel, V. Steckenreiter. Recent progress and options for future crystalline silicon solar cells. *28th European Photovoltaic Solar Energy Conference and Exhibition*, 2BP.1.1, Paris, France, 2013

5. J. H. Petermann, H. Schulte-Huxel, V. Steckenreiter, R. Gogolin, S. Eidelloth, T. Dullweber, S. Kajari-Schröder, R.Brendel. Module interconnection of both sides-contacted silicon solar cells by screen-printing. *35th IEEE Photovoltaic Specialists Conference*, Tampa, Florida, 2013

Other publications

1. R. Gogolin, N.-P. Harder. Trapping behavior of Shockley-Read-Hall recombination centers in silicon solar cells. *Journal of Applied Physics*, 114, 064504, 2013

2. N.-P. Harder, R. Gogolin, R. Brendel. Trapping-related recombination of charge carriers in silicon. *Applied Physics Letters* 97, 112111/1-3, 2010

3. R. Ferré, R. Gogolin, J. Müller, N.-P. Harder, R. Brendel. Laser transfer doping for contacting *n*-type silicon solar cells. *Physica Status Solidi A*, 208, p.1964, 2011

4. R. Gogolin, N.-P. Harder, R. Brendel. Trapping-related recombination of charge carriers in silicon. *Proc. 35th IEEE Photovoltaic Specialists Conference*, Honululu, USA, p.443-446, 2010

5. R. Ferré, R. Gogolin, J. Müller, N.-P. Harder, M. Kessler, C. Mader, P. Giesel, T. Neubert, R. Brendel. Laser transfer doping using amorphous silicon. *Proc.*

26th European Photovoltaic Solar Energy Conference and exhibition, 879-883, Hamburg, Germany, 2011

Given talks

1. R. Gogolin, N.-P. Harder, Trapping in Silicium, March 2, 2010, Silicon Forest, Falkau, Germany

2. R. Gogolin, M. Turcu, S. Mau, N.-P. Harder, Entwicklung von Heterojunction Solarzellen, March 5, 2013, Silicon Forest, Falkau, Germany

3. R. Gogolin, R. Ferré, M. Turcu, N.-P. Harder, Silicon heterojunction solar cells: Influence of H_2-dilution on cell performance, April 3-5, 2012, 2nd SiliconPV Conference, Leuven, Belgium

4. R. Gogolin, R. Ferré, M. Turcu, N.-P. Harder, Loss analysis of a-Si:H/c-Si heterojunction solar cells, April 23, 2013, npv workshop, Chambéry, France

Danksagung

Abschließend möchte ich mich ganz herzlichen bei allen bedanken, die zum Gelingen dieser Arbeit beigetragen haben:

- **Prof. Dr. rer. nat. Jan Schmidt** für die Übernahme des Referats und die hervorragende wissenschaftliche Betreuung.

- **Prof. Dr. rer. nat. Christoph Tegenkamp** für die freundliche Übernahme des Koreferats.

- **Prof. Dr.-Ing. Rolf Brendel** für die Anstellung am ISFH und die wissenschaftliche Unterstützung.

- **Dr. Nils-Peter Harder** für die enge Zusammenarbeit während meiner Promotion, für die vielen inspirativen Gespräche und für die herausragende wissenschaftliche Betreuung.

- Dem gesamten TopShot Team **Dr. Rafel Ferré**, **Dr. Mirca Turcu**, **Susanne Mau** und **Sabrina Schimanke** vom ISFH sowie **Dr. Lars Korte**, **Dr. Nicola Mingirulli** und **Jan Haschke** vom HZB für die angenehme und erfolgreiche Zusammenarbeit.

- Den technischen Angestellten **Anja Christ**, **Sarah Spätlich** und **Ilka Feilhaber** für die stets freundliche und kompetente Beratung und Unterstützung bei der Probenprozessierung.

- **Nadja Braun** für die Unterstützung bei der Inkjet Prozessierung.

- **Nadine Wehmeier** und **Michael Siebert** für die Unterstützung am Clustertool.

- **Tobias Neubert**, **David Sylla** und **Peter Giesel** für die Hilfe bei der Laserprozessierung.

- **Miriam Berger** und **Birgit Beier** für die Unterstützung am Siebdrucker.

- **Arne Schmidt** und **Martin Wolf** für die Unterstützung im Charakterisierungslabor.

- **Hendrik Holst** für die Hilfe mit SunRays und die geduldige Beantwortung von LaTeX-Fragen.

- **Marita Steinhof** für die vielen Bestellungen und ihren unerschütterlichen Einsatz für das Allgemeinwohl aller Mitarbeiter.

- Den hausinternen Technikern und Ingenieuren **Stefan Beiße**, **Michael Weiß**, **Johannes Schlieker** und **Andreas Treder** für die Instanthaltung aller Anlagen und die Unterstützung bei technischen Fragen zum Clustertool.

- **Wolfgang Gaßdorf**, **Mareike Weiner**, **Sabine Kreber**, **Carina Faulhaber**, **Sonja Helbig**, **Heidi Paldino** und **Mareike Radloff** für die Unterstützung in allen verwaltungstechnischen Angelegenheiten.

- Meinen Kollegen und Freunden **Christian Ulzhöfer**, **Udo Römer** und **Christopher Kranz** für die super Bürogemeinschaft und die schönen Momente auf und nach der Arbeit.

- Allen **Kollegen** am ISFH für das sehr angenehme und freundliche Arbeitsklima, die stetige Diskussionsbereitschaft bei Fachfragen sowie die zahllosen Tipps und Anregungen.

- Mein besonderer Dank gilt **meiner Familie** für ihre liebevolle Unterstützung während der gesamten Promotion.

128

Persönliche Daten

Name	Ralf Gogolin
Anschrift	Richard-Brandt-Straße 2, 30900 Wedemark
Geburtsdatum	28. Februar 1981
Geburtsort	Burgwedel
Nationalität	deutsch

Bildung

Juni 2000	Abitur am Gymnasium Mellendorf
September 2000 - Juni 2001	Grundwehrdienst im Kraftfahrausbildungszentrum Munster
Oktober 2001 - Juni 2009	Studium der technischen Physik an der Leibniz Universität Hannover Diplomarbeit am Institut für Solarenergieforschung Hameln (ISFH) zum Thema: Ladungsträgertrapping und Ladungsträgerrekombination in Silicium Diplom im Juni 2009
Juli 2009 - März 2015	Doktorand am Institut für Solarenergieforschung Hameln (ISFH)

Berufliche Tätigkeit

Juli 2009 - März 2013	Wissenschaftlicher Mitarbeiter am Institut für Solarenergieforschung Hameln (ISFH) in der Arbeitsgruppe Hocheffizienz Solarzellen
Februar 2010 - März 2010	Gastwissenschaftler am Helmholtz Zentrum Berlin (HZB) am Institut Silizium-Photovoltaik
April 2013 - Mai 2015	Wissenschaftlicher Mitarbeiter am Institut für Solarenergieforschung Hameln (ISFH) in der Arbeitsgruppe PV Materialien